UNIVERSITY OF CALIFORNIA
RIVERSIDE

Parameter Estimation Procedure of Reaction Diffusion Equation with Application on Cell Polarity Growth

A Dissertation submitted in partial satisfaction
of the requirements for the degree of

Doctor of Philosophy

in

Applied Statistics

by

Chenwei Tian

September 2018

Dissertation Committee:

Dr. Xinping Cui, Chairperson
Dr. Weixin Yao
Dr. Zhenbiao Yang

The Dissertation of Chenwei Tian is approved:

Committee Chairperson

University of California, Riverside

Acknowledgments

I am most grateful to my advisor, Dr. Xinping Cui, and co-advisor, for her support and encouragement. Without her guidance, this dissertation would not exist.

I would also like to thank Dr. Zhenbiao Yang and his post-doc Dr. Jingzhe Guo, for their biological motivation and experimental data. I appreciate Dr. Junping Shi and his Ph.D student Dr, Qingyan Shi, for their mathematical work presented in this thesis. The last but not the least, I would also like to thank Dr. Nicolas Brunel, for his constructive comments and ideas on statistical part of this dissertation. Without his suggestions, this dissertation would not be completed.

To my parents for all the support.

ABSTRACT OF THE DISSERTATION

Parameter Estimation Procedure of Reaction Diffusion Equation with Application on Cell Polarity Growth

by

Chenwei Tian

Doctor of Philosophy, Graduate Program in Applied Statistics
University of California, Riverside, September 2018
Dr. Xinping Cui, Chairperson

Cell polarity is a fundamental feature of almost all cells. An excellent example for studying cell polarity is pollen tube tip growth, which is a specialized form of cell growth, in which growth is limited to the apical end of the cell, allowing the cell to rapidly elongate and penetrate tissues. The key of pollen tube tip growth is polarized distribution on plasma membrane of a particle named ROP1 and Ca^{2+}. The oscillated distribution is the result of a feedback loop between ROP1 and Ca^{2+}.

This dissertation takes a multidisciplinary approach by combining knowledge of cell biology, mathematics, and statistics in order to quantitatively study the full system for the interaction between ROP1 and Ca^{2+} in pollen tube tip growth. In the first part of the dissertation, we propose a mechanistic reaction-diffusion equation derived model of cell polarity, and analytically study the spatiotemporal dynamic of proposed model. In the second part, we first introduce parameter estimation procedure of linear reaction-diffusion equation, then extend it to nonlinear case. Our approach can be seen as an extension of gradient matching procedure. Moreover, consistency and asymptotic normality of proposed

method will be discussed in linear case. And simulation study will be conducted in both cases. In the end, we will apply proposed method on the pollen tube tip growth model to predict ROP1 and Ca^{2+} concentration on plasma membrane. And guidance of refining proposed model is given based on predication of ROP1 and Ca^{2+}.

Contents

List of Figures

List of Tables

Chapter 1

Introduction

Cell polarity refers to the asymmetric shape and structure of cells, which plays a very important role in specialized functions in both animal cells and plant cells. In the immune system of animals, a type of white blood cell called monocyte can move quickly toward the site of infection through cell polarity, differentiate into macrophages and remove dead cell debris. Cell polarity also plays an important role in asymmetric division of epithelial stem cells, which is pivotal for the maintenance of epithelial tissue homeostasis. Loss of cell polarity may cause symmetric division, leading to tissue overgrowth, thereby favoring tumor initiation. In plant cells, cell polarity is involved in processes such as embryogenesis, organogenesis, and vascular tissue formation and regeneration. For example, tip growth of pollen tubes and root hairs is controlled by cell polarity. In this dissertation, we will focus on the cell polarity of pollen tubes.

Cell polarity in pollen tube tip growth is described in [43]. It begins with the recruitment and activation of the signaling apparatus, i.e., ROP GTPbase, under the spatial

cues that determine the site and the direction of tip growth. Once the localization of ROP1 has been established and maintained, active ROP1 controls exocytosis of pectin that determines cell wall mechanics and therefore the shape of pollen tubes. Many previously proposed models focus on the cell wall mechanics and shape formation of pollen tubes. In this dissertation, we will focus on modeling the establishment of polarized distribution of ROP1 on the membrane.

Altschuler et.al.[1] proposed a PDE model for yeast cell polarization but only considered positive feedback. The reaction-diffusion pattern formation theory suggests that positive feedback alone cannot generate stable spatial patterns. Chou, Nie, etc. have also constructed RD models for yeast cell polarization induced by pheromone spatial gradient [5, 19, 22, 45, 46]. As a key regulator of the self-organizing PT system, the activity and distribution of ROP1 are fine-tuned by both positive and negative feedback mechanisms as well as slow diffusion. Yang's group have shown that Ca^{2+} is involved in the negative feedback regulation of ROP1 signaling, and conducted experiments [12, 15, 16, 26, 40] to study the oscillation of Ca^{2+} gradient and established ODE based model to describe Ca^{2+} activity. In general, ROP1 activity can be summarized as: (1) activation of inactive ROP1; (2) inhibition of active ROP1, which depends on Ca^{2+}; (3) lateral diffusion of molecules along the membrane. On the other hand, Ca^{2+} concentration near plasma membrane is determined by: (1) influx of Ca^{2+}, which is regulated by ROP1; (2) self-decay of Ca^{2+}; and (3) diffusion of Ca^{2+} along the membrane.

In the first part of this dissertation, we focus on mathematical modeling of pollen tube tip growth. In chapter 2, we will first review some models of ROP1 activity and Ca^{2+}

activity and their drawbacks. We then propose a partial differential equation (PDE) based model, which describes interaction between ROP1 and Ca^{2+} with diffusion effect taken into account. In chapter 3, we will analytically study the spatial-temporal dynamic of proposed model. First, we will discuss temporal pattern of the kinetic system of proposed model. In this section, conditions on parameter, under which oscillation can be generated, will be discussed. Then, we will add the diffusion and non-local effect to study the spatial pattern of the proposed model.

In the second part of this dissertation, we focus on statistical inference based on the proposed PDE mdoel for pollen tube tip growth. In particular, we will introduce a general framework of parameter estimation procedure for reaction diffusion equation, which can be applied to our proposed model. In fact, parameter estimation of differential equation (DE) based model have been widely studied [4, 18, 27, 39]. In chapter 4, we will review different type of parameter estimation procedures for DE models as well as their limitations, such as lack of explicit formula of variation of parameter estimator, and requirement of nonparametric estimation of higher order derivatives. In chapter 5 and 6, we will introduce our parameter estimation procedure for reaction diffusion equation, which can avoid nonparametric estimation of higher order derivatives. The key idea of our method is to decompose unknown spatial-temporal dynamic by eigenfunction of Laplacian operator. With this decomposition, we can transform our PDE to a set of ODEs, which describe how weight of eigenfunctions change over time. In chapter 5, we will first discuss about parameter estimation procedure, then provide consistency and asymptotic normality of proposed procedure for linear PDE together with simulation study. In chapter 6, proposed

method will be extended to nonlinear PDE. We will first describe parameter estimation procedure and its implementation, then conduct simulation study to illustrate consistency of proposed estimators. In chapter 7, we will apply the proposed methods to estimate positive feedback and negative feedback parameters in pollen tube tip growth model and predict ROP1-Ca^{2+} concentration on plasma membrane. In addition, we suggest to refine our pollen tube tip growth model guided by results of our real data analysis.

Part I

Mathematical Modeling of Pollen Tube Tip Growth

Chapter 2

Biological Background: Rapid Spatial-temporal Oscillation of Pollen Tube Tip Growth

As a key regulator of the self-organizing pollen tube system, the activity and distribution of ROP1 are fine-tuned by both positive and negative feedback mechanisms as well as slow diffusion. It has been indicated that the Ca^{2+} gradient is involved in the negative feedback regulation of ROP1. In addition, it also has been shown that ROP1 promotes the formation of the intracellular Ca^{2+} gradients probably via the influx of extracellular Ca^{2+}[12, 16]. In this chapter, we propose a reaction-diffusion model of ROP1 and Ca^{2+} distributions on the cell membrane to show how ROP1 and Ca^{2+} are spatio-temporally intertwined and what is the quantitative relationship between them in order to generate the ROP1-Ca^{2+} spatio-temporal oscillation.

Modeling polarized distribution of signaling molecule on plasma membrane , such as Cdc42 in budding yeast, has been widely studied. Altschuler et al. [1] showed that feedbacks alone can generate polarized distribution of signaling molecule when the number of molecules is small. A PDE model for yeast cell polarization was proposed in [1] but it only considered the positive feedback. The reaction-diffusion pattern formation theory suggests that positive feedback alone cannot generate stable spatial patterns. Reaction-diffusion models for yeast cell polarization induced by pheromone spatial gradient have been established in [5, 19, 22, 45, 46]. Moreover, Gupta [13] provides an explanation for the existence of polarized distribution in such cells if the population size is large. In recent work, Zhen[38] proposed a PDE model for the ROP1 dynamics for the pollen tube tip growth, which captures positive feedback, negative feedback and diffusion of ROP1. It is shown in [38] that the positive steady state of proposed model is unique and has a soliton-like profile which resembles the *Arabidopsis* PT experimental ROP1 data obtained in Yang lab.

Several studies from the Yang group have shown that Ca^{2+} is involved in the negative feedback regulation of ROP1 signaling, and they have formulated an ODE based mathematical model and conducted experiments [12, 15, 16, 26, 40] to investigate the oscillation. On the other hand, ROP1 activation promotes increase in calcium level.

In this chapter, we will first provide some main results about ROP1 activity. Then we will discuss the interaction between ROP1 and Ca^{2+}. In the end, we will introduce our proposed full system of reaction-diffusion model for interaction between ROP1 and Ca^{2+} on the cell membrane.

2.1 Main results of ROP1 activity

The redistribution of signaling molecules is determined by the rates of four fundamental transport mechanisms [1] (Fig 2.1): (1) recruitment (k_{fb}) of cytoplasmic molecules to the locations of membrane-bound signaling molecules; (2) spontaneous association (k_{on}) of cytoplasmic molecules to random locations on the plasma membrane; (3) lateral diffusion (D) of molecules along the membrane; and (4) random disassociation (k_{off}) of signaling molecules from the membrane.

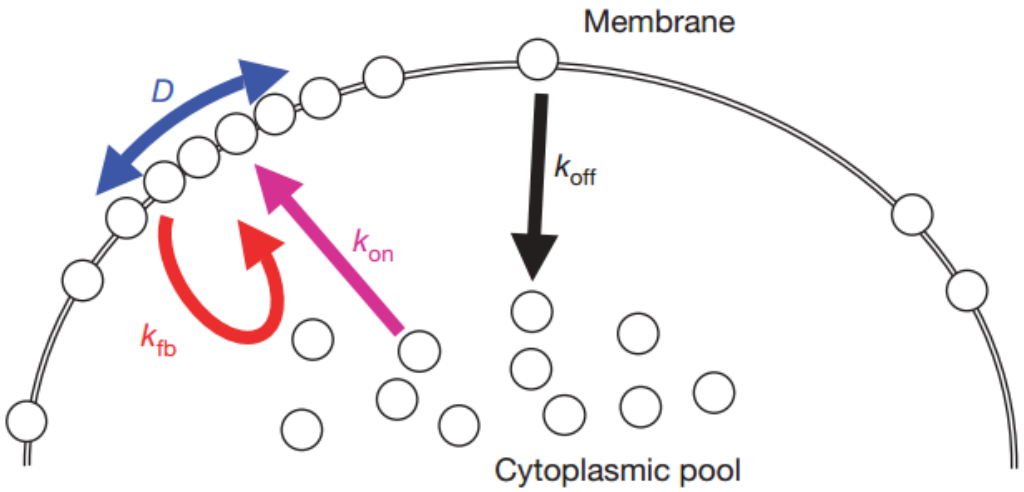

Figure 2.1: A conceptual model of a ROP1 positive feedback circuit is characterized by four biologically interpretable parameters [1].

In an initial analysis of the dynamics of this positive feedback circuit when the spatial distribution of molecules on the membrane is ignored, Altschuler [1] found out that the fraction of total signaling molecules on the membrane can switch from zero to a final equilibrium h_{eq} with a half time of $\sim 1/(h_{eq}k_{fb})$. This equilibrium fraction h_{eq} can be estimated simply as $1 - k_{off}/k_{fb}$. Accounting for the spatial distribution of signaling molecules

on the plasma membrane, Altschuler [1] shows that distinct polarized regions emerge spontaneously When the total number of signaling molecules (N) is small. He also showed that this behaviour is strongly affected by the ratio k_{on}/k_{fb} of spontaneous membrane association rate to feedback rate. When the ratio is large, it is more likely to result in a spatially homogeneous density. When the ratio is small, local amplification by positive feedback frequently results in the emergence of spatially isolated clusters of signaling molecules. When the total number of signaling molecules (N) is large, Gupta [13] illustrated that at stationarity, the membrane molecules are arranged into clans of various sizes and molecules in a clan are spatially clustered. In addition, there are times when most of the molecules are part of a single clan and lie in a single hemisphere on the membrane, thereby causing a cell to polarize.

The rest of the chapter is organized as follows. Section 2.1.1 presents a deterministic model which gives the results on equilibrium fraction h_{eq}. In section 2.1.2, we present a stochastic process consisting of a continuous time Markov process and an undergone Brownian motion, and provide the results about cell polarity behavior when N is small. In section 2.1.3, A Fleming-Viot stochastic process will be discussed, which characterizes membrane molecule behavior when N is large. In section 2.1.4, we discuss the PDE model proposed by Zhen [38] and describes dynamic of ROP1 distribution on the cell membrane.

2.1.1 Deterministic Model

In this section, we summarize Altschuler's deterministic model, including two parts: (1) ODE model of the amount of all molecules on the membrane; (2) PDE model of dynamics of density of membrane-mound molecules [1].

First, Altschuler[1] modeled the fraction $h(t)$ of all molecules on the membrane that changes in time t by the following ordinary differential equation:

$$\frac{dh}{dt} = k_{on}(1-h) + k_{fb}(1-h)h - k_{off}h \tag{2.1}$$

Let h_+ and h_- be two equilibrium of model (2.1) with $\frac{dh}{dt} = 0$ so we have

$$h_\pm = \frac{k_{fb} - k_{on} - k_{off}}{2k_{fb}} \pm \sqrt{(\frac{k_{fb} - k_{on} - k_{off}}{2k_{fb}})^2 + \frac{k_{on}}{k_{fb}}} \tag{2.2}$$

Hence, solution of model (2.1) can be written as

$$h(t) = \frac{h_+ + h_- C e^{-t/T_{eq}}}{1 + C e^{-t/T_{eq}}} \tag{2.3}$$

where $C = \frac{h_+ - h(0)}{h(0) - h_-}$, $T_{eq} = [(h_+ - h_-)k_{fb}]^{-1}$ and $h(0)$ is the initial value of $h(t)$. Therefore, two conclusions can be drawn from this solution:

1. Assuming $t/T_{eq} \gg 0$, we have $h(t) = h_+ - (h_+ - h_-)Ce^{-t/T_{eq}}$. In this case, $h(t)$ approaches h_+ at an exponential rate with half-time T_{eq}, i.e. $h_+ - h(t)$ decreases by a factor 2 in every time interval length $T_{eq}\ln 2$.

2. Assuming $k_{fb} > k_{off} > 0$ and $k_{on} \ll k_{fb} - k_{off}$, we have $h_{eq} = h_+ \approx 1 - \frac{k_{off}}{k_{fb}}$ and $h_- \approx 0$. In this case, $T_{eq} \approx (h_{eq}k_{fb})^{-1}$.

In the next stage, Altschuler[1] modeled the density of membrane-bound molecules $u(x,t)$ that evolves in time by the following partial differential equation:

$$\frac{\partial u}{\partial t} = \frac{1}{2}D \bigtriangledown^2 u + k_{on}(1-h) + k_{fb}(1-h)u - k_{off}u \tag{2.4}$$

where h as $h(t)$ in model (2.1). For PDE (2.4), We can reparameterize it with $v(x,t) = \frac{u(x,t) - h(t)}{h(t)}$. The quantity $v(x,t)$ can be interpreted as the deviation of membrane density

from its spatial average relative to this average. Then PDE (2.4) can be rewritten as:

$$\frac{\partial v}{\partial t} = \frac{1}{2} D \bigtriangledown^2 v - k_{on} \frac{1-h}{h} v \tag{2.5}$$

Altschuler [1] pointed out that spatial oscillations of the membrane density decay exponentially with half time of $T_{\text{diff}} = 2\ln 2 \times \lambda_1^2/D$, where λ_1 is the first eigenvalue of the Laplacian operator. In a special case where the membrane is modeled by a circle of radius R, $T_{\text{diff}} = 2\ln 2 \times R^2/D$. In the case where the membrane is modeled by a sphere of radius R, $T_{\text{diff}} = \ln 2 \times R^2/D$. Therefore, solutions of the PDE model may exhibit spatial localization for some time, this localization cannot persist. That is to say, it is impossible to achieve a spatially inhomogeneous steady-state for positive feedback system. Moreover, since T_{diff} only depends on the diffusion constant and the physical size of the membrane, but not on the rate constants k_{on}, k_{fb} and k_{off}, a change in rates k_{on}, k_{fb} and k_{off} will not lead to spatially localized state.

2.1.2 Stochastic Model: Markov Process for small population

Besides describing the positive feedback system by PDE model (2.4), Altschuler [1] also introduced a three-stage stochastic model to describe the stochastic process of positive feedback system. The first stage describes the behavior of the total number of particles on the membrane $n(t)$ with a Markov process. The second stage describes the behavior of the locations of the particles on the membrane with a Brownian motion. The third stage describes the behavior of the clans on the membrane with a birth-death process. The models are as follow:

Stage 1 : The total number of particles on the membrane $n(t)$ can be described with a Markov process with the time evolution of the probability distribution of $n(t)$ written as:

$$\frac{dp_n(t)}{dt} = W_n - W_{n-1} \tag{2.6}$$

where $p_n(t)$ is the probability that there are n particles on the membrane at time t; $W_n = k_{off}(n+1)p_{n+1}(t) - (k_{on} + k_{fb}\frac{n}{N})(N-n)p_n(t)$ [9]. Denote a sequence of random times $t_1 < t_2 < \cdots$, at which $n(t)$ jumps by ± 1. During each time interval (t_i, t_{i+1}), the number of particles on membrane is a constant n_i. Denote $x_1(t), \cdots, x_{n_i}(t)$ be the location of each particles at time t during $t \in [t_i, t_{i+1}]$.

Stage 2 : During time period $t \in [t_i, t_{i+1}]$, the location of each particles $x_1(t), \cdots, x_{n_i}(t)$ can be described as a Brownian motion with diffusion coefficient D. Moreover, let the locations at the end of the previous time interval $[t_{i-1}, t_i]$ be $x_1(t_i), \cdots, x_{n_{i-1}}(t_i)$. Then, the locations at the beginning of current time interval $[t_{i-1}, t_i]$ can be initialized based on the old locations in following ways:

1. If $n_i = n_{i-1} + 1$, then the new locations are set by keeping the old locations and randomly adding a new location $x_{n_{i-1}+1}(t_i)$. Notice that the way of randomly picking the new location depends on whether it is a spontaneous-on event or a recruitment event. With probability $k_{on}/[k_{on} + k_{fb}(N - n_{i-1})]$, a spontaneous-on event occurred, in which case we let $x_{n_i}(t_i)$ be a randomly selected point on the membrane. Otherwise a recruitment occurred, in which case we let $x_{n_i}(t_i)$ be a random selection from the already exist particle location.

2. If $n_i = n_{i-1} - 1$, then the new locations are set as the old locations with randomly

discarding one of old locations.

Stage 3 Particles can be tracked individually, and their lineage can be considered by dividing the particles on the membrane into clans. Initially each particle is assigned to its own clan. Then any particle which gets recruited to the membrane are assigned to the clan of the recruiting particle.

Altschuler [1] modeled dynamics of clans in a time interval $[0, T_0]$, where no spontaneous on-event happens. Assuming that initially $N_0 = h_{eq}N$ particles on the membrane starting its own clan so there are N_0 clans at the beginning numbers with $\mathbb{C} = 1, \cdots, N_0$, where N is total number of particles in the cell and h_{eq} is equilibrium fraction of particles on the membrane. Let $n_{\mathbb{C}}(t)$ be the size of clan $\mathbb{C}$ at time t so $n_{\mathbb{C}}(0) = 1$ for any $\mathbb{C} = 1, \cdots, N_0$. Altschuler [1] described the behavior of $n_{\mathbb{C}}(t)$ as a birth-death process with birth rate as $(1-h)k_{fb}$ and death rate as k_{off}, which are the same at the equilibrium. Then denote $p_n^{\mathbb{C}}(t)$ as the changes of the probability that a given clan $\mathbb{C}$ has n particles at time t, which can be modeled as

$$\frac{dp_n^{\mathbb{C}}(t)}{dt} = \begin{cases} k_{off}\{(n-1)p_{n-1}^{\mathbb{C}}(t) - 2np_n^{\mathbb{C}}(t) + (n+1)p_{n+1}^{\mathbb{C}}(t)\} & \text{if } n > 0 \\ k_{off}p_1^{\mathbb{C}}(t) & \text{if } n = 0 \end{cases} \tag{2.7}$$

with initial value as $p_1^{\mathbb{C}}(0) = 1$ and $p_i^{\mathbb{C}}(0) = 0$ for any $i \neq 0$. In this case, $p_0^{\mathbb{C}}(t)$ is the probability of a given clan $\mathbb{C}$ becomes extinct at time T. By solving model (2.7), the probability that a given clan still exist at time t can be given as $1 - p_0^{\mathbb{C}}(t) = \dfrac{1}{1+k_{off}t}$. Hence, the expected number of clans at time t is $\dfrac{N_0}{1+k_{off}t}$. Therefore, the expected time that only one clan is left on the membrane can be calulated as $T_{stoch} \approx N\left(\dfrac{1}{k_{off}} - \dfrac{1}{k_{fb}}\right)$ if $N_0 \gg 1$.

Therefore, in order to have only one clan on the membrane, $T_{stoch} < T_0$ is required where T_0 is the time between two spontaneous on-event. In fact, with $h_{eq}N$ particles on the membrane, the spontaneous on-event occur rate is $k_{on}(1 - h_{eq})N$, which leads to average time between two spontaneous on-event $T_{on} = [k_{on}(1 - h_{eq})N]^{-1}$. Therefore, the sufficient condition to guarantee cluster formation is

$$T_{stoch} \ll T_{on} \qquad \Rightarrow \qquad \frac{k_{on}}{k_{off}} \ll (h_{eq}(1 - h_{eq})N^2)^{-1} \tag{2.8}$$

Moreover, the above analysis did not depend on the initial distribution of particles on the membrane. Thus, the polarized state will frequently recur infinitely and with high probability in any timespan of length T_{stoch}. In addition, from stage 2 model, which describes the location of each particles as Brownian motion with diffusion coefficient D. One can expect the particles of a clan to be located in a region of radius $d_{stoch} = \sqrt{DT_{stoch}}$, which means that if diffusion rate D is small then the clan members will spread out to form a localized particle cluster; if diffusion rate D is very large then the clan members will move so far to evenly spread cover membrane and form no cluster.

Besides the case where the number of signaling molecules is closed to equilibrium, Altschuler [1] also discussed the case where the number of signaling molecules N is sufficiently small. In this case, the spontaneous event is so infrequent that there is no signaling molecules on the membrane, in most cells. Based on model (2.6) in stage 1, the probability that there is no particles on membrane can be written as

$$p_0 = P(n(t) = 0) \approx \{1 + \frac{\alpha}{A}\sqrt{N}e^{BN}\}^{-1} \tag{2.9}$$

where $\alpha = \dfrac{k_{on}}{k_{fb}}$; $A = h_{eq}\sqrt{(1 - h_{eq})/2\pi}$, $B = -h_{eq} - \ln(1 - h_{eq})$. Hence, the probability of an empty membrane will be exactly 50% when $k_{on}/k_{fb} \approx AN^{-1/2}e^{-BN}$.

2.1.3 Stochastic Model: Fleming-Viot process for infinite population limit

Gupta [13] proposed a Fleming-Viot process for positive feedback circuit when N is large. He claimed that if we let the feedback strength of each membrane bound molecule increase linearly with the population, then we can get recurring cell polarity in the infinite population limit. Gupta scales up k_{fb} and k_{off} by the population size N and leaves k_{on} the same. Here we consider the recruitment, spontaneous association and random disassociation of molecules as birth, immigration and death process, respectively.

Gupta [13] started with the Markov process and Brownian motion described by Altschuler [1] as in section 2.1.2. He showed that in the infinite population limit, the dynamics of cell molecules is given by a measure-valued process μ where $\mu = h_{eq}v$ with v being a Fleming-Viot process. He also proved ergodicity and unique stationarity of this process v in the sense that its transition function converges exponentially to the stationary distribution.

At any time, the molecules on the membrane can be divided into clans based on their ancestral relationship. According to the theorem proposed by Ethier and Kurtz [7] and results in Feng's book [10], at stationarity in Fleming-Viot process, the sizes of atoms in descending order has the Possion-Dirichlet distribution with the parameter $\theta = \dfrac{k_{on}}{k_{off}}$. It indicates that there are a few large clans and many small clans.

Gupta [13] mainly discussed the size and the proportion of clans. He showed that while the molecules are constantly diffusing on the membrane, each clan will not spread out more and more with time. In fact, the expected distance squared between two molecules from the same clan at stationarity is $S_p(t) = \dfrac{2D}{(k_{on} + k_{fb})\alpha + D/R^2}$ where

$\alpha = (1 - h_{eq})/h_{eq}$. Therefore, as the diffusion speed D goes down or the effective feedback strength $\gamma = k_{fb}(\frac{1 - h_{eq}}{h_{eq}})$ increases, the quantity S_p gets smaller. As for the proportion of clans, Gupta [13] defined a concept called ϵ-polarized. For any $0 < \epsilon \ll 1$, a cell is ϵ-polarized if at least $(1 - \epsilon)$ fraction of the membrane population belongs to a single clan and also resides in a single hemisphere on the membrane. Then he showed that the cell gets ϵ-polarized (defined below) infinitely frequent. Therefore, we obtain recurring cell polarity when N is large.

2.1.4 Reaction-Diffusion model

The PDE model (2.4) proposed by Altschuler [1] was further modified in [38], in which the spontaneous term was eliminated for two reasons. Firstly, the spontaneous rate k_{on} is much smaller than k_{fb} and k_{off}. If k_{on} is not small, then most particles will arrive on the membrane through spontaneous associations rather than recruitment. The stochastic model above indicates that no cluster will be formed in this case. Therefore, we can assume that k_{on} is small enough. Secondly, the time between two spontaneous events follows an exponential distribution with expectation $T_{on} = (k_{on}(1 - h_{eq})N)^{-1}$. When k_{on} is small, T_{on} will be large leading to a long time between two spontaneous events. Since the PDE model only describes the change of distribution of ROP1 intensity in a small time limit, i.e. $\frac{dR(x,t)}{dt}$, we can assume that spontaneous event does not happen.

The ROP1 polarization dynamics without spontaneous association can be simplified as three main procedure (Fig 2.2): (1) activation of inactive ROP1; (2) deactivation of active ROP1; (3) lateral diffusion of ROP1 along the membrane. The activation and deacti-

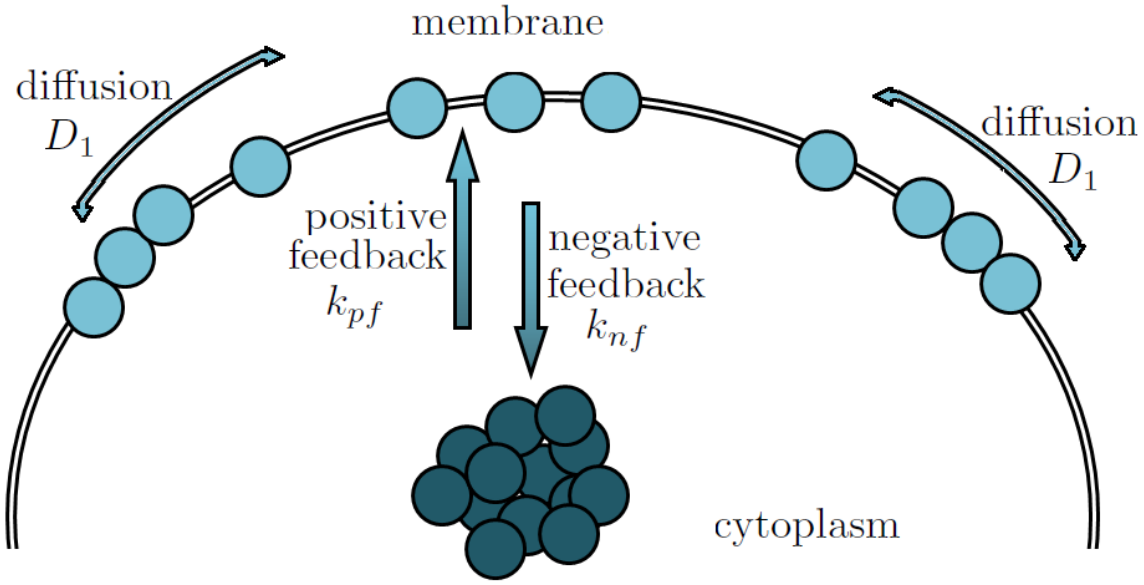

Figure 2.2: ROP1 polarization dynamics

vation of ROP1 can be considered as positive feedback and negative feedback, respectively. Both activation rate and deactivation rate are proportional to substrate concentration. Since majority of inactive ROP1 are in cytoplasm with high mobility, the activation rate is proportional to the total amount of cytoplasmic molecules (i.e. $R_{tot} - \int R dx$) with rate k_{pf}. Moreover, empirical data analysis suggests that the activation rate is proportional to R^{α} where $\alpha > 1$. On the other hand, most active ROP1 are on membrane. Since molecules on the membrane have much less mobility, the deactivation rate is proportional to the density of molecules (i.e. $R(x,t)$) at given location with rate k_{nf}. Therefore, the PDE model (2.4) were modified as following in [38]:

$$\frac{\partial R(x,t)}{\partial t} = k_{pf} R(x,t)^{\alpha} \left(\frac{R_{tot} - \int_{-L_0}^{L_0} R(x,t)dx}{R_{tot}}\right) - k_{nf} R(x,t) + D\frac{\partial^2 R(x,t)}{\partial x^2} (x,t) \in [-L_0, L_0] \times [0, \infty] \tag{2.10}$$

where $R(x,t)$ is the ROP1 density on cell membrane, k_{pf} and k_{nf} are coefficients of positive feedback and negative feedback, respectively. R_{tot} denotes the total free ROP1 in the cell, and D is the diffusion coefficient of ROP1 on membrane. The activation of inactive ROP1 is assumed to be proportional to R^α for $\alpha \in (1,2)$ based on Yang lab's experimental results, and x is the signed distance from the tip of pollen tube.

It has been shown in [38] that the positive steady state of (2.10) is unique and has a soliton-like profile which resembles the *Arabidopsis* PT experimental ROP1 data obtained in Yang lab. Moreover the parameters k_{pf} and k_{nf} were estimated based on the numerically integrated steady state profile of (2.10) and the experimental data using a constrained Least Squares (CNLS) method. The experimental data fits with the numerical steady state of (2.10) reasonably well. However the positive steady state of (2.10) indeed is unstable with respect to the time-evolution dynamics of (2.10), which suggests that some other feedback mechanism or other key activator/inhibitor in the system is not identified in (2.10), such as Ca^{2+} inhibition. Also the model (2.10) cannot produce time-periodic patterns which occurs in the pollen tube tip growth. Therefore, we need a new model that can couple the spatial Ca^{2+} dynamics with the ROP1 dynamics in (2.10).

2.2 Interaction between ROP1 and Ca^{2+}

Several experimental studies have been conducted by Yang group to investigate the interaction between ROP1 signaling regulation and Ca^{2+} activities. Their experimental data [40, 12, 15, 16, 26] suggests that Ca^{2+} plays a important role in negative feedback of ROP1 regulation. Accordingly, Yan [40] proposed two possible hypotheses along with two

models to explain the inhibition effect of Ca^{2+} on ROP1: (1) Ca^{2+} promotes the disassembly of the apical F-actin, leading to the down-regulation of ROP1 activity by countering the F-actin-mediated positive feedback, which can be modeled as

$$\frac{dR}{dt} = \beta_R \times \max\{R_0 - R, 0\}\frac{\max\{C_0 - C, 0\}R}{R_0 C_0} - \alpha_R R \tag{2.11}$$

where β_R is ROP1 activation rate, α_R is ROP1 inactivation rate, R_0 is saturated ROP1 concentration in cell, and C_0 is high calcium threshold to decrease F-actin; (2) Ca^{2+} signaling might down-regulate ROP1 activity by activating negative regulators of ROP1, which can be modeled as

$$\frac{dR}{dt} = \beta_R \times \max\{R_0 - R, 0\}\frac{R}{R_0} - \alpha_R R f(C)$$

$$f(C) = \begin{cases} 1/M & C < C_{\min} \\ \frac{1}{M}\left[1 + \frac{(M-1)(C - C_{min})}{C_{max} - C_{min}}\right] & C_{min} \le C \le C_{max} \\ 1 & C > C_{max} \end{cases}$$

where M, C_{min} and C_{max} are piecewise activation of GAP by calcium.

On the other hand, ROP1 activates the RIC3 downstream pathway, which may trigger extracellular calcium influxes and activate calcium release from the internal calcium pool. Therefore, ROP1 activity promotes the increase in calcium level which can be modeled as

$$\frac{dC}{dt} = \beta_C \left[R(t - \tau) + b\right] - \alpha_C C$$

where β_C is calcium accumulation rate, α_C is calcium depletion, and τ is time delay between ROP1 and calcium accumulation. According to Yan's simulation and experimental results [40], time delay plays an important role in generation of oscillation.

2.3 Proposed Model

Studies show that negative feedback of ROP1 depends on Ca^{2+} near the plasma membrane, and that Ca^{2+} influx, which is activated by ROP1, have most effects on concentration of Ca^{2+} near the plasma membrane. In this dissertation, we propose a model to describes ROP1-Ca^{2+} feedback loop on plasma membrane.

As described previously, ROP1 polarization dynamics without spontaneous association can be simplified as three main procedures (see Fig. 2.2): (1) activation of inactive ROP1; (2) inhibition of active ROP1, which is forced by Ca^{2+}; (3) lateral diffusion of ROP1 along the membrane. The activation and inhibition of ROP1 can be considered as positive feedback and negative feedback, respectively. Both activation and inhibition rates are proportional to the substrate concentrations.

The lateral movement of ROP1 is modeled by a diffusion term $D_r \dfrac{\partial^2 R(x,t)}{\partial x^2}$, where D_r is the diffusion coefficient of ROP1. The ROP! activation rate is assumed to be proportional to R^α where the exponent satisfies $1 < \alpha < 2$ based on empirical studies. Since majority of inactive ROP1 are in cytoplasm with high mobility, the activation rate is proportional to the total amount of cytoplasmic molecules (*i.e.* $R_{tot} - \displaystyle\int_{-L}^{L} R(x,t)dx$) with rate k_{pf}. On the other hand, most active ROP1 are on the membrane. Since molecules on the membrane have much less mobility, the inhibition rate is proportional to the density of molecules (*i.e.* $R(x,t)$) at any given location with rate k_{nf}. Moreover, Ca^{2+} can inhibit ROP1 with some threshold k_c and an inhibition term $\frac{C^2}{C^2+k_c^2}$, which is a Hill function showing a transition from low inhibition rate at low Calcium density, to a high but bounded inhibition rate at a high Calcium density. The constant k_c is the half-saturation value in-

dicating the threshold between the low and high Calcium density. Hence $R(x,t)$ satisfies a reaction-diffusion equation with a nonlocal integral term:

$$\frac{\partial R(x,t)}{\partial t} = k_{pf} R^{\alpha}(x,t) \left(R_{total} - \int_{-L}^{L} R(x,t)dx \right) - k_{nf} R(x,t) \frac{C^2}{C^2 + k_c^2} + D_r \frac{\partial^2 R(x,t)}{\partial x^2}. \tag{2.12}$$

The Ca^{2+} activities can also be simplified by the following three procedures: (1) influx of Ca^{2+} which is regulated by ROP1 concentration; (2) efflux of Ca^{2+}; and (3) diffusion of Ca^{2+} along the membrane (see Fig.2.3). The diffusion of Ca^{2+} is given by

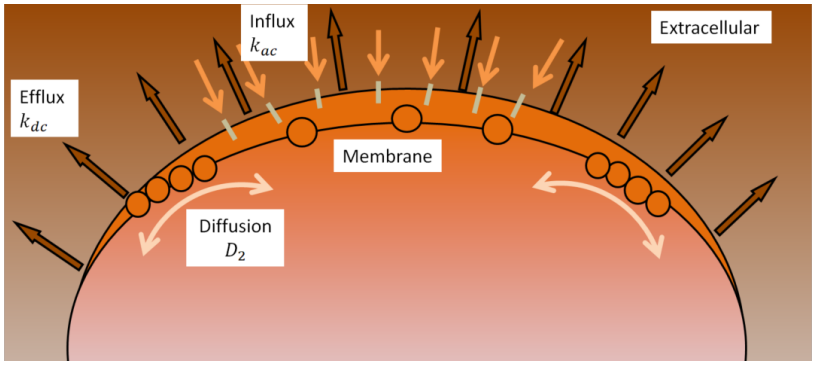

Figure 2.3: Ca^{2+} dynamics

$D_c \frac{\partial^2 C(x,t)}{\partial x^2}$, where D_c is the diffusion coefficient of Ca^{2+}. The Ca^{2+} ions could flow into the cell through Calcium channel on the membrane, and the Ca^{2+} influx is controlled by ROP1 with rate k_{ac}. Also there is a time delay τ in this promotion. In this work, we model Ca^{2+} promotion with $k_{ac}R(x,t-\tau)$ to show a linear response of Calcium influx to the ROP1 density. On the other hand, self-decay of Ca^{2+} is proportional to substrate concentration at a certain rate k_{dc}. Therefore, the Ca^{2+} activities are described by a reaction-diffusion

equation with time-delay:

$$\frac{\partial C(x,t)}{\partial t} = k_{ac}R(x,t-\tau) - k_{dc}C(x,t) + D_2\frac{\partial^2 C(x,t)}{\partial x^2}. \tag{2.13}$$

Note that ROP1 activates both ROP1 and Ca^{2+} growth, and Ca^{2+} inhibits both ROP1 and Ca^{2+} (see Fig. 2.4).

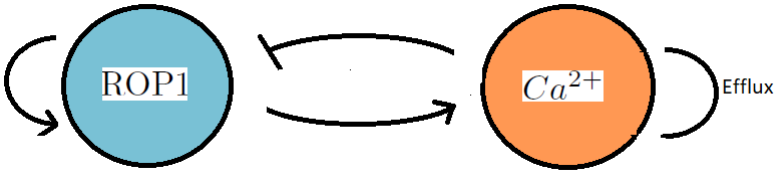

Figure 2.4: Interaction diagram of ROP1 and Ca^{2+}.

Putting 2.12 and 2.13 together with the proper initial conditions, we have the following full system for the interaction between the ROP1 and Ca^{2+} on the cell membrane:

$$\begin{cases} R_t = k_{pf}R^{\alpha}\left(R_{tot} - \int_{-L}^{L} R dx\right) - k_{nf}\dfrac{RC^2}{C^2+k_c^2} + D_r R_{xx}, & (x,t) \in (-L,L)\times(0,T), \\ C_t = k_{ac}R(x,t-\tau) - k_{dc}C + D_c C_{xx}, & (x,t) \in (-L,L)\times(0,T), \\ R_x(x,t) = C_x(x,t) = 0, & x = -L, L, \\ R(x,t) = R_0(x,t), & (x,t) \in (-L,L)\times[-\tau,0], \\ C(x,0) = C_0(x), & x \in (-L,L). \end{cases} \tag{2.14}$$

In fact, time delay is not necessary to generate oscillations in model (2.14) since the spatial information (diffusion term) introduces a kind of time delay in the dynamics.

Specifically, C_t function in model (2.14) is a heat equation $C_t = k_{ac}R - k_{dc}C + D_cC_{xx}$. Therefore, $C(x,t) = \int\int K(x-u, t-s)R(u-s)duds$, where $K(\dot{;}\dot{)}$ is a kernel function that averages R on its past values, which can be interpreted as a time delay effect. Therefore, in this dissertation we mainly work on the following model without time delay term:

$$\begin{cases} R_t = k_{pf}R^{\alpha}\left(R_{tot} - \int_{-L}^{L} R dx\right) - k_{nf}\dfrac{RC^2}{C^2 + k_c^2} + D_r R_{xx}, & (x,t) \in (-L,L) \times (0,T), \\ C_t = k_{ac}R(x,t) - k_{dc}C + D_cC_{xx}, & (x,t) \in (-L,L) \times (0,T), \\ R_x(x,t) = C_x(x,t) = 0, & x = -L, L, \\ R(x,0) = R_0(x), \quad C(x,0) = C_0(x), & x \in (-L,L). \end{cases} \tag{2.15}$$

Chapter 3

Analytic Study: Spatial-temporal dynamic of proposed model

It has been observed in experimental data that membrane-localized Ca^{2+} and ROP1 an oscillation of double-peak pattern which seems to be tightly correlated with ROP1 activity at the membrane both in time and space. Therefore, before moving on to parameter estimation procedure, it is necessary to verify that proposed model (2.15) is able to generate observed oscillation pattern of ROP1 and Ca^{2+} distribution on the membrane. In this chapter, we will analytically discuss spatial-temporal dynamic of solution to proposed model (2.15) under different condition of parameters. For this purpose, we first convert the equation into a dimensionless form, we introduce the normalized quantities:

$$\check{t} = k_{dc}t, \quad \check{x} = \sqrt{\frac{k_{dc}}{D_r}}x, \quad \check{R} = \frac{2LR}{R_{tot}}, \quad \check{C} = \frac{2Lk_{dc}C}{R_{tot}k_{ac}}, \tag{3.1}$$

$$k_1 = \frac{2Lk_{pf}}{k_{dc}}\left(\frac{R_{tot}}{2L}\right)^{\alpha}, \quad k_2 = \frac{k_{nf}}{2Lk_{pf}}\left(\frac{2L}{R_{tot}}\right)^{\alpha}, \quad k_3 = \frac{2Lk_ck_{dc}}{k_{ac}R_{total}}, \quad D = \frac{D_r}{D_c}, \tag{3.2}$$

$$\check{L} = L\sqrt{\frac{k_{dc}}{D_c}}, \quad \check{T} = k_{dc}T. \tag{3.3}$$

With these normalized quantities, the PDE model (2.15) is rewritten in the following normalized form:

$$\begin{cases} \check{R}_{\check{t}} = k_1\check{R}^{\alpha}\left(1 - \dfrac{1}{2\check{L}}\displaystyle\int_{-\check{L}}^{\check{L}} \check{R}d\check{x}\right) - k_1k_2\dfrac{\check{R}\check{C}^2}{\check{C}^2 + k_3^2} + D\check{R}_{\check{x}\check{x}}, & (\check{x},\check{t}) \in (-\check{L},\check{L}) \times (0,\check{T}), \\ \check{C}_{\check{t}} = \check{R}(\check{x},\check{t}) - \check{C} + \check{C}_{\check{x}\check{x}}, & (\check{x},\check{t}) \in (-\check{L},\check{L}) \times (0,\check{T}), \\ \check{R}(\check{x},0) = \check{R}_0(\check{x}), \quad \check{C}(\check{x},0) = \check{C}_0(\check{x}), & \check{x} \in (-\check{L},\check{L}). \end{cases} \tag{3.4}$$

Dropping the $\check{}$ in (3.4), we have the system

$$\begin{cases} R_t = k_1R^{\alpha}\left(1 - \frac{1}{2L}\displaystyle\int_{-L}^{L} Rdx\right) - k_1k_2\dfrac{RC^2}{C^2 + k_3^2} + DR_{xx}, & (x,t) \in (-L,L) \times (0,T), \\ C_t = R(x,t) - C(x,t) + C_{xx}, & (x,t) \in (-L,L) \times (0,T), \\ R_x(x,t) = C_x(x,t) = 0, & x = -L, L, \\ R(x,0) = R_0(x), \quad C(x,0) = C_0(x), & x \in (-L,L). \end{cases} \tag{3.5}$$

From now on, we will analyze the dynamics behavior of the simplified system (3.5). First, we will discuss about temporal dynamic of kinetic system. In the second section, we

will add diffusion and nonlocal term to kinetic system, and study how the spatial term changes the dynamics behavior of model (3.5).

3.1 Kinetic system

In system (3.5), if the initial conditions $(R_0(x,t), C_0(x))$ are spatially homogeneous, then the corresponding solution of (3.5) is also spatially homogeneous and it satisfies

$$\begin{cases} R_t = k_1 R^\alpha (1-R) - k_1 k_2 \dfrac{RC^2}{C^2+k_3^2}, \\ C_t = R(t) - C, \\ R(t) = R_0(t), \ \ t \in [-\tau, 0], \ \ C(0) = C_0. \end{cases} \tag{3.6}$$

The steady states of (3.6) satisfy

$$\begin{cases} k_1 R^\alpha (1-R) - k_1 k_2 \dfrac{RC^2}{C^2+k_3^2} = 0, \\ R - C = 0. \end{cases} \tag{3.7}$$

A nonnegative steady state is either the trivial one $(R, C) = (0, 0)$, or a positive one satisfying

$$R^{\alpha-1}(1-R) - k_2 \frac{C^2}{C^2+k_3^2} = 0, \ \ C = R. \tag{3.8}$$

Then (3.8) is equivalent to $C = R$ and

$$f(R) \equiv k_2 - R^{\alpha-3}(1-R)(R^2+k_3^2) = 0. \tag{3.9}$$

The following result shows the existence and exact multiplicity of roots R of (3.9), which also reveals the existence and exact multiplicity of steady states of (3.6) in form (R, R).

Proposition 1 *There exists a constant $k_{31} > 0$ such that*

1. *If $0 < k_3 < k_{31}$, then there exists $0 < k_{21} < k_{22}$ which depend on k_3 and α such that*

   (a) *when $0 < k_2 < k_{21}$, there is a unique positive root R_3 for* (3.9) *(see Fig. 3.1a);*

   (b) *when $k_2 > k_{22}$, there is a unique positive root R_1 for* (3.9) *(see Fig. 3.1e);*

   (c) *when $k_2 = k_{21}$ or $k_2 = k_{22}$, then there are exactly two positive roots R_1, R_3 satisfying $R_1 < R_3$ for* (3.9) *(see Fig. 3.1b and Fig. 3.1d);*

   (d) *when $k_{21} < k_2 < k_{22}$, there are exactly three positive roots R_1, R_2, R_3 satisfying $R_1 < R_2 < R_3$ for* (3.9) *(see Fig. 3.1c).*

2. *If $k_3 > k_{31}$, then for any $k_2 > 0$, there is a unique positive root R_1 for* (3.9) *(see Fig. 3.1f).*

The proof of Proposition 1 is given in Appendix. From Proposition 1, (3.6) possesses one, or two, or three positive steady states depending on the parameter values of k_2 and k_3. We denote the positive steady states of (3.6) by $(R_j, C_j) = (R_j, R_j)$ $(1 \le j \le 3)$, where R_j is the root of (3.9) as shown in Proposition 1, and $C_j = R_j$. Fig. 3.2 shows the regions of parameters (k_2, k_3) where (3.6) has 1 or 3 positive steady states. When $k_3 > k_{31}$, the bifurcation diagram in (k_2, R, C)-space is a monotone curve (see Fig. 3.3a and Fig. 3.3c), while when $0 < k_3 < k_{31}$, the corresponding bifurcation diagram is an S-shaped one with two saddle-node bifurcation points at $k_2 = k_{21}$ and $k_2 = k_{22}$ (see Fig. 3.3b). When the parameter k_2 varies, the bifurcation diagram depicts a typical hysteresis scenario with a bistable structure. Similar bifurcation structure have been found in various biological

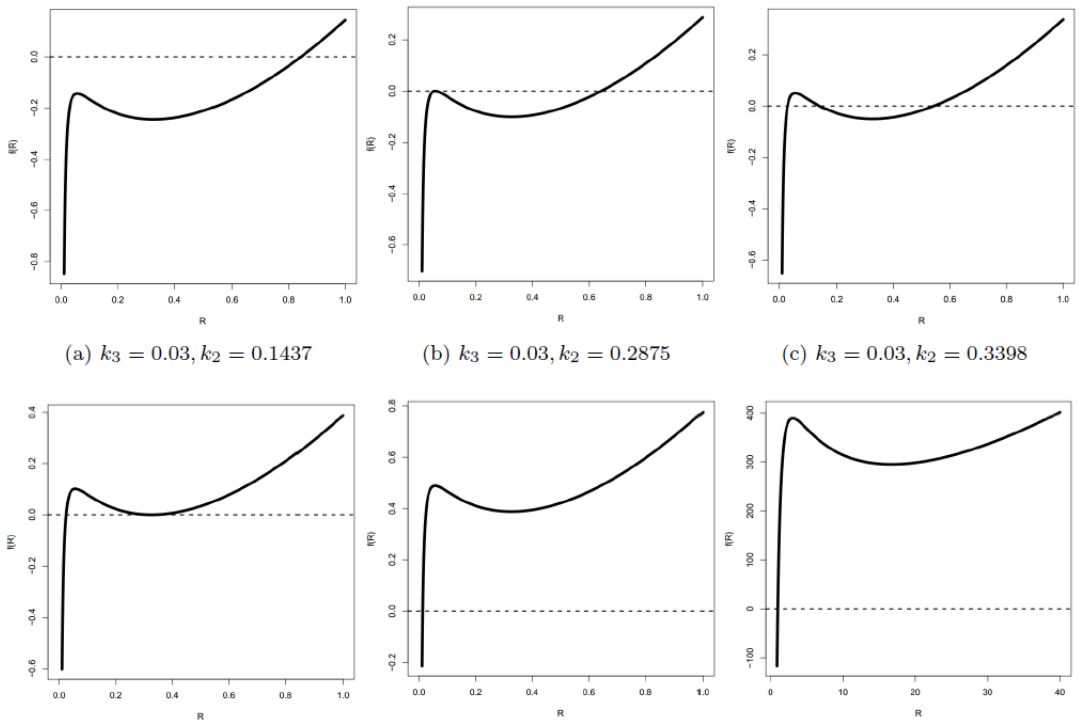

(a) $k_3 = 0.03, k_2 = 0.1437$ (b) $k_3 = 0.03, k_2 = 0.2875$ (c) $k_3 = 0.03, k_2 = 0.3398$

(d) $k_3 = 0.03, k_2 = 0.3881$ (e) $k_3 = 0.03, k_2 = 0.7762$ (f) $k_3 = 31.6228, k_2 = 1$

Figure 3.1: Graphs of $f(R)$ with $\alpha = 1.5$ and varying (k_2, k_3).

models of spruce budworm population [20], shallow lakes [29, 30], coral reef [17, 23], and forest and savanna [33, 34].

Next we consider the local stability of the steady states $(0,0)$ and (R_j, R_j) $(1 \leq j \leq 3)$ with respect to (3.6). First at steady state $(0,0)$, the Jacobian matrix is $\begin{pmatrix} 0 & 0 \\ 1 & -1 \end{pmatrix}$. Therefore we have two eigenvalues $\lambda_1 = 0$ and $\lambda_2 = -1 < 0$ which indicates that $(0,0)$ is a degenerate steady state. One can apply the theory of two-dimensional dynamical system to obtain the following description of the dynamics of (3.6) near $(0,0)$:

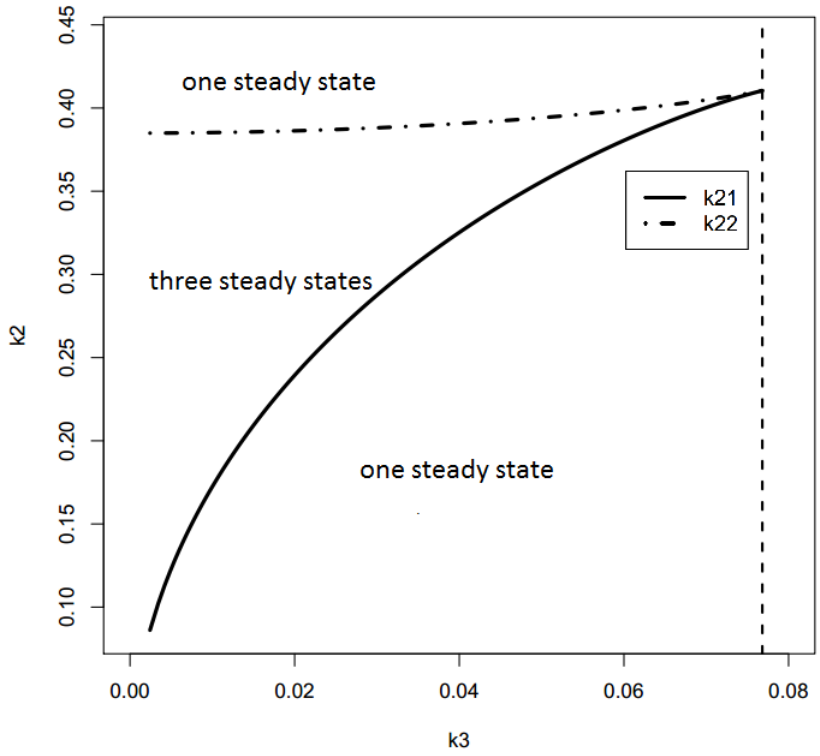

Figure 3.2: The number of positive steady state of system (2.5) for different values of (k_2, k_3) with $\alpha = 1.5$

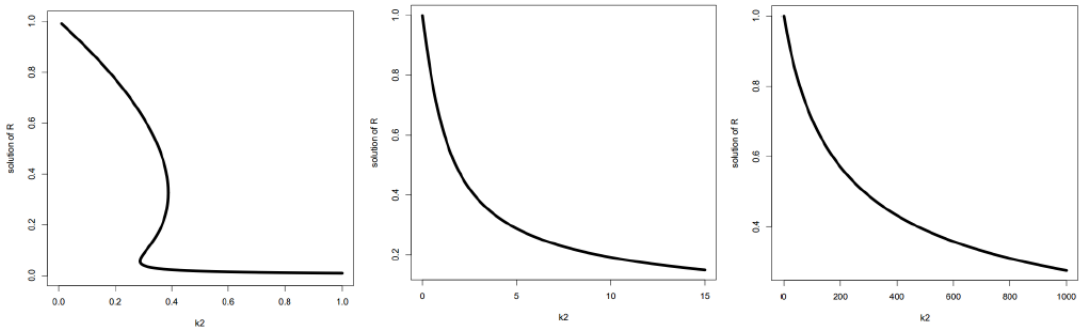

(a) $k_3 = 0.03$ (b) $k_3 = 1$ (c) $k_3 = 14.1421$

Figure 3.3: Bifurcation diagrams of system (2.5) with $\alpha = 1.5$

Proposition 2 *For any $k_1, k_2, k_3 > 0$, there exists a $\delta > 0$ such that in the neighborhood $B = \{(R, C) : 0 < R < \delta, 0 < C < \delta\}$ of $(0, 0)$,*

1. *(3.6) has a unique center manifold $W_c = \{(R, h_u(R)) : 0 < R < \delta\}$ such that $h_c(0) = h_c'(0) = 1$, and the orbit of (3.6) on W_c is unstable;*

2. *there exists a function $h_s : (0, \delta) \to (0, \delta)$ such that for any region $O = \{(R, C) : 0 \leq R \leq h_s(C), 0 < C < \delta\}$ is invariant, and for any $(R_0, C_0) \in O$, the solution $(R(t), C(t))$ of (3.6) with $(R(0), C(0)) = (R_0, C_0)$ satisfies $\lim_{t\to\infty}(R(t), C(t)) = (0, 0)$.*

3. *other orbits in B exhibits saddle behavior near $(0, 0)$, that is, the orbit does not approach $(0, 0)$ as $t \to \infty$, and for $t > T$, the orbit leaves the neighborhood B.*

The proof of Proposition 2 is given in Appendix. It shows that there is a "horn"-shaped region belonging to the basin of attraction of the origin $(0, 0)$. Indeed for any parameter values, if the initial value of Ca^{2+} C_0 is sufficiently large, then the solution will converge to $(0, 0)$ (see Fig 3.4). So our subsequent discussion will be for the remaining part of the phase portrait in which the orbits do not converge to $(0, 0)$.

For positive steady states, we linearize (3.6) at a steady state (R_j, R_j) $(j = 1, 2, 3)$, then we obtain the Jacobian matrix as

$$J(R_j, R_j) = \begin{pmatrix} k_1 R_j f_1'(R_j) & -k_1 R_j f_2'(R_j) \\ 1 & -1 \end{pmatrix}, \tag{3.10}$$

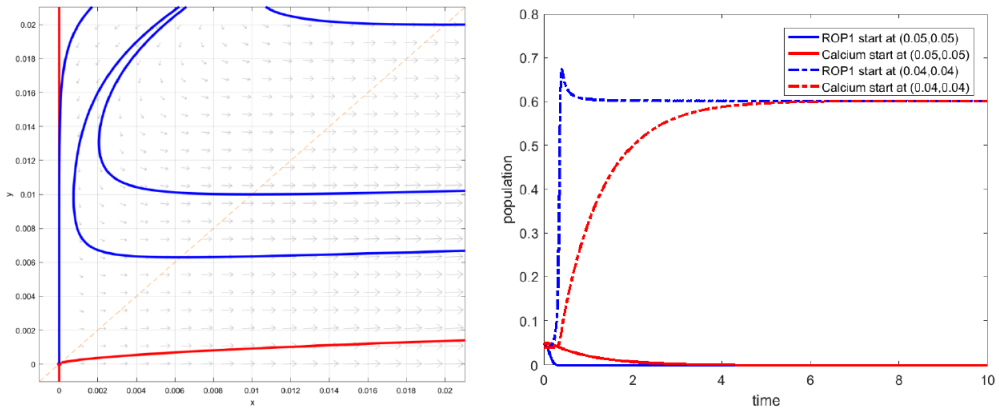

(a) Phase plane around (0,0).

(b) Different asymptotic behavior.

Figure 3.4: Dynamical behavior of (3.6) near $(0,0)$. Here $\alpha = 1.5$, $k_1 = 175$, k_2=0.31, k_3 = 0.0316, and the initial conditions for the solution orbits in the right panel are $(R(0), C(0)) = (0.05, 0.05)$ and $(0.04, 0.04)$

where

$$f_1(R) = R^{\alpha-1}(1-R), \quad f_2(R) = \frac{k_2 R^2}{R^2 + k_3^2}. \tag{3.11}$$

Hence we find that

$$Tr(J(R_j, C_j)) = k_1 R_j f_1'(R_j) - 1, \tag{3.12}$$

$$Det(J(R_j, C_j)) = k_1 R_j (f_2'(R_j) - f_1'(R_j)). \tag{3.13}$$

We recall that a steady state (R, R) of (3.6) is a sink or spiral sink if both eigenvalues of $J(R, R)$ are of negative real parts; it is a source or spiral source if both eigenvalues of $J(R, R)$ are of positive real parts; and it is a saddle if $J(R, R)$ has one positive and one negative eigenvalue. From the trace-determinant theory, it is easy to know that (R, R) is a sink or spiral sink if $Tr(J) < 0$ and $Det(J) > 0$; it is a source or spiral source if $Tr(J) > 0$ and $Det(J) > 0$; and it is a saddle if $Tr(J) \in R$ and $Det(J) < 0$.

For our next result regarding the local stability of the positive steady state (R_j, R_j)

$(j = 1, 2, 3)$ obtained above, we determine the stability using the trace and determinant of $J(R, C)$. We also observe that the steady states of (3.6) are independent of parameter k_1, but k_1 does affect the stability of steady states. For for fixed $\alpha \in (1, 2)$ and $k_3 > 0$, and any $0 < R < 1$, the pair (R, R) can be a steady state of (3.6) for exactly one value of $k_2 > 0$ by the relation (from (3.7)):

$$k_2 = R^{\alpha-3}(1 - R)(R^2 + k_3^2). \tag{3.14}$$

That is, for fixed $\alpha \in (1, 2)$ and $k_3 > 0$, the set of steady states of (3.6) can be parameterized by R as a bifurcation diagram (see Fig. 3.3):

$$\Sigma = \{(k_2(R), R, R) : R \in (0, 1)\}, \tag{3.15}$$

where $k_2(R)$ is given by (3.14). Now we state our results on the local stability of the positive steady state in terms of parametrization in (3.15).

Theorem 3 *Suppose that $\alpha \in (1, 2)$ and $k_3 > 0$, and $k_2(R)$ is defined as in (3.14) so that (R, R) is a positive steady state of (3.6) with $k_2 = k_2(R)$ for $0 < R < 1$.*

1. *If $k_3 > k_{31}$ (defined in Proposition 1), then $Det(R, R) > 0$ for any $R \in (0, 1)$; and if $0 < k_3 < k_{31}$, then there exist $r_1, r_2 > 0$ such that $Det(R, R) > 0$ for $R \in (0, r_1) \cup (r_2, 1)$, and $Det(R, R) < 0$ for $R \in (r_1, r_2)$. Here $k_2(r_1) = k_{21}$ and $k_2(r_2) = k_{22}$ (defined in Proposition 1).*

2. *Define*

$$k_{11} = \frac{\alpha^{2\alpha-1}}{(\alpha - 1)^{2\alpha-1}}. \tag{3.16}$$

If $0 < k_1 < k_{11}$, then $Tr(R, R) < 0$ for any $R \in (0, 1)$; and if $k_1 > k_{11}$, then there exist $0 < \tilde{R}_1 < \tilde{R}_2$ such that $Tr(R, R) < 0$ for $R \in (0, \tilde{R}_1) \cup \tilde{R}_2, 1)$, and $Tr(R, R) > 0$

for $R \in (\tilde{R}_1, \tilde{R}_2)$.

According to Theorem 3, we can have following results for $0 < k_3 < k_{31}$, when there are at least one and at most three positive steady state of (3.6):

1. The middle positive steady state (R_2, R_2) is always a saddle.

2. The largest positive steady state (R_3, R_3) or the smallest one (R_1, R_1) is either a sink or spiral sink, or a source or spiral source, but it is not a saddle.

3. Define

$$I_s = ((0, r_1) \cup (r_2, 1)) \cap ((0, \tilde{R}_1) \cup (\tilde{R}_2, 1)). \tag{3.17}$$

   Then when $R \in I_s$, the positive steady state (R, R) is a sink or spiral sink which is locally asymptotically stable. In particular, when $R > 0$ is sufficiently small or when R is close to 1, then (R, R) is a sink or spiral sink.

4. Define

$$I_u = ((0, r_1) \cup (r_2, 1)) \cap (\tilde{R}_1, \tilde{R}_2). \tag{3.18}$$

   Then when $R \in I_u$, the positive steady state (R, R) is a source or spiral source which is unstable.

The proof of Theorem 3 is in the Appendix. Note that the stable regime I_s is always not an empty set as it contains a right neighborhood of $R = 0$ and a left neighborhood of $R = 1$, but I_s may also contain another connected component which is disconnected from $R = 0$ and $R = 1$. The unstable regime I_u could be empty, and that happens when $0 < k_1 < k_{11}$. However I_u is not empty when k_1 is chosen as sufficiently large. Indeed for

fixed $k_3 > 0$, one has that

$$\lim_{k_1\to\infty} \tilde{R}_1 = 0, \quad \lim_{k_1\to\infty} \tilde{R}_2 = \frac{\alpha - 1}{\alpha}. \tag{3.19}$$

The local stability analysis given in Theorem 3 can be used to guide our classification of global dynamics of (3.6). A complete classification in terms of parameters (k_1, k_2, k_3) is rather exhaustive and it will be given in Appendix. Here we focus on in which cases, the system (3.6) shows sustained temporal oscillations. The follow result classifies the occurrence of Hopf bifurcations in terms of parameters k_1, k_2 and k_3.

Proposition 4 *Suppose that $\alpha \in (1, 2)$, and define*

$$g(R) = R^{\alpha-1}[(\alpha - 1) - \alpha R]. \tag{3.20}$$

Let k_{31}, k_{11} be defined as in Proposition 1 and (3.16) respectively, and let $r_1, r_2, \tilde{R}_1, \tilde{R}_2 > 0$ be defined in Theorem 3. We also define $\tilde{k}_{21} = k_2(\tilde{R}_1)$ and $\tilde{k}_{22} = k_2(\tilde{R}_2)$.

1. *If $k_3 > k_{31}$, (3.6) has a unique positive steady state for all $k_1, k_2 > 0$. Moreover*

   (a) *When $k_1 < k_{11}$, the unique positive steady state of (3.6) is a sink or spiral sink for any $k_2 > 0$. (see Fig. 3.5a)*

   (b) *When $k_1 > k_{11}$, the unique positive steady state of (3.6) is a sink or spiral sink for $k_2 \in (0, \tilde{k}_{22}) \cup (\tilde{k}_{21}, \infty)$, and is unstable for $k_2 \in (\tilde{k}_{22}, \tilde{k}_{21})$; Hopf bifurcations occur at $k_2 = \tilde{k}_{21}$ and $k_2 = \tilde{k}_{22}$, and there exists at least one periodic orbit for $k_2 \in (\tilde{k}_{22}, \tilde{k}_{21})$. (see Fig. 3.5b)*

2. *If $0 < k_3 < k_{31}$, (3.6) has at least one and at most three positive steady states, and*

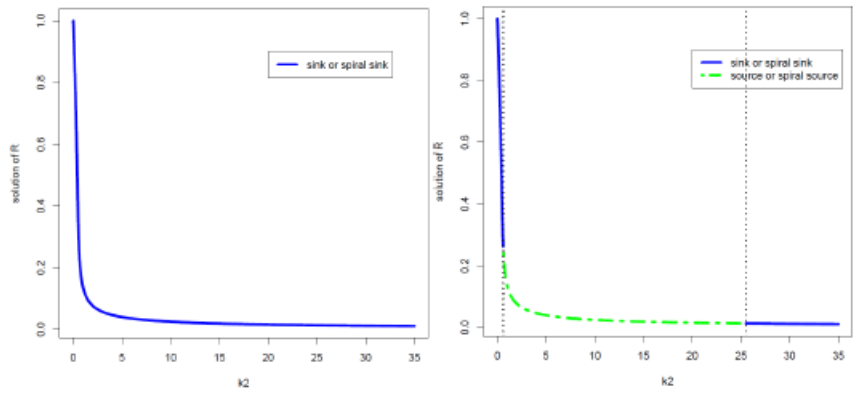

(a) $k_3 = 0.2$, $k_1 = 4.5$

(b) $k_3 = 0.2$, $k_1 = 18$

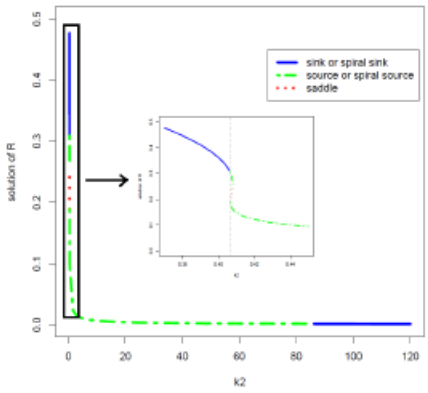

(c) $k_3 = 0.0742$, $k_1 = 50$

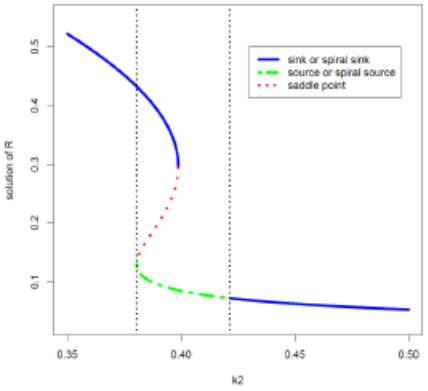

(d) $k_3 = 0.06$, $k_1 = 9.5$

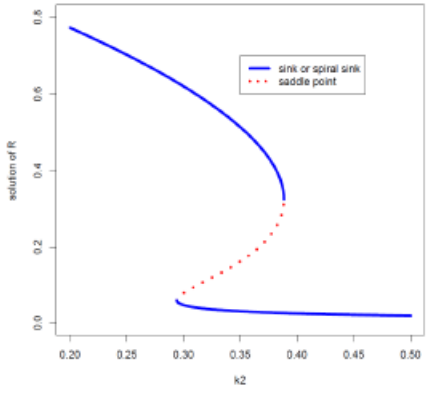

(e) $k_3 = 0.0316$, $k_1 = 9.5$

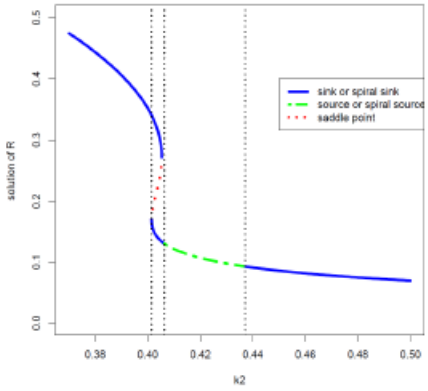

(f) $k_3 = 0.0707$, $k_1 = 9.1$

Figure 3.5: Possible bifurcation diagrams of (3.6) with parameter k_2. Here the horizontal axis is k_2 and the vertical axis is R, $\alpha = 1.5$ and k_1, k_3 are specified for each diagram.

when there exist three positive steady states, the middle one (R_2, R_2) *is a saddle. Moreover*

(c) If $k_1 > 1/g(r_2)$*, then Hopf bifurcations occur at* $\tilde{k}_{22}$ *on the large steady state* (R_3, R_3) *and at* $\tilde{k}_{21}$ *on the small steady state* (R_1, R_1) *of* (3.6)*. (see Fig. 3.5c)*

(d) If $1/g(r_1) < k_1 < 1/g(r_2)$*, then the large positive steady state* (R_3, R_3) *is always a sink or spiral sink, and a Hopf bifurcation occurs at* $\tilde{k}_{21}$ *on the small positive steady state* (R_1, R_1) *of* (3.6)*. (see Fig. 3.5d)*

(e) Define

$$\tilde{k}_3 = \sqrt{\frac{(\alpha-1)^5}{\alpha^3(-\alpha^2+5\alpha-2)}}. \tag{3.21}$$

If $0 < k_1 < 1/g(r_1)$ *and* $0 < k_3 < \tilde{k}_3$*, or* $0 < k_1 < k_{11}$ *and* $\tilde{k}_3 < k_3 < k_{31}$*, then both the large positive steady state* (R_3, R_3) *and the small positive steady state* (R_1, R_1) *are always sink or spiral sink, and there is no Hopf bifurcation occurring. (see Fig. 3.5e)*

(f) If $k_{11} < k_1 < 1/g(r_1)$ *and* $\tilde{k}_3 < k_3 < k_{31}$*, then the large positive steady state* (R_3, R_3) *is always a sink or spiral sink, and Hopf bifurcations occur at* $\tilde{k}_{21}$ *and* $\tilde{k}_{22}$ *on the small positive steady state* (R_1, R_1) *of* (3.6)*. (see Fig. 3.5f)*

The proof of Proposition 4 is in the Appendix. The six bifurcation diagrams of steady states and Hopf bifurcations are shown in Fig. 3.5, and a classification of (k_3, k_1) parameter regions in which Hopf bifurcations with parameter k_2 can occur is summarized in Fig. 3.6.

Guided by bifurcation diagrams above, there are following six possible dynamic

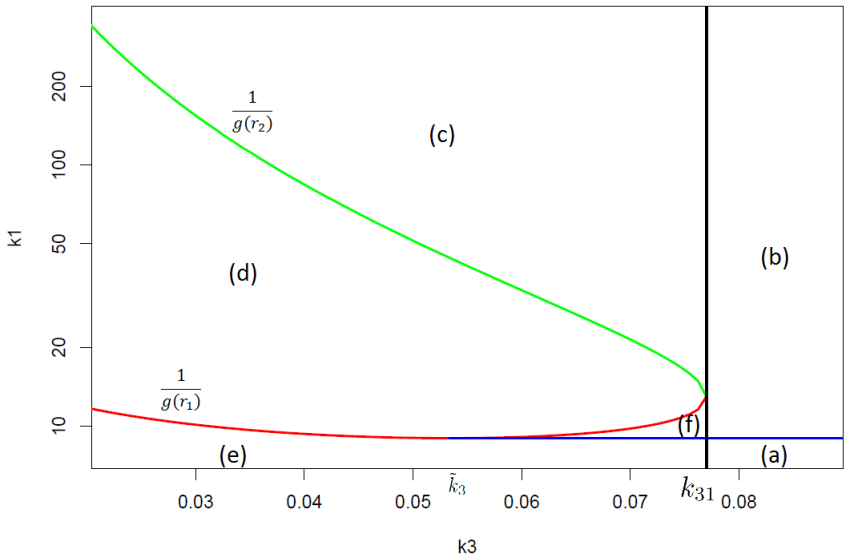

Figure 3.6: Classification of (k_3, k_1) parameter region for Hopf Bifurcation occurrence with $\alpha = 1.5$.

phase planes and dynamics of $(R(t), C(t))$ solutions. Note that from Proposition 2, there is always a region of initial conditions that orbits starting from there converge to the origin $(0, 0)$ as $t \to \infty$. That region is bounded below by the maximum center manifold. So in the following we only describe the dynamics below the maximum center manifold.

1. There is only one positive steady state R_1, which is a sink or spiral sink. All the solutions will converge to R_1. For example, when $\alpha = 1.5$, $k_1 = 9.5$, $k_2 = 1$, $k_3 = 0.06$, there is a spiral sink at $R_1 = 0.02587$. (See Fig 3.7 upper row)

2. There is only one positive steady state R_1, which is a source or spiral source, and there is a limit cycle around R_1. For example, when $\alpha = 1.5$, $k_1 = 15$, $k_2 = 1$, $k_3 = 0.06$, there is a limit cycle around positive steady state $R_1 = 0.02587$.(See Fig 3.7 lower row)

3. There are three positive steady states R_1, R_2 and R_3; R_2 is a saddle point while R_1 and R_3 are sinks or spiral sinks. A solution will converge to either R_1or R_3 depending on the initial value. For example, when $\alpha = 1.5$, $k_1 = 5$, $k_2 = 0.4035$, $k_3 = 0.0707$, there are two sinks, $R_1 = 0.1418$ and $R_3 = 0.3194$. The solution will converge to $R_1 = 0.1418$ if initial value is $(R(0), C(0)) = (0.1, 0.4)$ while to $R_3 = 0.3194$ if $(R(0), C(0)) = (0.4, 0.1)$. (See Fig 3.8)

4. There are three positive steady states R_1, which is a source, R_2, which is a saddle point, R_3, which is a global sink. Whatever initial value is, the solution will converge to R_3. For example, when $\alpha = 1.5$, $k_1 = 12$, $k_2 = 0.31$, $k_3 = 0.0316$, the sink $R_3 = 0.6013$ attracts most of initial conditions, and Fig 3.9 shows an orbit connecting R_1 to R_3. It is also possible that there is a limit cycle around R_1, but the parameter range for that case is not robust.

5. There are three positive steady states R_1, R_2 and R_3. R_2 is a saddle point while R_1 and R_3 are source or spiral source. Again the parameter range supporting such dynamics is not robust enough so we do not include a phase portrait for that case here.

3.2 Diffusion Effect (Joint Work with Dr. Qingyan Shi)

In this section, we shall show that spatiotemporal pattern formation is possible for (3.5) as a combined effect of diffusion, kinetic dynamics discussed in Section 3.1, and also

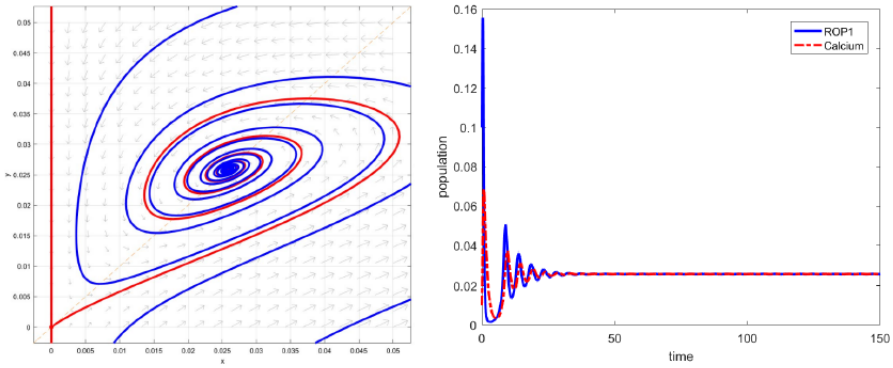

(a) Phase plane

(b) Solution with $(R(0), C(0)) = (0.1, 0.01)$

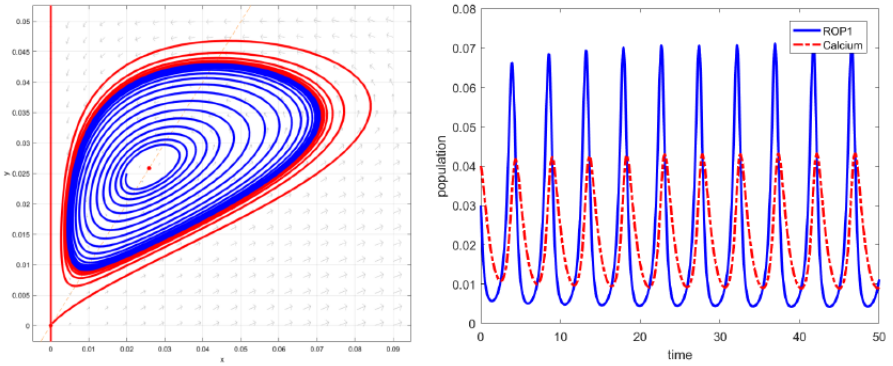

(c) Phase plane

(d) Solution with $(R(0), C(0)) = (0.03, 0.04)$

Figure 3.7: Dynamic behavior of (3.6) when $\alpha = 1.5$, $k_2 = 1$, $k_3 = 0.06$; Upper:$k_1 = 9.5$; Lower: $k_1 = 15$.

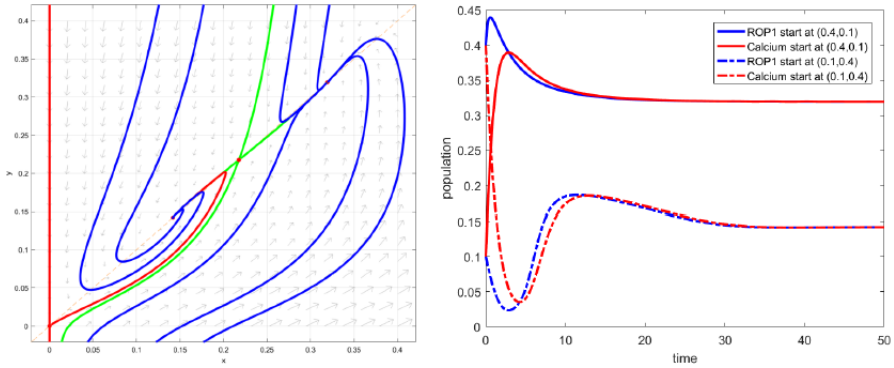

(a) Phase plane

(b) Solutions with $(R(0), C(0)) = (0.4, 0.1)$ and $(0.1, 0.4)$.

Figure 3.8: Dynamic behavior of (3.6) when $\alpha = 1.5$, $k_1 = 5$,$k_2 = 0.4035$, $k_3 = 0.0707$.

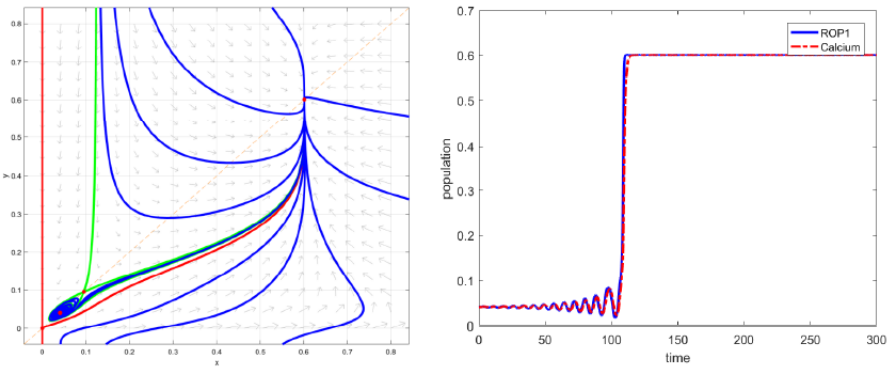

(a) Phase plane (b) Solution with $(R(0), C(0)) = (0.04, 0.04)$

Figure 3.9: Dynamic behavior of (3.6) when $\alpha = 1.5$, $k_1 = 12$,$k_2 = 0.31$, $k_3 = 0.0316$.

the nonlocal integral term.

It is easy to see that a steady state $(R_*,\ R_*)$ of (3.6) is a constant steady state solution of (3.5). Linearizing Eq. (3.5) at a constant steady state $(R_*,\ R_*)$, we obtain the following eigenvalue problem which determines the linear stability of the constant steady state:

$$\begin{cases} \mu\phi = D\phi_{xx} + (k_1 R_* f_1'(R_*) + k_1 R_*^\alpha)\,\phi - k_1 R_* f_2'(R_*)\psi - k_1 R_*^\alpha \dfrac{1}{2L}\displaystyle\int_{-L}^{L} \phi dx, & x \in (-L, L), \\ \mu\psi = \psi_{xx} + \phi - \psi, & x \in (-L, L), \\ \phi_x(x) = \psi_x(x) = 0, & x = -L, L, \end{cases} \tag{3.22}$$

where $f_1(R)$ and $f_2(R)$ are defined in (3.11). The eigenvalue problem (3.22) can be considered in the real-valued Sobolev space with the Neumann Boundary problem $X = \{(\phi, \psi) \in H^2(-L, L) \times H^2(-L, L) :\ R_x(\pm L) = C_x(\pm L) = 0\}$, and the eigenvalues of the diffusion

operator $u \mapsto -u''$ on X are

$$\lambda_n = \left(\frac{n\pi}{2L}\right)^2, \ n \in \mathbb{N}_0 := \{0, 1, 2, \cdots\}, \tag{3.23}$$

and the corresponding eigenfunctions are

$$\varphi_n(x) = \begin{cases} \cos(\sqrt{\lambda_n}x), & n = 0, 2, 4, \cdots, \\ \\ \sin(\sqrt{\lambda_n}x), & n = 1, 3, 5, \cdots. \end{cases} \tag{3.24}$$

The following lemma shows that the eigenvalue problem (3.22) can be solved through a Fourier decomposition of the eigenfunction and it is reduced to eigenvalues of infinitely many 2×2 matrices.

Lemma 5 *Let λ_n and $\varphi_n(x)$ be defined by* (3.23) *and* (3.24) *respectively, and let (R_*, R_*) be a constant steady state of Eq.* (3.5) *with R_* satisfying Eq.* (3.9)*. Define*

$$\begin{aligned} J_0 &= \begin{pmatrix} k_1 R_* f_1'(R_*) & -k_1 R_* f_2'(R_*) \\ \\ 1 & -1 \end{pmatrix}, \\ J_n &= \begin{pmatrix} -D\lambda_n + k_1 R_* f_1'(R_*) + k_1 R_*^{\alpha} & -k_1 R_* f_2'(R_*) \\ \\ 1 & -\lambda_n - 1 \end{pmatrix}, \ n = 1, 2, 3 \cdots, \end{aligned} \tag{3.25}$$

then we have

(i) if μ is an eigenvalue of (3.22)*, then there exists $n \in \mathbb{N}_0$ such that μ is an eigenvalue of J_n;*

(ii) (R_*, R_*) is locally asymptotically stable when the eigenvalues of J_n for all $n \in \mathbb{N}_0$ have negative real parts, and it is unstable when there exists some $n \in \mathbb{N}_0$ such that J_n has at least one eigenvalue with positive real part.

From Lemma 5, the eigenvalues of (3.22) are the eigenvalues of J_n, which are determined by the characteristic equation

$$\Gamma_n(\mu) = \mu^2 - T_n\mu + D_n = 0, \tag{3.26}$$

where

$$T_0 = k_1 R_* f_1'(R_*) - 1, \quad D_0 = k_1 R_*(f_2'(R_*) - f_1'(R_*)),$$

and for $n \geq 1$,

$$T_n = -(D+1)\lambda_n + k_1 R_* f_1'(R_*) + k_1 R_*^\alpha - 1,$$

$$D_n = D\lambda_n^2 + \left(D - k_1 R_* f_1'(R_*) - k_1 R_*^\alpha\right)\lambda_n + k_1 R_*(f_2'(R_*) - f_1'(R_*)) - k_1 R_*^\alpha.$$

Following the approach in [37, 44], the condition for the occurrence of a Hopf bifurcation near (R_*, R_*) is that there exist a pair of purely imaginary eigenvalues $\pm i\omega_n$ with $\omega_n > 0$ such that Eq. (3.26) holds, which is equivalent to that there exists $n \in \mathbb{N}_0$ such that

(H) $T_n = 0$, $D_n > 0$, and $T_i \neq 0$, $D_i \neq 0$ for $i \neq n$.

Also, we need to the verify the transversality condition which is $\frac{d\mathcal{R}e(\mu)}{dk_1} \neq 0$ for Hopf bifurcation is satisfied. By the fact that $\mathcal{R}e(\mu) = T_n/2$, we obtain that

$$\frac{d\mathcal{R}e(\mu)}{dk_1} = R_* f_1'(R_*) + R_*^\alpha = (\alpha - 1)R_*^{\alpha-1}(1 - R_*) > 0,$$

as $0 < R_* < 1$. Therefore, the transversality condition holds and Hopf bifurcations indeed occur at the following defined bifurcation points.

Here we choose k_1 the as bifurcation parameter, while one can also use other parameter as the bifurcation parameter. Then we have the spatially homogeneous and

non-homogeneous Hopf bifurcation points:

$$k_{1H}^{(0)} = \frac{1}{R_* f_1'(R_*)}, \;\; k_{1H}^{(n)} = \frac{1 + (D+1)\lambda_n}{R_* f_1'(R_*) + R^\alpha}, \; n \in \mathbb{N}, \tag{3.27}$$

provided that $k_2 \in (k_2^*, +\infty)$ such that $R_* f_1'(R_*) > 0$ which is necessary for the homogeneous Hopf bifurcation, where

$$k_2^* = k_2 \left(\frac{\alpha - 1}{\alpha} \right) \tag{3.28}$$

with $k_2(R)$ defined by (3.14). Also, notice that $R_* f_1'(R_*) + R^\alpha = (\alpha - 1) R_*^{\alpha - 1}(1 - R_*) > 0$ holds for any $R_* \in (0, 1)$, thus $k_{1H}^{(n)} > 0$. To sum up the discussion, we have the following lemma.

Lemma 6 *For fixed parameters k_3, D in system* (3.5) *and let k_2^* and $k_{1H}^{(n)}, n \in \mathbb{N}_0$ be defined by* (3.28) *and* (3.27) *respectively, then we have*

(i) when $k_2 \in (0, k_2^*)$, the spatially homogeneous Hopf bifurcation does not occur, but system (3.5) *undergoes a spatially non-homogeneous Hopf bifurcation at $k_1 = k_{1H}^{(n)}$ defined in* (3.27) *for each $n \in \mathbb{N}$;*

(ii) when $k_2 \in (k_2^*, +\infty)$, system (3.5) *undergoes a spatially homogeneous Hopf bifurcation at $k_1 = k_{1H}^{(0)}$ and a spatially non-homogeneous Hopf bifurcation at $k_1 = k_{1H}^{(n)}$ for each $n \in \mathbb{N}$.*

Similarly a steady state bifurcation occurs when

(S) $D_n = 0$, $T_n \neq 0$, and $T_i \neq 0$, $D_i \neq 0$, for $i \neq n$,

holds for some $n \in \mathbb{N}$, which is also called the diffusion-driven instability developed by Turing [36]. According to the condition (S), by taking k_1 as the bifurcation parameter, we

can obtain the following bifurcation points for the Turing instability:

$$k_{1S}^{(n)} = \frac{D(\lambda_n^2 + \lambda_n)}{(R_* f_1'(R_*) + R_*^\alpha)\lambda_n + R_*(f_1'(R_*) - f_2'(R_*)) + R_*^\alpha}, \ n \in \mathbb{N}. \tag{3.29}$$

Note that $k_{1S}^{(n)}$ may not be positive, but there exist a $N \in \mathbb{N}$ such that $k_{1S}^{(n)} > 0$ when $n > N$ and a steady state bifurcation indeed occurs at $k_1 = k_{1S}^{(n)}$ when $n > N$. According to [44], we also need to the verify the transversality condition which is $\frac{dD_n}{dk_1} \neq 0$ for the steady state bifurcation is satisfied. By a direct calculation, we have

$$\frac{dD_n}{dk_1} = -(R_* f_1'(R_*) + R_*^\alpha)\lambda_n + R_*(f_2'(R_*) - f_1'(R_*) - R^{\alpha-1}) < 0.$$

The Hopf bifurcation points defined in (3.27) and the steady state bifurcation points defined in (3.29) provide theoretical parameter values where spatial/temporal patterns for system (3.5) can emerge. In the remaining part of this section, we take some different values of k_1, k_3 and the spatial domain length L to numerically demonstrate possible bifurcations and rich dynamical behavior of model (3.5).

Example 7 *We choose* $k_2 = 1, \ k_3 = 0.06, \ \alpha = 1.5, \ L = 0.5\pi$. *In this case there is a unique constant steady state* $(R_*, R_*) = (0.0259, 0.0259)$ *which is determined by Eq.* (3.9). *According to Proposition 4,* $(0.0259, 0.0259)$ *is locally asymptotically stable for* $k_1 \in (0, k_1^*)$ *and unstable for* $k_1 \in (k_1^*, +\infty)$ *with* $k_1^* = 13.4744$ *being the homogeneous Hopf bifurcation point of the kinetic system* (3.10). *Then, by* (3.27) *and* (3.29), *we can compute the bifurcation points as*

$$k_{1H}^{(0)} = k_1^* = 13.4744, \ k_{1H}^{(n)} = 12.7578(1 + (D+1)n^2), \ k_{1S}^{(n)} = \frac{D(n^4 + n^2)}{0.0784n^2 - 0.1822}. \tag{3.30}$$

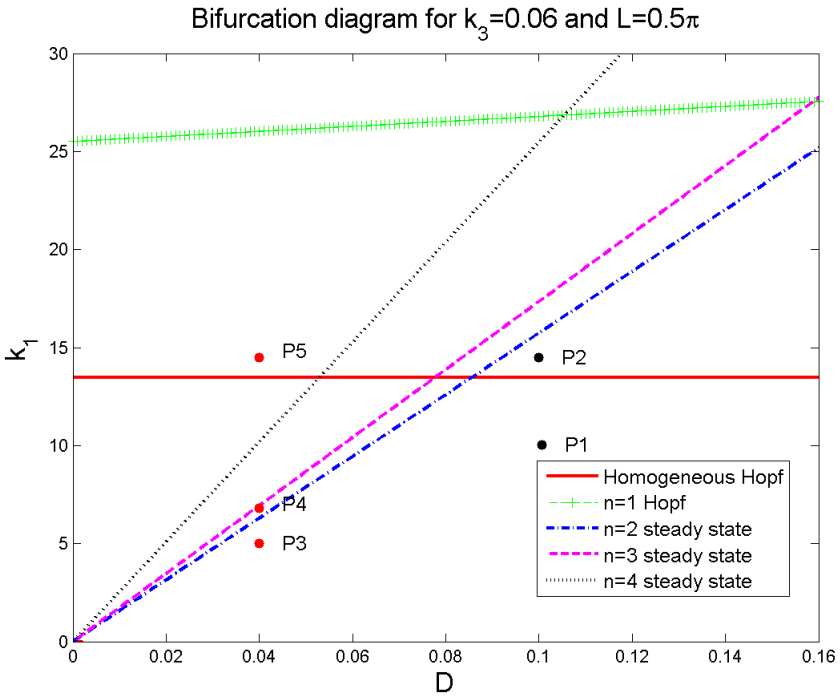

Figure 3.10: Steady state and Hopf bifurcation diagram for (3.5) on $D - k_1$ plane with $k_2 = 1$, $k_3 = 0.06$, $\alpha = 1.5$, $L = 0.5\pi$. We choose six points in $D - k_1$ plane to perform the numerical simulations: $P1 = (0.1, 10)$, $P2 = (0.1, 14.5)$, $P3 = (0.04, 5)$, $P4 = (0.04, 7)$, $P5 = (0.04, 14.5)$.

The bifurcation curves in (3.30) are plotted in Fig. 3.10 in $D - k_1$ plane, and this diagram serves as a guidance map for the different spatiotemporal patterns shown below. Fig. 3.11 demonstrates the situation when $D = 0.1$ and $k_1 = 10$ ($P1$) or $k_1 = 14.5$ ($P2$) in Fig. 3.10. For parameter value at $P1$, the constant steady state $(0.0259, 0.0259)$ is locally stable under a small random perturbation around the steady state (Fig. 3.11a,b); while a spatially homogeneous time-periodic orbit arises when k_1 crosses the homogeneous Hopf bifurcation line $k_1 = k_{1H}^{(0)}$ and reaches $P2$ (Fig. 3.11c,d).

For a smaller diffusion rate $D = 0.04$, spatially non-homogeneous steady states and periodic orbits can be generated when k_1 increases (see from Fig. 3.10). When $k_1 = 5$

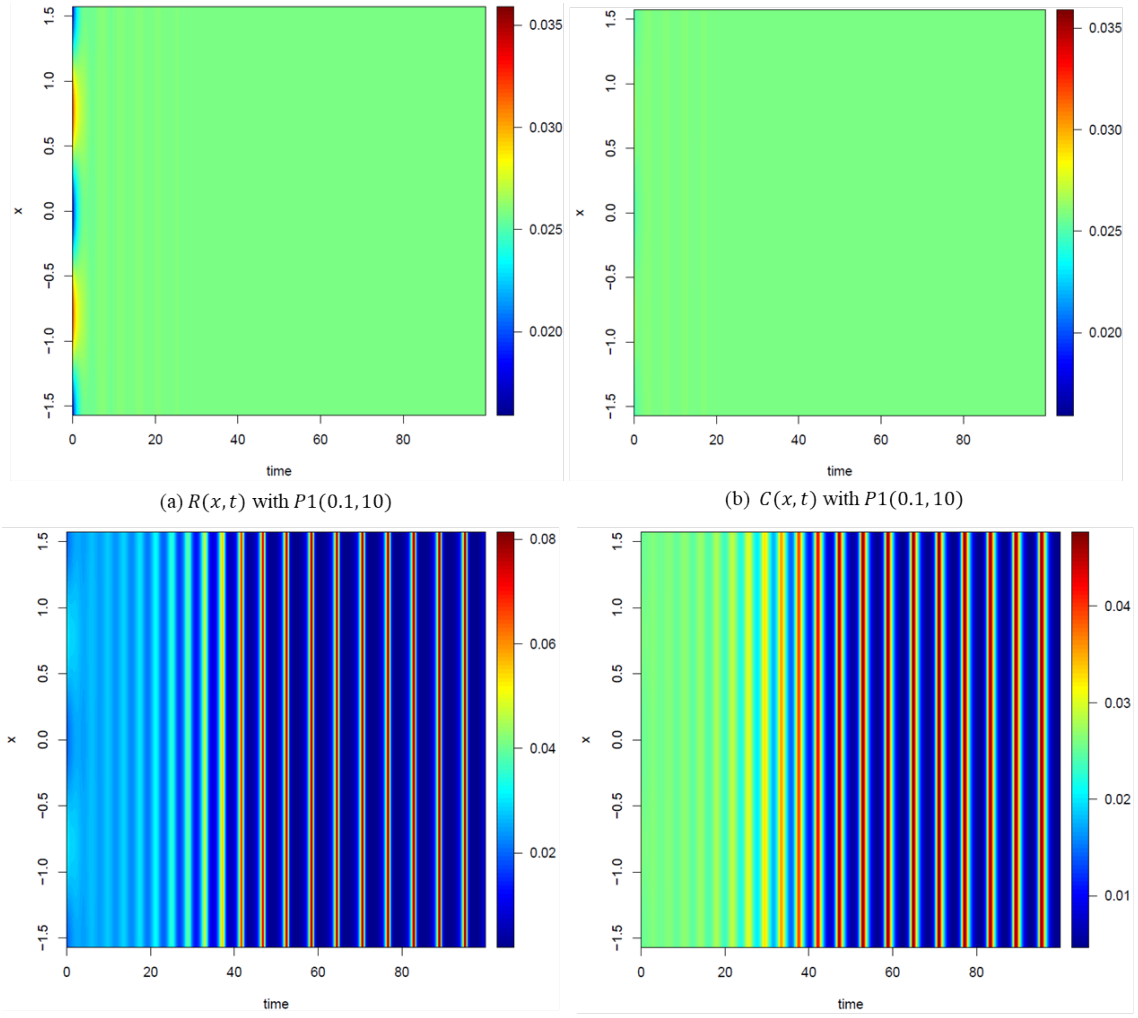

(a) $R(x,t)$ with $P1(0.1,10)$

(b) $C(x,t)$ with $P1(0.1,10)$

(c) $R(x,t)$ with $P2(0.1,14.5)$

(d) $C(x,t)$ with $P2(0.1,14.5)$

Figure 3.11: The dynamics of (3.5) when $D = 0.1,\ k_2 = 1,\ k_3 = 0.06,\ L = 0.5\pi$.

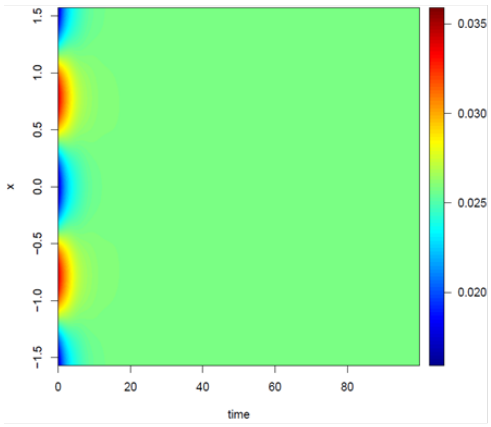

(a) $R(x,t)$ with $P3(0.04, 5)$

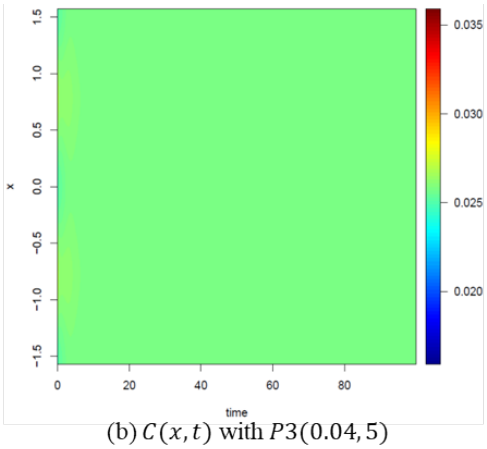

(b) $C(x,t)$ with $P3(0.04, 5)$

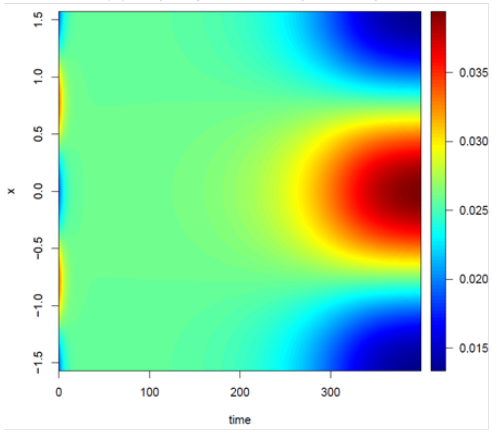

(c) $R(x,t)$ with $P4(0.04, 7)$

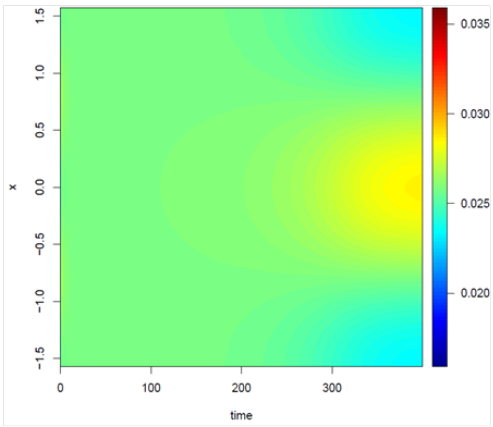

(d) $C(x,t)$ with $P4(0.04, 7)$

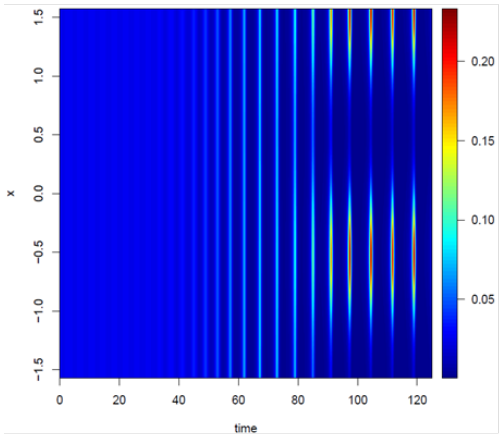

(e) $R(x,t)$ with $P5(0.04, 14.5)$

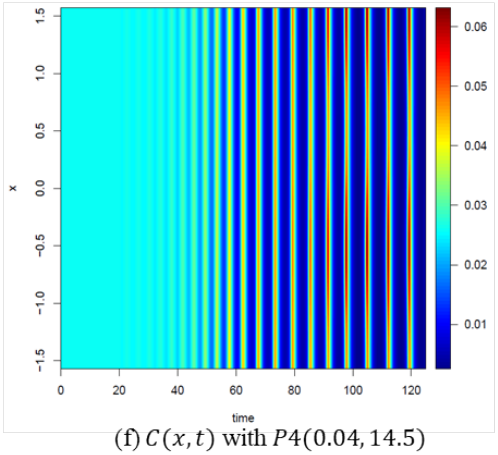

(f) $C(x,t)$ with $P4(0.04, 14.5)$

Figure 3.12: The dynamics of Eq. (3.5) when $D = 0.04,\ k_2 = 1,\ k_3 = 0.06,\ L = 0.5\pi$.

($P3$), the constant steady state is stable under a small perturbation (see Fig. 3.12a,b); when $k_1 = 7$ ($P4$), a mode-2 Turing pattern (spatially non-homogeneous steady state) is observed (see the Fig. 3.12c,d). Finally if k_1 crosses the homogeneous Hopf bifurcation line $k_1 = k_{1H}^{(0)}$ to $k_1 = 14.5$ ($P5$), then spatiotemporal patterns (spatially non-homogeneous periodic orbits) are observed (see Fig. 3.12e,f).

In this example, the homogeneous Hopf bifurcation curve ($n = 0$) and the steady state bifurcation curve with lowest n ($n = 2$) are where stability switches occur. For parameter values below both curves ($P1, P3$), the constant steady state is stable; for the one above the homogeneous Hopf bifurcation curve but below the steady state bifurcation curve ($P2$), a spatial homogeneous periodic orbit is observed; for the ones below the homogeneous Hopf bifurcation curve but above the steady state bifurcation curve ($P4$), a spatially non-homogeneous steady state is observed; and for the one above both bifurcation curves ($P6$), a spatially non-homogeneous periodic orbit emerges.

Example 8 *We choose* $k_2 = 1,\ k_3 = 0.5,\ \alpha = 1.5,\ L = \pi$*, there is a unique constant steady state* $(R_*, R_*) = (0.3920, 0.3920)$ *which is determined by Eq.* (3.9) *and is locally asymptotically stable for the kinetic system* (3.6) *by Proposition 4. Then, by* (3.27) *and* (3.29)*, we can compute the bifurcation point as*

$$k_{1H}^{(n)} = 5.2539(1 + (D+1)n^2),\ k_{1S}^{(n)} = \frac{D(n^4+n^2)}{0.1903n^2 - 0.2812}. \tag{3.31}$$

Similarly, by plotting (3.31) in $D - k_1$ plane, we obtain the bifurcation diagram in Fig. 3.13. Note that here a homogeneous Hopf bifurcation line is absent as $k_2 < k_2^*$.

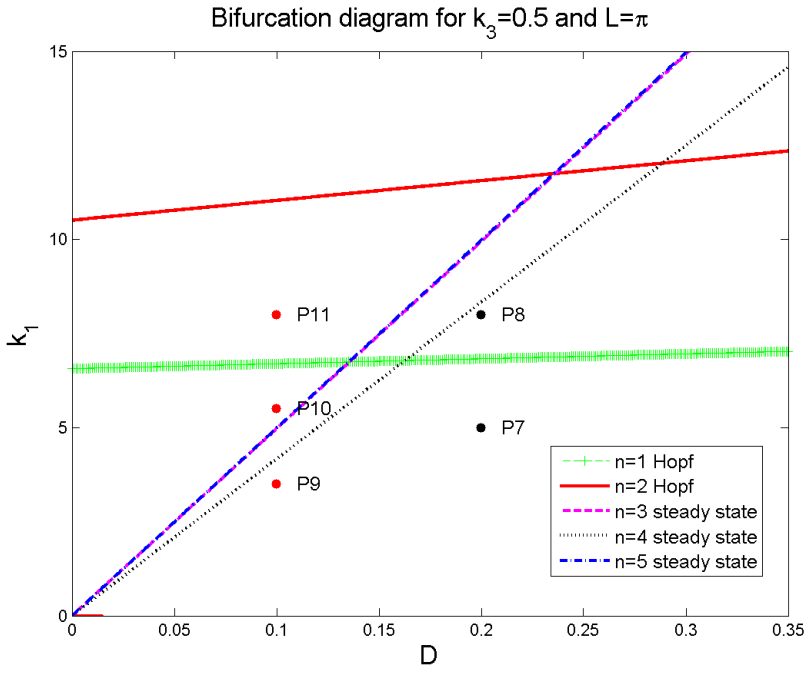

Figure 3.13: Steady state and Hopf bifurcation diagram for Eq. (3.5) on $D - k_1$ plane with $k_2 = 1,\ k_3 = 0.5,\ \alpha = 1.5,\ L = \pi$. The chosen points for the numerical simulations are: $P7 = (0.2, 5),\ P8 = (0.2, 8),\ P9 = (0.1, 3.5),\ P10 = (0.1, 6),\ P11 = (0.1, 8)$.

According to Lemma 6, we know that there is no homogeneous Hopf bifurcation in this case. When $D = 0.2$, Fig. 3.14 shows that the constant steady state is stable below the non-homogeneous Hopf bifurcation line ($P7$, upper row of Fig. 3.14), and a stable spatially non-homogeneous time-periodic pattern emerges when k_1 crosses the first non-homogeneous Hopf bifurcation line ($P8$, lower row of Fig. 3.14). On the other hand when $D = 0.1$, with the increase of k_1, the first bifurcation line is the steady state bifurcation with mode $n = 4$, so we observe the spatially non-homogeneous steady state at $P10$ (see the middle row of Fig. 3.15). Then the lower row of Fig. 3.15 demonstrates that a spatiotemporal oscillatory pattern is generated after k_1 traverses the spatially non-homogeneous Hopf bifurcation line.

In this example, a spatially homogeneous Hopf bifurcation does not occur, and

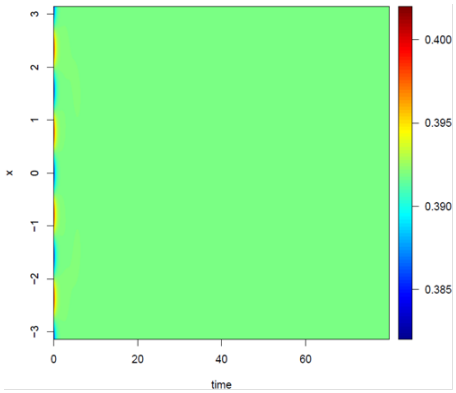

(a) $R(x,t)$ with $P7(0.2,5)$

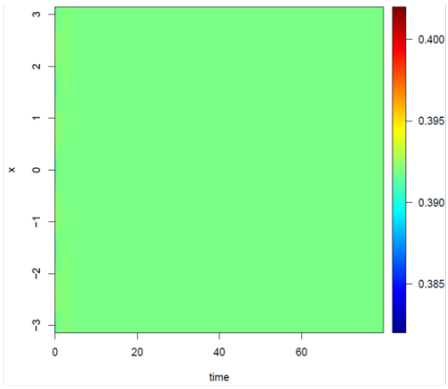

(b) $C(x,t)$ with $P7(0.2,5)$

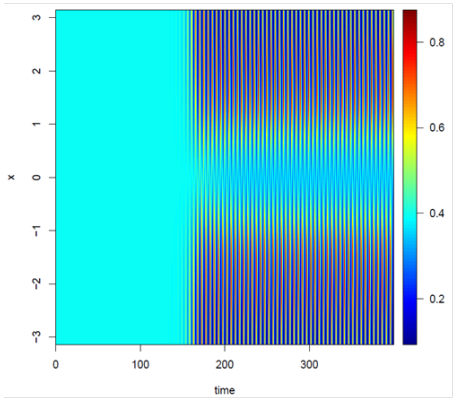

(a) $R(x,t)$ with $P8(0.2,8)$

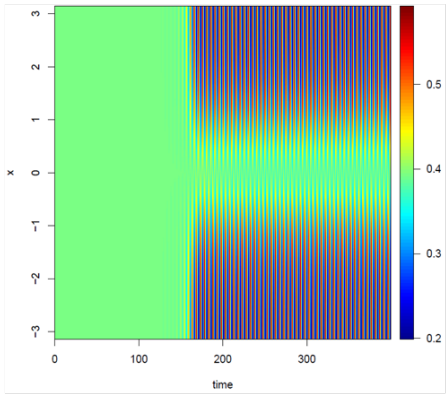

(b) $C(x,t)$ with $P8(0.2,8)$

Figure 3.14: The dynamics of Eq. (3.5) when $D = 0.2,\ k_2 = 1,\ k_3 = 0.5,\ L = \pi$.

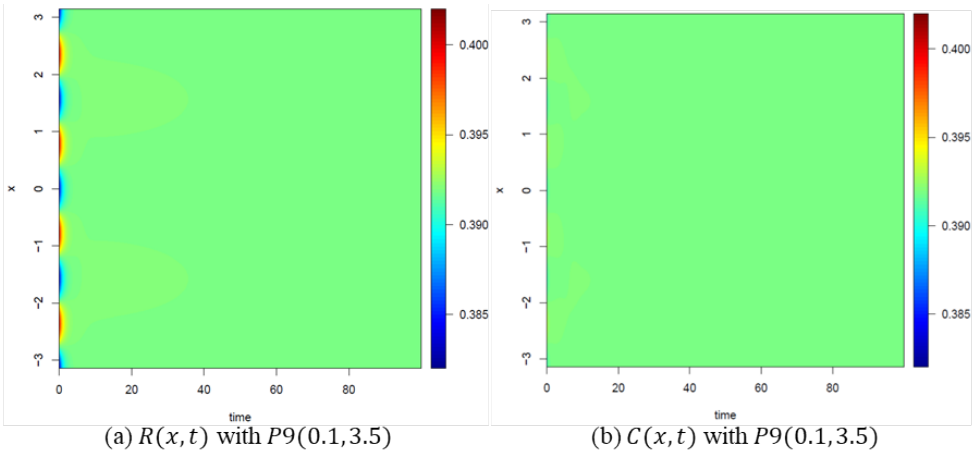

(a) $R(x,t)$ with $P9(0.1,3.5)$ (b) $C(x,t)$ with $P9(0.1,3.5)$

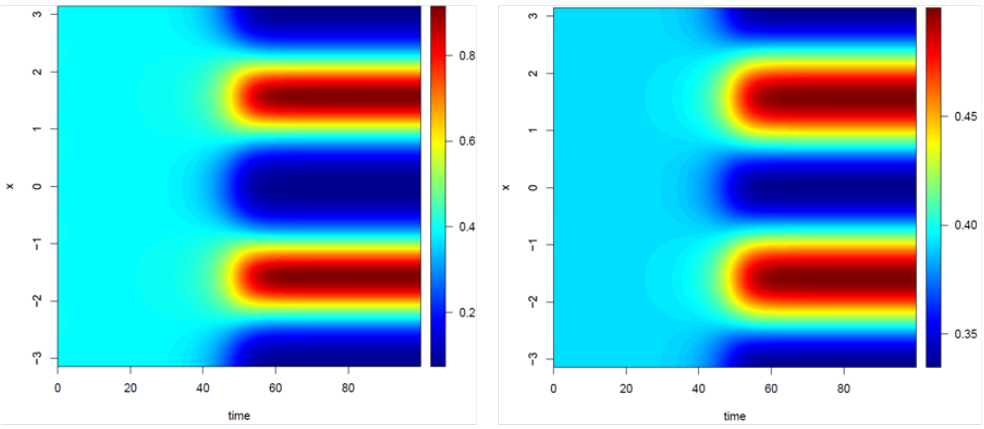

(c) $R(x,t)$ with $P10(0.1,6)$ (d) $C(x,t)$ with $P10(0.1,6)$

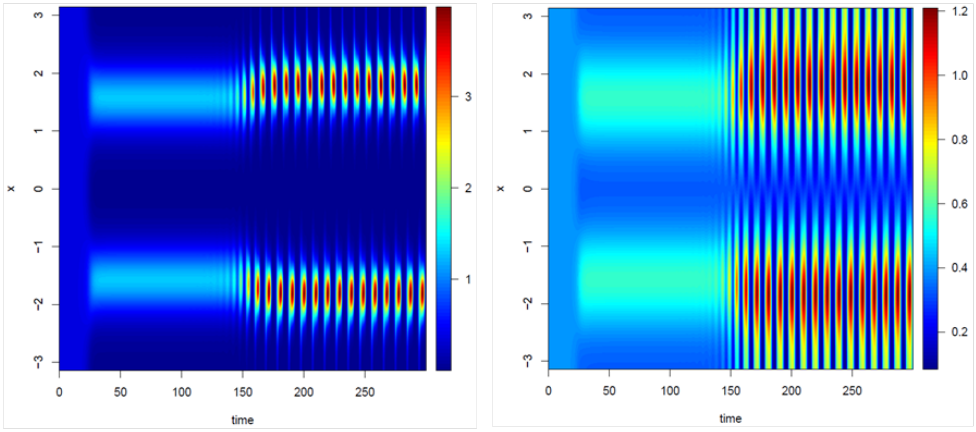

(e) $R(x,t)$ with $P11(0.1,8)$ (f) $C(x,t)$ with $P11(0.1,8)$

Figure 3.15: The dynamics of Eq. (3.5) when $D = 0.1,\ k_2 = 1,\ k_3 = 0.5,\ L = \pi$.

the spatially non-homogeneous time-periodic orbits can bifurcate directly from a constant steady state (Fig. 3.14), or through a steady state bifurcation first then a Hopf bifurcation (see Fig. 3.15), which is different from the ones in Example 7.

Part II

Statistical Analysis of Pollen Tube Tip Growth Model

Chapter 4

Literature Review: Parameter Estimation of Differential Equation

Reaction diffusion equation, a special type of Differential Equation (DE), has been widely used in modeling dynamic processes from molecular level to species level in biology. At molecular level, enzyme inhibition and cooperatively reaction is typically studied with nonlinear reaction-diffusion equation [41]. At cellular level, reaction diffusion equation is used to model formation of clusters of cells, which gives rise to disease, such as growth of small avascular solid tumors [35]. At species level, as basic structure of food chains and ecological system, dynamic of prey-predator is also formulated with reaction diffusion equation incorporated with time delay and spatial components [28].

However, studies on parameter estimation of DE models are limited, especially for PDE. Most parameter estimation procedures of DE models can be classified into three types: (1) gradient matching procedure [4, 18, 27]; (2) generalized profiling estimation

[39, 27]; (3) Bayesian estimation [39]. Gradient matching procedure can be considered as a two-step method, which in the first step obtains nonparametric estimate of the function and its derivative and then in the second step estimates parameters by least square or weighted least square methods. For generalized profiling estimation, the unknown dynamic is still estimated by nonparametric function, such as linear combination of basis function. However, there are two main differences between generalized profiling estimation and gradient matching procedure. One is that a different smoothing penalty is used in nonparametric estimation of the function. The other is that in generalized profiling estimation the unknown dynamic and PDE parameters are estimated simultaneously. For Bayesian estimation of dynamic function, Xun [39] outlined a Monte Carlo Markov Chain (MCMC) based Bayesian estimation procedure with Bayesian P-spline. In this chapter, we will briefly review all three types of methods.

4.1 Gradient matching procedure

Liang [18] and Brunel [4] both proposed gradient matching related parameter estimation procedure. Both methods are developed based on ODE as

$$\begin{cases} \dot{F} = \mathcal{F}(F(t), \boldsymbol{\theta}) \\ F(0) = F_0 \end{cases} \tag{4.1}$$

In Liang's work [18], data points are observed at time grids $\{t_i\}_{i=1}^n$, where t_i are i.i.d uniformly distributed on $[0, 1]$.

$$Y_i = F(t_i) + \epsilon_i \quad i = 1, 2, \cdots, n \tag{4.2}$$

where ϵ_i, $i = 1, 2, \cdots, n$ are independently distributed with mean zero and finite variance $\sigma^2(t_i)$. Liang and Wu [18] proposed a 2-step procedure consisting of (1) local polynomial regression to smooth the function and (2) parameter estimation by least square method. Based on local polynomial regression [8], with symmetric kernel function as $K_h(\cdot) = K(\cdot/h)/h$, the function and its derivative can be estimated by

$$\hat{F}(t) = \boldsymbol{\zeta}_1^T \left(\boldsymbol{T}_{1,t}^T \boldsymbol{W}_t \boldsymbol{T}_{1,t}\right)^{-1} \boldsymbol{T}_{1,t}^T \boldsymbol{W}_t \boldsymbol{Y}$$

$$\hat{\dot{F}}(t) = \boldsymbol{\zeta}_2^T \left(\boldsymbol{T}_{2,t}^T \boldsymbol{W}_t \boldsymbol{T}_{2,t}\right)^{-1} \boldsymbol{T}_{2,t}^T \boldsymbol{W}_t \boldsymbol{Y}$$

where $\boldsymbol{\zeta}_1 = (1 \quad 0)$, $\boldsymbol{\zeta}_2 = (0 \quad 1 \quad 0)$, $\boldsymbol{W}_t = \text{diag}\{K_h(t_1 - t), \cdots, K_h(t_n - t)\}$, and

$$\boldsymbol{T}_{1,t} = \begin{vmatrix} 1 & t_1 - t \\ \vdots & \vdots \\ 1 & t_n - t \end{vmatrix} \qquad \boldsymbol{T}_{2,t} = \begin{vmatrix} 1 & t_1 - t & (t_1 - t)^2 \\ \vdots & \vdots & \vdots \\ 1 & t_n - t & (t_n - t)^2 \end{vmatrix}$$

With nonparametric estimators of function and its first order derivative, $\hat{F}(t)$ and $\hat{\dot{F}}(t)$, the parameter estimation can be obtained by

$$\hat{\boldsymbol{\theta}} = \underset{\boldsymbol{\theta}}{\text{argmin}} \sum_{i=1}^{n} \left| \hat{\dot{F}}(t_i) - \mathcal{F}(\dot{F}(t_i), \boldsymbol{\theta}) \right|^2$$

Moreover, Liang and Wu [18] provided asymptotic theory for their method under the following assumptions:

1. The third derivative of $F(t)$ is continuous on $[0, 1]$.

2. The kernel function $K(\cdot)$ is symmertric about zero and is supported on $[-1, 1]$.

3. The bandwidth $h = h_n = n^{-2/7} a_n$ is a sequence satisfying $h \to 0$ as $n \to \infty$, where a_n is a sequence tending to 0 slower than $\log^{-1} n$.

4. $\mathcal{F}(F, \boldsymbol{\theta})$ is a continuous function of $\boldsymbol{\theta}$.

5. Parameter space is closed, bounded compact set.

6. Distance between two parameters $d_n(\boldsymbol{\theta}_1, \boldsymbol{\theta}_2) = \sum_{i=1}^{n} |\mathcal{F}(F(t_i), \boldsymbol{\theta}_1) - \mathcal{F}(F(t_i), \boldsymbol{\theta}_2)|^2 \to d(\boldsymbol{\theta}_1, \boldsymbol{\theta}_2) = 0$ if and only if $\boldsymbol{\theta}_1 = \boldsymbol{\theta}_2$.

7. The first and second partial derivatives of $\mathcal{F}(F, \boldsymbol{\theta})$ exist and are continuous for all $\boldsymbol{\theta}$ and F, and for some $0 < \iota < 1$ and constant M_1,

$$\left| \frac{\partial \mathcal{F}(F_1, \boldsymbol{\theta})}{\partial \boldsymbol{\theta}} - \frac{\partial \mathcal{F}(F_2, \boldsymbol{\theta})}{\partial \boldsymbol{\theta}} \right| \leq M_1 |F_1 - F_2|^{\iota}.$$

8. The first partial derivative $\dfrac{\partial \mathcal{F}(F, \boldsymbol{\theta})}{\partial F}$ is continuous, for some constant $M_{\boldsymbol{\theta}}$,

$$\sup_F \left| \frac{\partial \mathcal{F}(F, \boldsymbol{\theta})}{\partial F} \right| \leq M_{\boldsymbol{\theta}}.$$

With all of the above assumptions, $\hat{\boldsymbol{\theta}}$ is proved to be consistent, and $nh^{3/2}(\hat{\boldsymbol{\theta}} - \boldsymbol{\theta})$ is asymptotically normally distributed with mean zero and covariance matrix as

$$\boldsymbol{\Sigma}_{\boldsymbol{\theta}} = \sigma^2 \mu_2^{-2}(K) \mu_2(K^2) \left[\mathbb{E} \left\{ \frac{\partial \mathcal{F}(F, \boldsymbol{\theta})}{\partial \boldsymbol{\theta}} \right\}^{\otimes 2} \right]^{-1}$$

where $\mu_2(K) = \int_{-1}^{1} z^2 K(z) dz$.

In Brunel's work [4], he used B-spline regression instead of local polynomial regression in smoothing step and weighted least square method in estimation step. Although both methods are developed for ODE, Bar, Hegger and Kantz [2] applied similar method to PDE using multivariate polynomial approximation.

4.2 Generalized Profiling Estimation

Xun [39] and Ramsay [27] introduced similar generalized profiling estimation methods based on a PDE model

$$\mathcal{F}(\boldsymbol{x}, F, \frac{\partial F}{x_1}, \cdots, \frac{\partial F}{x_p}, \frac{\partial^2 F}{\partial x_1 \partial x_1}, \cdots, \frac{\partial^2 F}{\partial x_1 \partial x_p}, \cdots, \boldsymbol{\theta}) = 0 \quad \boldsymbol{x} \in \Omega \tag{4.3}$$

Data $\{Y_i\}_{i=1}^n$ is observed over a meshgrid with measurement error as

$$Y_i = F(\boldsymbol{x}_i) + \epsilon_i \quad i = 1, \cdots, n$$

where ϵ_i, $i = 1, \cdots, n$, follow i.i.d Gaussian distribution with mean zero and variance σ_e^2.

Similar as gradient matching procedure, the unknown dynamic is also represented with nonparametric function, such as linear combination of basis functions:

$$F(\boldsymbol{x}) = \sum_{m=1}^{N} \phi_m(\boldsymbol{x})\beta_m = \boldsymbol{\phi}^T(\boldsymbol{x})\boldsymbol{\beta} \tag{4.4}$$

where $\{\phi_m(\boldsymbol{x})\}_{m=1}^N$ are basis functions. The PDE model (4.3) can be rewritten in terms of basis functions as

$$\mathcal{F}(\boldsymbol{x}, \boldsymbol{\phi}^T\boldsymbol{\beta}, \frac{\partial \boldsymbol{\phi}}{x_1}^T \boldsymbol{\beta}, \cdots, \frac{\partial \boldsymbol{\phi}}{x_p}^T \boldsymbol{\beta}, \frac{\partial^2 \boldsymbol{\phi}^T}{\partial x_1 \partial x_1}\boldsymbol{\beta}, \cdots, \frac{\partial^2 \boldsymbol{\phi}^T}{\partial x_1 \partial x_p}\boldsymbol{\beta}, \cdots, \boldsymbol{\theta}) = 0 \tag{4.5}$$

However, one of the differences between gradient matching procedure and generalized profiling estimation is that the latter introduces a new penalty function in smoothing step. Here the smoothing coefficient $\boldsymbol{\beta}$ is estimated by penalized least square with

$$S_{inner}(\boldsymbol{\beta}|\boldsymbol{\theta}) = \sum_{i=1}^{n}(Y_i - \boldsymbol{\phi}^T(\boldsymbol{x}_i)\boldsymbol{\beta})^2 + \rho \int_\Omega \mathcal{F}(\boldsymbol{\phi}^T(\boldsymbol{x})\boldsymbol{\beta}, \boldsymbol{\theta})^2 d\boldsymbol{x}$$

and PDE parameter estimation is obtained by minimizing

$$S_{outer}(\boldsymbol{\theta}) = \sum_{i=1}^{n} \left[Y_i - \boldsymbol{\phi}^T(\boldsymbol{x}_i)\hat{\boldsymbol{\beta}}(\boldsymbol{\theta})\right]^2$$

Therefore, algorithm for generalized profiling method can be summarized as bellow: (1) setting up initial value as $\boldsymbol{\theta} = \boldsymbol{\theta}^{(0)}$; (2) obtaining $\boldsymbol{\beta}^{(itr+1)}(\boldsymbol{\theta}^{(itr)})$ by minimizing $S_{inner}(\boldsymbol{\beta}|\boldsymbol{\theta}^{(itr)})$; (3) updating $\boldsymbol{\theta} = \boldsymbol{\theta}^{(itr+1)}$ by minimizing $S_{outer}(\boldsymbol{\theta})$; (4) repeating step (2) and (3) for sufficient time until $\boldsymbol{\theta}^{(itr)}$ converges.

4.3 Bayesian Estimation

Xun [39] also proposed a Bayesian estimation procedure for model (4.3) with application of Bayesian P-Spline and the idea of incorporating PDE model (4.3) as prior information. Bayesian P-Spline is applied in smoothing step with similar nonparametric representation of the unknown dynamic $Y_i = \boldsymbol{\phi}^T(\boldsymbol{x}_i)\boldsymbol{\beta} + \epsilon_i$, where ϵ_i, $i = 1, \cdots, n$, follow i.i.d Gaussian distribution with mean zero and variance σ_e^2. Here we use two-dimensional case as an example. Considering the interaction of one-dimensional coefficients as well as each dimension, we applied difference penalty. Let $\boldsymbol{\Phi}_1$ and $\boldsymbol{\Phi}_2$ be basis function matrices of each dimension, and $\dot{\boldsymbol{\Phi}}_1$, $\dot{\boldsymbol{\Phi}}_2$ be corresponded first order derivative matrices. In this case, prior is suggested by Berry , Carroll and Ruppert [3] as

$$[\boldsymbol{\beta}|\gamma_1, \gamma_2] \propto (\gamma_1\gamma_2)^{N/2}\exp\{-\boldsymbol{\beta}^T(\gamma_1\boldsymbol{H_1} + \gamma_2\boldsymbol{H_2} + \gamma_1\gamma_2\boldsymbol{H_3})\boldsymbol{\beta}/2\}$$

where N is the number of basis function, $\boldsymbol{H_1} = \boldsymbol{\Phi}_1^T\boldsymbol{\Phi}_1 \otimes \dot{\boldsymbol{\Phi}}_2^T\dot{\boldsymbol{\Phi}}_2$, $\boldsymbol{H_2} = \dot{\boldsymbol{\Phi}}_1^T\dot{\boldsymbol{\Phi}}_1 \otimes \boldsymbol{\Phi}_2^T\boldsymbol{\Phi}_2$, and $\boldsymbol{H_3} = \dot{\boldsymbol{\Phi}}_1^T\dot{\boldsymbol{\Phi}}_1 \otimes \dot{\boldsymbol{\Phi}}_2^T\dot{\boldsymbol{\Phi}}_2$. As hyper-parameter, prior of γ_1 and γ_2 is suggested to be Gamma(a_1,b_1) and Gamma(a_2,b_2), respectively. Meanwhile, model (4.3) also incorporates prior information as

$$\mathcal{F}(\boldsymbol{\phi}^T(\boldsymbol{x}_i)\boldsymbol{\beta}, \boldsymbol{\theta}) = \psi(\boldsymbol{x}_i) \quad i = 1, \cdots, n$$

where $\psi(\boldsymbol{x}_i)$, $i = 1, \cdots, n$ is assumed to be i.i.d with a prior distribution $N(0, \gamma_0^{-1})$, where γ_0 is precision parameter and large enough so that the approximation error in basis function representation is small. The prior of γ_0 is suggested to be Gamma(a_0,b_0) by Xun [39]. The hierarchical Bayesian model can be summarized as follows:

Stage 1 Observation data:

$$Y_i = \boldsymbol{\phi}^T(\boldsymbol{x}_i)\boldsymbol{\beta} + \epsilon_i, \quad \epsilon_i \sim N(0, \sigma_e^2) \quad i = 1, \cdots, n$$

Stage 2 Bayesian P-Splines:

$$[\boldsymbol{\beta}|\boldsymbol{\theta}, \gamma_0, \gamma_1, \gamma_2] \propto (\gamma_0\gamma_1\gamma_2)^{N/2}\exp\{-\gamma_0\boldsymbol{\psi}^T(\boldsymbol{\beta}, \boldsymbol{\theta})\boldsymbol{\psi}(\boldsymbol{\beta}, \boldsymbol{\theta})/2 - \boldsymbol{\beta}^T(\gamma_1\boldsymbol{H_1} + \gamma_2\boldsymbol{H_2} + \gamma_1\gamma_2\boldsymbol{H_3})\boldsymbol{\beta}/2\}$$

Stage 3 Prior of PDE parameters:

$$\boldsymbol{\theta} \propto MVN(\mathbf{0}, \sigma_\theta^2\boldsymbol{I})$$

$$\sigma_e^2 \sim \text{Inverse Gamma}(a, b)$$

Stage 4 Prior of hyper parameters in Bayesian P-Splines:

$$\gamma_j \sim \text{Gamma}(a_j, b_j), \quad j = 0, 1, 2$$

In order to obtain Bayesian estimates, MCMC is implemented by using the Gibbs sampling approach to get a sequence of realizations of σ_e^2, γ_0, γ_1, γ_2 from posterior distribution, and Metropolis-Hastings method to simulate realizations of $\boldsymbol{\beta}$ and $\boldsymbol{\theta}$. Therefore, with all prior information, the Bayesian method is implemented as discussed below.

Let the procedure starts with initialized values $\sigma_e^{2(0)}$, $\gamma_0^{(0)}$, $\gamma_1^{(0)}$, $\gamma_2^{(0)}$, $\boldsymbol{\beta}^{(0)}$ and $\boldsymbol{\theta}^{(0)}$. Suppose current value is $\sigma_e^{2(itr)}$, $\gamma_0^{(itr)}$, $\gamma_1^{(itr)}$, $\gamma_2^{(itr)}$, $\boldsymbol{\beta}^{(itr)}$ and $\boldsymbol{\theta}^{(itr)}$. The updating procedure is as follows:

step 1 Using Gibbs sampling to simulate a realization of each of σ_e^2, γ_0, γ_1, γ_2 given other parameters, $\boldsymbol{\beta}^{(itr)}$, $\boldsymbol{\theta}^{(itr)}$ and $\boldsymbol{Y}$

$$\sigma_e^{2(itr+1)}|\gamma_0^{(itr)},\gamma_1^{(itr)},\gamma_2^{(itr)},\boldsymbol{\beta}^{(itr)},\boldsymbol{\theta}^{(itr)},\boldsymbol{Y}$$

$$\sim \text{Inverse Gamma}\left(a+n/2, b+(\boldsymbol{Y}-\boldsymbol{\Phi}\boldsymbol{\beta}^{(itr)})^T(\boldsymbol{Y}-\boldsymbol{\Phi}\boldsymbol{\beta}^{(itr)})/2\right)$$

$$\gamma_0^{(itr+1)}|\sigma_e^{2(itr+1)},\gamma_1^{(itr)},\gamma_2^{(itr)},\boldsymbol{\beta}^{(itr)},\boldsymbol{\theta}^{(itr)},\boldsymbol{Y}$$

$$\sim \text{Gamma}\left(a_0+N/2, b_0+\boldsymbol{\psi}^T(\boldsymbol{\beta}^{(itr)},\boldsymbol{\theta}^{(itr)})\boldsymbol{\psi}(\boldsymbol{\beta}^{(itr)},\boldsymbol{\theta}^{(itr)})/2\right)$$

$$\gamma_1^{(itr+1)}|\sigma_e^{2(itr+1)},\gamma_0^{(itr+1)},\gamma_2^{(itr)},\boldsymbol{\beta}^{(itr)},\boldsymbol{\theta}^{(itr)},\boldsymbol{Y}$$

$$\sim \text{Gamma}\left(a_1+N/2, b_1+\boldsymbol{\beta}^{(itr)T}(\boldsymbol{H_1}+\gamma_2^{(itr)}\boldsymbol{H_3})\boldsymbol{\beta}^{(itr)}/2\right)$$

$$\gamma_2^{(itr+1)}|\sigma_e^{2(itr+1)},\gamma_0^{(itr+1)},\gamma_1^{(itr+1)},\boldsymbol{\beta}^{(itr)},\boldsymbol{\theta}^{(itr)},\boldsymbol{Y}$$

$$\sim \text{Gamma}\left(a_2+N/2, b_2+\boldsymbol{\beta}^{(itr)T}(\boldsymbol{H_2}+\gamma_1^{(itr+1)}\boldsymbol{H_3})\boldsymbol{\beta}^{(itr)}/2\right)$$

step 2 Using Metropolis-Hastings method to simulate a realization of $\boldsymbol{\beta}^{(itr+1)}$, $\boldsymbol{\theta}^{(itr+1)}$ with conditional distribution as

$$
\begin{aligned}
&\boldsymbol{\beta}|\sigma_e^{2(itr+1)}, \gamma_0^{(itr+1)}, \gamma_1^{(itr+1)}, \gamma_2^{(itr+1)}, \boldsymbol{\theta}^{(itr)}, \boldsymbol{Y} \\
&\quad \propto \exp\Big\{-\boldsymbol{\beta}^T(\sigma_e^{2(itr+1)}\boldsymbol{\Phi}^T\boldsymbol{\Phi} + \gamma_1^{(itr+1)}\boldsymbol{H_1} + \gamma_2^{(itr+1)}\boldsymbol{H_2} + \gamma_1^{(itr+1)}\gamma_2^{(itr+1)}\boldsymbol{H_3})\boldsymbol{\beta}/2 \\
&\quad -\sigma_e^{-2(itr+1)}\boldsymbol{\beta}^T\boldsymbol{\Phi}^T\boldsymbol{Y} - \gamma_0^{(itr+1)}\boldsymbol{\psi}^T(\boldsymbol{\beta}, \boldsymbol{\theta}^{(itr)})\boldsymbol{\psi}(\boldsymbol{\beta}, \boldsymbol{\theta}^{(itr)})/2\Big\} \\
&\boldsymbol{\theta}|\sigma_e^{2(itr+1)}, \gamma_0^{(itr+1)}, \gamma_1^{(itr+1)}, \gamma_2^{(itr+1)}, \boldsymbol{\beta}^{(itr+1)}, \boldsymbol{Y} \\
&\quad \propto \exp\Big\{-\boldsymbol{\theta}^T\boldsymbol{\theta}/(2\sigma_e^{2(itr+1)}) - \gamma_0^{(itr+1)}\boldsymbol{\psi}^T(\boldsymbol{\beta}, \boldsymbol{\theta}^{(itr)})\boldsymbol{\psi}(\boldsymbol{\beta}, \boldsymbol{\theta}^{(itr)})/2\Big\}
\end{aligned}
$$

We repeat the above 2-step updating rule to get a sequence of realizations of $\{\sigma_e^2, \gamma_0, \gamma_1, \gamma_2, \boldsymbol{\beta}, \boldsymbol{\theta}\}$. Moreover, it is suggested that initial burn-in period should be ignored because the initial realizations are most likely not coming from the target distribution, and that one should save every k-th realizations to reduce dependence.

Chapter 5

Parameter Estimation Procedure of Linear Reaction Diffusion Equation

In Chapter 4, we reviewed the current state-of-the-art parameter estimation procedures for DE models, which can be categorized as gradient matching procedure [4, 18, 27], generalized profiling method [39, 27] and Bayesian method [39, 27]. However, all of these methods have some limitations. For example, the computation of variation of parameter estimators can be hard. Sometimes bootstrap method is introduced to evaluate standard error of estimators. Moreover, most of these methods require nonparametric estimation of the second order (or even higher order) derivative with respect to spatial axes, which would be difficult in high dimensional cases.

In this chapter and the following chapter, we propose a parameter estimation

procedure for the reaction diffusion equation written as below:

$$\frac{\partial F(\boldsymbol{x},t)}{\partial t} = \mathcal{F}(F(\boldsymbol{x},t),\boldsymbol{\theta}) + D\Delta F \tag{5.1}$$

where $F(\boldsymbol{x},t)$ is unknown spatial-temporal dynamics function, $\mathcal{F}(\cdot)$ is local reaction function depending on $F(\boldsymbol{x},t)$ and parameter $\boldsymbol{\theta}$, D is diffusion coefficient, and Δ is Laplacian operator. Our proposed method is based on gradient matching procedure. Instead of using naive version of gradient matching procedure with nonparametric estimation of the second order derivative with respect to $\boldsymbol{x}$, we identify a system of ODEs on inner product of solution and eigen-function of Laplacian operator, which also depends on parameters. Moreover, in linear reaction diffusion equation case, we can obtain a closed-form expression for parameters.

Specifically, we consider a general linear reaction diffusion model defined on the bounded space Ω with boundary denoted as $\partial\Omega$.

$$\begin{cases} F_t = \theta_1 G(\boldsymbol{x},t) + \theta_2 F(\boldsymbol{x},t) + D\Delta F, \quad \text{for} \quad (\boldsymbol{x},t) \in \Omega \times [0,T] \\ \alpha_1 F(\boldsymbol{x},t) + \alpha_2 \dfrac{\partial F}{\partial \boldsymbol{n}} = 0, \quad \text{for} \quad (\boldsymbol{x},t) \in \partial\Omega \times [0,T] \\ F(\boldsymbol{x},0) = f_0(\boldsymbol{x}) \end{cases} \tag{5.2}$$

where θ_1, θ_2 and D are unknown parameters and $f_0(\boldsymbol{x})$ is the initial condition. In particular, we will focus on the domain $\Omega = [0,1]^p$. There exist a variety of boundary conditions which have strong influence on the solutions (existence, or qualitative properties). In this case, we only consider Dirichlet condition, where $\alpha_2 = 0$, and Neumann's condition, where $\alpha_1 = 0$.

In model (5.2), $G(\boldsymbol{x},t)$ serves as a source function and $F(\boldsymbol{x},t)$ as unknown dynamic function defined on domain Ω. Hence, the first, second and the third term in model (5.2)

can be considered as source, linear reaction and diffusion term, respectively. In this chapter, we will first review some mathematical background. Then, we will describe the proposed procedure with technique details. In the end, we will provide consistency and asymptotic normality of the proposed estimator, followed by simulation studies.

5.1 Mathematical background

We are interested in the parameter estimation of general linear parabolic PDE defined on the set $\Omega \times [0, T]$, where Ω is a bounded set in $\mathbb{R}^p$. The existence and uniqueness of solutions to this kind of PDEs can be assessed in general situations. In this case, the existence of the solutions for linear hyperbolic PDE is based on a suitable series expansion provided by the eigenfunctions of the Laplacian.

Model (5.2) is a parabolic PDE, closely related to the Heat Equation. Indeed, if we consider the standard transformation $\check{F} = \exp(-\theta_2 t)F$, the function $\check{F}$ is the solution of the Heat equation:

$$\check{F}_t = \theta_1 \check{G} + D\Delta\check{F} \tag{5.3}$$

with a source $(\boldsymbol{x}, t) \mapsto \check{G}(\boldsymbol{x}, t) = \exp(\theta_2 t)G(\boldsymbol{x}, t)$, and the same boundary and initial conditions. It suffices to have mild regularity conditions on the initial condition $f_0(\boldsymbol{x})$ and the source function $G(\boldsymbol{x}, t)$. In particular, a convenient derivation of the solution $F(\boldsymbol{x}, t)$ to (5.2) is provided by the use of a Hilbert basis of $\mathbb{L}^2(\Omega)$ obtained for the Laplacian on Ω with boundary conditions. Indeed, an almost closed-form expression is obtained by the

eigenfunctions $\{\varphi_n\}_{n=0}^{\infty}$ satisfying:

$$\begin{cases} -\Delta\varphi_n = \lambda_n\varphi_n, \quad \text{for} \quad \boldsymbol{x} \in \Omega \\ \alpha_1\varphi_n(\boldsymbol{x}) + \alpha_2\dfrac{\partial\varphi_n(\boldsymbol{x})}{\partial \boldsymbol{n}} = 0, \quad \text{for} \quad \boldsymbol{x} \in \partial\Omega \end{cases} \tag{5.4}$$

where $\{\lambda_n\}_{n=0}^{\infty}$ is the sequence of increasing eigenvalues. Obviously, the eigenfunctions depend on the boundary conditions. Here we only consider Dirichlet or Neumann's condition, hence the solution space is either the Sobolev space $\mathbb{H}_0^1$ or $\mathbb{H}^1$.

Example 9 *Examples of eigenfunctions* $\{\varphi_n\}_{n=0}^{\infty}$*:*

1. *For* $\Omega = [0, 1]$*:*

   - *Neumann's condition* ($\alpha_1 = 0$)*,*

   $$\varphi_n(x) = \begin{cases} 1 & n = 0 \\ \sqrt{2}cos(n\pi x) & n = 1, 2, \cdots \end{cases} \tag{5.5}$$

   with $\lambda_n = (n\pi)^2$*;*

   - *Dirichlet's condition* ($\alpha_2 = 0$)*,*

   $$\varphi_n(x) = \begin{cases} 0 & n = 0 \\ \sqrt{2}\sin(n\pi x) & n = 1, 2, \cdots \end{cases} \tag{5.6}$$

   with $\lambda_n = (n\pi)^2$*.*

2. *For hypercube* $\Omega = [0, 1]^p$ *with eigenfunctions for the Laplacian with Dirichlet conditions,*

   $$\varphi_n(\boldsymbol{x}) = 2^{p/2}\prod_{i=1}^{p}\sin(n\pi x_i)$$

while for Neumann's condition

$$\varphi_n(\boldsymbol{x}) = 2^{p/2} \prod_{i=1}^{p} \cos(n\pi x_i)$$

We assume that the source function $(\boldsymbol{x}, t) \mapsto G(\boldsymbol{x}, t)$ is a function in $\mathbb{L}^2\big(\Omega \times [0, T]\big)$ and that the functions

$$t \mapsto \langle G, \varphi_n \rangle \stackrel{\Delta}{=} G_n(t)$$

are differentiable for all $n \geq 0$. From equation (5.2) and (5.4) and integration by parts exploiting the boundary conditions, we obtain that the solution $(\boldsymbol{x}, t) \mapsto F(\boldsymbol{x}, t)$ can be decomposed as

$$F(\boldsymbol{x}, t) = \sum_{n=0}^{\infty} F_n(t) \varphi_n(\boldsymbol{x}),$$

and we have for all $n \geq 0$, for all t in [0,T]:

$$\begin{cases} \frac{d}{dt} F_n(t) + (\lambda_n D - \theta_2) F_n(t) = \theta_1 G_n(t) \\ \\ F_n(0) = F_{0,n} \end{cases} \tag{5.7}$$

The initial conditions $F_{0,n}$ are derived from the series expansion of the initial condition $F_0(\boldsymbol{x}) = \sum_{n=0}^{\infty} F_{0,n} \varphi_n(\boldsymbol{x})$. We have an explicit expression for the (5.7) given by

$$F_n(t) = F_{0,n} e^{(\theta_2 - \lambda_n D)t} + \theta_1 \int_0^t G_n(s) e^{(\theta_2 - \lambda_n D)(t-s)} ds \tag{5.8}$$

The existence and uniqueness of the solution shows that the $\mathbb{L}^2$ norm of $F_n(t)$ is finite for all t: $\sum_{n=0}^{\infty} |F_n(t)|^2 < \infty$ but we also have $\sum_{n=0}^{\infty} \lambda_n |F_n(t)|^2 < \infty$.

5.2 Statistical Model and Estimation Procedures

5.2.1 Statistical Model

We observe the source $G(\boldsymbol{x}, t)$ and the dynamics $F(\boldsymbol{x}, t)$ with noise on a deterministic time grid $0 < t_1 < \cdots < t_{n_t} = T$, at some locations $\boldsymbol{x}_i = 0, 1, \ldots, n_x$.

$$\begin{cases} f_{ij} = F(\boldsymbol{x}_i, t_j) + \epsilon_{ij}^{(f)} \\ g_{ij} = G(\boldsymbol{x}_i, t_j) + \epsilon_{ij}^{(g)} \end{cases} \qquad i = 0, 1, 2, \cdots, n_x \quad j = 1, 2, \cdots, n_t \tag{5.9}$$

where $\epsilon_{ij}^{(f)}, \epsilon_{ij}^{(g)}$ are observation errors satisfying $\epsilon_{ij}^{(f)} \overset{i.i.d}{\sim} N(0, \sigma_f^2)$ and $\epsilon_{ij}^{(g)} \overset{i.i.d}{\sim} N(0, \sigma_g^2)$ independently, for all $i = 0, 1, 2, \cdots, n_x$ and $j = 1, 2, \cdots, n_t$. With observations of $\{f_{ij}, g_{ij}\}_{i=0,j=1}^{n_x,n_t}$, we want to estimate the unknown reaction rate θ_1, θ_2 and diffusion rate D based on model (5.2).

5.2.2 Motivation: From PDE to ODE

Now we are going to present our parameter estimation procedure for PDE model (5.2). The proposed procedure can be considered as an extension of gradient matching approach applied to an ODE system (5.7), which is derived through spectral decomposition of the solution to PDE (5.2).

By taking the inner product on $\mathbb{L}^2(\Omega)$ with the eigenfunctions of the Laplacian, we obtain a set of ODEs defined as (5.7). For instance, in the case of Neumann's condition

on Ω we get

$$\dot{F}_0(t) = \theta_1 G_0(t) + \theta_2 F_0(t) \tag{5.10}$$

$$\dot{F}_n(t) = \theta_1 G_n(t) + (\theta_2 - D\lambda_n) F_n(t) \quad n = 1, 2, \cdots \tag{5.11}$$

For the Dirichlet conditions, the set of ODEs starts from $n = 1$. Therefore, we propose an extended gradient matching procedure for θ_1, θ_2 and D estimation. As we can see from the equation (5.11), the diffusion coefficient D can be difficult to obtain, because it is crushed by exploding with eigenvalues λ_n. This will need a special care.

5.2.3 Estimator definition and computational procedure

Inspired by the idea in section 5.2.2, we propose the following parameter estimation procedure: (1) obtaining pseudo data of $F_n(t)$ and $G_n(t)$; (2) smoothing pseudo data; (3) plugging smoothed pseudo data in equation (5.10) and (5.11) and estimating θ_1, θ_2 and D with 2-step least square estimate. Details for each step is discussed below:

Step 1: Obtaining pseudo data of $F_n(t)$ and $G_n(t)$

The Fourier coefficients $F_n(t)$ and $G_n(t)$ are obtained by Right Riemann Summation

$$\tilde{F}_n(t_j) = \Delta \boldsymbol{x} \sum_{i=1}^{n_x} f(\boldsymbol{x}_i, t_j)\varphi_n(\boldsymbol{x}_i) \qquad \tilde{G}_n(t_j) = \Delta \boldsymbol{x} \sum_{i=1}^{n_x} g(\boldsymbol{x}_i, t_j)\varphi_n(\boldsymbol{x}_i)$$

where $\Delta \boldsymbol{x} = \Delta x_1 \Delta x_2 \cdots \Delta x_p$ for $\boldsymbol{x} \in \Omega \in \mathbb{R}^p$. Notice that $\Delta \boldsymbol{x}$ is of order n_x^{-1}.

Step 2: Smoothing pseudo data $\tilde{F}_n(t)$ and $\tilde{G}_n(t)$

Let $\tilde{\boldsymbol{F}}_n = \begin{pmatrix} \tilde{F}_n(t_1) \\ \tilde{F}_n(t_2) \\ \cdots \\ \tilde{F}_n(t_{n_t}) \end{pmatrix}$, $\tilde{\boldsymbol{G}}_n = \begin{pmatrix} \tilde{G}_n(t_1) \\ \tilde{G}_n(t_2) \\ \cdots \\ \tilde{G}_n(t_{n_t}) \end{pmatrix}$. $\tilde{\boldsymbol{F}}_n$ and $\tilde{\boldsymbol{G}}_n$ can be smoothed by any smoothing technique, such as local polynomial method, projection estimator, kernel estimator and so on. Here, we use projection technique with orthogonal basis function set $\{\phi_m(t)\}_{m=0}^{\infty}$. Note that basis function set $\{\phi_m(t)\}_{m=0}^{\infty}$ can be chosen from multiple smoothing techniques, such that B-splines. As for periodic function, $\{\phi_m(t)\}_{m=0}^{\infty}$ can also be chosen as Fourier series. Suppose, we choose the number of basis function is $N_{T,est}$. Let

$$\boldsymbol{\Phi} = \begin{pmatrix} \boldsymbol{\phi}_1 & \boldsymbol{\phi}_2 & \cdots & \boldsymbol{\phi}_{N_{T,est}} \end{pmatrix} = \begin{pmatrix} \phi_1(t_1) & \phi_2(t_1) & \cdots & \phi_{N_{T,est}}(t_1) \\ \phi_1(t_2) & \phi_2(t_2) & \cdots & \phi_{N_{T,est}}(t_2) \\ \vdots & \vdots & \cdots & \vdots \\ \phi_1(t_{n_t}) & \phi_2(t_{n_t}) & \cdots & \phi_{N_{T,est}}(t_{n_t}) \end{pmatrix}$$

$$\dot{\boldsymbol{\Phi}} = \begin{pmatrix} \dot{\boldsymbol{\phi}}_1 & \dot{\boldsymbol{\phi}}_2 & \cdots & \dot{\boldsymbol{\phi}}_{N_{T,est}} \end{pmatrix} = \begin{pmatrix} \dot{\phi}_1(t_1) & \dot{\phi}_2(t_1) & \cdots & \dot{\phi}_{N_{T,est}}(t_1) \\ \dot{\phi}_1(t_2) & \dot{\phi}_2(t_2) & \cdots & \dot{\phi}_{N_{T,est}}(t_2) \\ \vdots & \vdots & \cdots & \vdots \\ \dot{\phi}_1(t_{n_t}) & \dot{\phi}_2(t_{n_t}) & \cdots & \dot{\phi}_{N_{T,est}}(t_{n_t}) \end{pmatrix}$$

Let $\boldsymbol{\phi}(t) = \begin{bmatrix} \phi_1(t) & \phi_2(t) & \cdots & \phi_{N_{T,est}}(t) \end{bmatrix}$. In this case, $\tilde{F}_n(t)$, $\tilde{G}_n(t)$ can be smoothed by

$$\hat{F}_n(t) = \boldsymbol{\phi}(t)(\boldsymbol{\Phi}^T\boldsymbol{\Phi})^{-1}\boldsymbol{\Phi}^T\tilde{\boldsymbol{F}}_{\boldsymbol{n}} \qquad \hat{G}_n(t) = \boldsymbol{\phi}(t)(\boldsymbol{\Phi}^T\boldsymbol{\Phi})^{-1}\boldsymbol{\Phi}^T\tilde{\boldsymbol{G}}_{\boldsymbol{n}} \tag{5.12}$$

The first derivative of $\tilde{F}_n(t)$ can be obtained by

$$\hat{\dot{F}}_n(t) = \dot{\boldsymbol{\phi}}(t)(\boldsymbol{\Phi}^T\boldsymbol{\Phi})^{-1}\boldsymbol{\Phi}^T\tilde{\boldsymbol{F}}_{\boldsymbol{n}} \tag{5.13}$$

Step 3: two-step least square estimation of $\hat{\theta}_1$, $\hat{\theta}_2$ and $\hat{D}$

Based on equation (5.10), we obtain $\hat{\theta}_1$ and $\hat{\theta}_2$ by minimizing

$$S_1(\theta_1, \theta_2) = \int_0^T \left[\hat{\dot{F}}_0(t) - \hat{G}_0(t)\theta_1 - \hat{F}_0(t)\theta_2\right]^2 dt \tag{5.14}$$

In order to estimate D, we plug the estimates of θ_1 and θ_2 in equation (5.11), and consider multiple ODEs. Suppose we look at the first $N_{X,est}$ equations, $\hat{D}$ is obtained by minimizing

$$S_2(D) = \sum_{n=1}^{N_{X,est}} \int_0^T \left[\hat{\dot{F}}_n(t) - \hat{\theta}_1\hat{G}_n(t) - \hat{\theta}_2\hat{F}_n(t) + \lambda_n\hat{F}_n(t)D\right]^2 dt \tag{5.15}$$

In practice, we are not minimizing the integral in mean squared error (5.14) or (5.15). Instead, we minimize mean squared error as

$$\hat{S}_1(\theta_1, \theta_2) = \frac{1}{n_t}\sum_{j=1}^{n_t} \left[\hat{\dot{F}}_0(t_j) - \hat{G}_0(t_j)\theta_1 - \hat{F}_0(t_j)\theta_2\right]^2 \tag{5.16}$$

and

$$\hat{S}_2(D) = \frac{1}{n_t}\sum_{n=1}^{N_{X,est}}\sum_{j=1}^{n_t} \left[\hat{\dot{F}}_n(t_j) - \hat{\theta}_1\hat{G}_n(t_j) - \hat{\theta}_2\hat{F}_n(t_j) + \lambda_n\hat{F}_n(t_j)D\right]^2 \tag{5.17}$$

Since ODE (5.10) and (5.11) are linear with respect to θ_1, θ_2 and D, $\hat{\theta}_1$, $\hat{\theta}_2$ and $\hat{D}$ are obtained by a 2-step linear least square estimation procedure.

$N_{X,est}$ is the number of equations used to estimate D. It is analog to the number of equations used in the Method of Moment. That is to say, $N_{X,est}$ can be fixed, which means that it is not necessary to have $N_{X,est} \to \infty$ when sample size gets larger. In practice, $N_{X,est}$ can be chosen with cross validation based on criteria of minimum prediction error. On the

other hand, $N_{T,est}$ is the number of basis functions used in smoothing step. The choice of $N_{T,est}$ is much more critical than $N_{X,est}$. In the following discussion of consistency and asymptotic normality, we treat $N_{X,est}$ as fixed and mainly discuss the asymptotic results when $N_{T,est}$ goes to infinity.

5.3 Consistency

5.3.1 Assumptions and Notations

In order to develop consistency and asymptotic normality of the proposed estimators, we need the following assumptions:

Assumption 10 *The source $G(\boldsymbol{x}, t)$, the first and the second partial derivatives of $G(\boldsymbol{x}, t)$ are uniformly bounded.*

Notice that, due to the relationship between $F(\boldsymbol{x}, t)$ and $G(\boldsymbol{x}, t)$, assumption 10 implies that the unknown dynamic $F(\boldsymbol{x}, t)$, the first and the second partial derivatives of $F(\boldsymbol{x}, t)$ are also uniformly bounded. This assumption is made to control the approximation error of pseudo data. Moreover, the consistency of smoothed data is required as well. Based on Newey's results [24], we define $|g|_d = \max_{|\Lambda|<d} \sup_{t\in[0,T]} |\partial^{|\Lambda|} g(x)/\partial x^{\Lambda_1} \cdots \partial x^{\Lambda_i}|$.

Assumption 11 *There exists α and $\beta_{N_{T,est}}$, such that $|G_n - \boldsymbol{\Phi}_{N_{T,est}} \boldsymbol{\beta}_{G,N_{T,est}}|_1 = O(N_{T,est}^{-\alpha})$ and $|F_n - \boldsymbol{\Phi}_{N_{T,est}} \boldsymbol{\beta}_{F,N_{T,est}}|_1 = O(N_{T,est}^{-\alpha})$ as $N_{T,est} \to \infty$.*

In the case of periodic function, without loss of generality, we assume that measurement period T is a multiple of period T_0. Thus, basis functions $\boldsymbol{\phi}(t) = \begin{bmatrix}\phi_1(t) & \cdots & \phi_{N_{T,est}}(t)\end{bmatrix}$

are orthogonal in each time period and satisfy

$$\sup_t \sqrt{\texttt{trace}(\boldsymbol{\phi}\boldsymbol{\phi}^T)} = \sqrt{\sum_{m=1}^{N_{T,est}} \phi_m^2(t)} \leq \sqrt{N_{T,est}}. \tag{5.18}$$

5.3.2 Consistency of pseudo data and smoothed data.

Since smoothed data is obtained from pseudo data, bias and variation of smoothed data can come from both smoothing and approximation in pseudo data. Under assumption 10, bias and variation of pseudo data $\tilde{G}_n(t)$ and $\tilde{F}_n(t)$ can be directly calculated based on approximation error of Right Riemann Summation, i.e., for all $n \neq m \geq 0$

$$\begin{aligned}
&\text{Bias}\left(\tilde{G}_n(t)\right) = O(\Delta\boldsymbol{x}) && \text{Bias}\left(\tilde{F}_n(t)\right) = O(\Delta\boldsymbol{x}) \\
&\text{Var}\left(\tilde{G}_n(t)\right) = \Delta\boldsymbol{x}\left(\sigma_g^2 + O(\Delta\boldsymbol{x})\right) \triangleq s_1 && \text{Var}\left(\tilde{F}_n(t)\right) = \Delta\boldsymbol{x}\left(\sigma_f^2 + O(\Delta\boldsymbol{x})\right) \triangleq s_2 \\
&\text{Cov}\left(\tilde{G}_n(t), \tilde{G}_m(t)\right) = O((\Delta\boldsymbol{x})^2) && \text{Cov}\left(\tilde{F}_n(t), \tilde{F}_m(t)\right) = O((\Delta\boldsymbol{x})^2)
\end{aligned}$$

The smoothing error is discussed below based on Neway's result [24]:

Theorem 12 *Define $\bar{F}_n(t)$, $\bar{G}_n(t)$, $\bar{\dot{F}}_n(t)$ as expectation of pseudo data $\tilde{F}_n(t)$, $\tilde{G}_n(t)$, $\tilde{\dot{F}}_n(t)$. Under assumption 11, suppose $N_{T,est}$ is chosen such that $N_{T,est}^2/n_t \to 0$ as $n_t \to \infty$, then we have smoothing error as*

$$\int_0^T |\bar{F}_n(t) - \hat{F}_n(t)|^2 dt = O_p(N_{T,est}/n_t + N_{T,est}^{-2\alpha}) \tag{5.19}$$

$$\int_0^T |\bar{G}_n(t) - \hat{G}_n(t)|^2 dt = O_p(N_{T,est}/n_t + N_{T,est}^{-2\alpha}) \tag{5.20}$$

$$\sup_t |\bar{\dot{F}}_n(t) - \hat{\dot{F}}_n(t)| = O_p(N_{T,est}/\sqrt{n_t} + N_{T,est}^{-\alpha}) \tag{5.21}$$

Therefore, by combining approximation and smoothing results, we can obtain the consistency of smoothed data as

Theorem 13 *Under assumption 10 and 11, suppose $N_{T,est}$ is chosen such that $N_{T,est}^2/n_t \to 0$ as $n_t \to \infty$, for any $n = 0, 1, \cdots$, consistency of smoothed data can be given by*

$$\int_0^T |F_n(t) - \hat{F}_0(t)|^2 dt = O_p(N_{T,est}/n_t + N_{T,est}^{-2\alpha} + n_x^{-2}) \triangleq O_p(c_{n_x,N_{T,est},n_t}) \tag{5.22}$$

$$\int_0^T |G_n(t) - \hat{G}_0(t)|^2 dt = O_p(N_{T,est}/n_t + N_{T,est}^{-2\alpha} + n_x^{-2}) \triangleq O_p(c_{n_x,N_{T,est},n_t}) \tag{5.23}$$

$$\sup_t |\dot{F}_n(t) - \hat{\dot{F}}_0(t)| = O_p(N_{T,est}/\sqrt{n_t} + N_{T,est}^{-\alpha+0.5} + n_x^{-1}) \triangleq O_p(b_{n_x,N_{T,est},n_t}) \tag{5.24}$$

Moreover, the smoothed data $\hat{\boldsymbol{F}}$, $\hat{\boldsymbol{G}}$ and $\hat{\dot{F}}$ follow multivariate normal distributions with the following variance-covariance matrix, i.e., for any $n \neq m \geq 0$,

$$\text{cov}(\hat{\boldsymbol{F}}_{\boldsymbol{n}}) = \boldsymbol{\Phi}(\boldsymbol{\Phi}^T\boldsymbol{\Phi})^{-1}\boldsymbol{\Phi}^T s_2 \qquad \text{cov}(\hat{\dot{\boldsymbol{F}}}_{\boldsymbol{n}}) = \dot{\boldsymbol{\Phi}}(\boldsymbol{\Phi}^T\boldsymbol{\Phi})^{-1}\dot{\boldsymbol{\Phi}}^T s_2 \tag{5.25}$$

$$\text{cov}(\hat{\boldsymbol{F}}_{\boldsymbol{n}}, \hat{\dot{\boldsymbol{F}}}_{\boldsymbol{n}}) = \boldsymbol{\Phi}(\boldsymbol{\Phi}^T\boldsymbol{\Phi})^{-1}\dot{\boldsymbol{\Phi}}^T s_2 \quad \text{cov}(\hat{\boldsymbol{G}}_{\boldsymbol{n}}) = \boldsymbol{\Phi}(\boldsymbol{\Phi}^T\boldsymbol{\Phi})^{-1}\boldsymbol{\Phi}^T s_1 \tag{5.26}$$

$$\text{cov}(\hat{\boldsymbol{F}}_{\boldsymbol{n}}, \hat{\boldsymbol{F}}_{\boldsymbol{m}}) = \boldsymbol{0} \qquad \text{cov}(\hat{\dot{\boldsymbol{F}}}_{\boldsymbol{n}}, \hat{\dot{\boldsymbol{F}}}_{\boldsymbol{m}}) = \boldsymbol{0} \tag{5.27}$$

$$\text{cov}(\hat{\boldsymbol{F}}_{\boldsymbol{n}}, \hat{\dot{\boldsymbol{F}}}_{\boldsymbol{m}}) = \boldsymbol{0} \qquad \text{cov}(\hat{\boldsymbol{G}}_{\boldsymbol{n}}, \hat{\boldsymbol{G}}_{\boldsymbol{m}}) = \boldsymbol{0} \tag{5.28}$$

5.3.3 Consistency of $\hat{\theta}_1$ and $\hat{\theta}_2$

$\hat{\theta}_1$ and $\hat{\theta}_2$ are obtained by minimizing $S_1(\theta_1, \theta_2)$ defined in (5.14). In order to prove that $\hat{\theta}_1$ and $\hat{\theta}_2$ are consistent estimators of θ_1 and θ_2, the key is to prove that $\lim_{n_t \to \infty} S_1(\theta_1, \theta_2)$ reaches its minimum at true values θ_1^* and θ_2^*.

The large sample behavior of $S_1(\theta_1, \theta_2)$ depends on consistency of smoothed data $\hat{\dot{F}}_0(t)$, $\hat{G}_0(t)$ and $\hat{F}_0(t)$. Based on our discussion of consistency of smoothed data and Theorem 13, we know that the smoothed data converge to true value with certain convergence

rate. Therefore, we can have

$$S_1(\theta_1, \theta_2) \to \int_0^T \left[\dot{F}_0(t) - G_0(t)\theta_1 - F_0(t)\theta_2\right]^2 dt$$
$$= \int_0^T \left[(\theta_1^* - \theta_1)G_0(t) + (\theta_2^* - \theta_2)F_0(t)\right]^2 dt$$

In fact, based on result in Theorem 13, with simple calculation and Cauchy inequality, we can prove that

Lemma 14 *Under assumption 10 and 11, suppose $N_{T,est}$ is chosen such that $N_{T,est}^2/n_t \to 0$ as $n_t \to \infty$ and parameter space $\mathbf{\Theta} = \{\theta_1, \theta_2, D\}$ is a compact space, then limit of objective function $S_1(\theta_1, \theta_2)$ is*

$$S_1(\theta_1, \theta_2) = \int_0^T \left[(\theta_1^* - \theta_1)G_0(t) + (\theta_2^* - \theta_2)F_0(t)\right]^2 dt + O_p(d_{n_x,n_t,N_{T,est}}) \tag{5.29}$$

where the error order $d_{n_x,n_t,N_{T,est}} = N_{T,est}^2/n_t + N_{T,est}^{-2\alpha+1} + n_x^{-2}$.

The detailed proof of Lemma 14 is given in the Appendix.

Notice that $\int_0^T \left[(\theta_1^* - \theta_1)G_0(t) + (\theta_2^* - \theta_2)F_0(t)\right]^2 dt$ is minimized at $\theta_1 = \theta_1^*$ and $\theta_2 = \theta_2^*$. Therefore, $\hat{\theta}_1$ and $\hat{\theta}_2$ are consistent estimator of θ_1 and θ_2 with convergence rate at $d_{n_x,n_t,N_{T,est}} = N_{T,est}^2/n_t + N_{T,est}^{-2\alpha+1} + n_x^{-2}$.

Theorem 15 *Under assumption 10 and 11, suppose $N_{T,est}$ is chosen such that $N_{T,est}^2/n_t \to 0$ as $n_t \to \infty$ and parameter space $\mathbf{\Theta} = \{\theta_1, \theta_2, D\}$ is a compact space, then the estimator $(\hat{\theta}_1, \hat{\theta}_2)$ are consistent estimator of (θ_1, θ_2).*

5.3.4 Consistency of $\hat{D}$

$\hat{D}$ is obtained by minimizing $S_2(D)$ defined in (5.15). Let D^* be the true value of D. Similar as the consistency of $\hat{\theta}_1$ and $\hat{\theta}_2$, it is critical to study the large sample behavior of

$S_2(D)$, which depends on consistency of smoothed data and estimator $\hat{\theta}_1$ and $\hat{\theta}_2$. We already discussed about consistency of $\hat{\dot{F}}_n(t)$ and $\hat{F}_n(t)$. Now we look at the limiting behavior of $\hat{\theta}_1\hat{G}_n$ and $\hat{\theta}_2\hat{F}_n$. Note that $\hat{\theta}_1$,$\hat{\theta}_2$ are consistent estimators of θ_1 and θ_2 with convergence rate $d_{n_x,N_{T,est},n_t}$, and that $\hat{G}_n(t)$ and $\hat{F}_n(t)$ converge to the true value of the functions with $\mathbb{L}_2$ convergence rate at $c_{n_x,N_{T,est},n_t}$. With simple calculation of Cauchy inequality, we can obtain the limiting behavior of $\hat{\theta}_1\hat{G}_n(t)$ and $\hat{\theta}_2\hat{F}_n(t)$ as

Lemma 16 *Under assumption 10, 11, suppose $N_{T,est}$ is chosen such that $N_{T,est}^2/n_t \to 0$ as $n_t \to \infty$, then we have*

$$\sum_{n=1}^{N_{X,est}} \int_0^T \left[\hat{\theta}_1\hat{G}_n(t) - \theta_1^* G_n(t)\right]^2 dt = O_p(c_{n_x,N_{T,est},n_t}) + O_p(d^2_{n_x,N_{T,est},n_t})$$
$$\sum_{n=1}^{N_{X,est}} \int_0^T \left[\hat{\theta}_2\hat{F}_n(t) - \theta_2^* F_n(t)\right]^2 dt = O_p(c_{n_x,N_{T,est},n_t}) + O_p(d^2_{n_x,N_{T,est},n_t})$$

Detailed proof of Lemma 16 is given in Appendix. Note that based on Theorem 13, Lemma 16 and Cauchy-Schwartz inequality, suppose $N_{T,est}^2/n_t \to 0$ as $n_t \to \infty$, we have

$$\sum_{n=1}^{N_{X,est}} \int_0^T \left[\hat{\dot{F}}_n - \hat{\theta}_1\hat{G}_n - \hat{\theta}_2\hat{F}_n - \dot{F}_n + \theta_1^* G_n + \theta_2^* F_n\right]^2 dt = O_p(N_{T,est}^2/n_t + N_{T,est}^{-2\alpha+1} + n_x^{-2}) \tag{5.30}$$

Furthermore, with the similar calculation as the proof in Lemma 14, we can obtain the limiting behavior of the objective function $S_2(D)$ as

$$S_2(D) = \sum_{n=1}^{N_{X,est}} \lambda_n^2 \int_0^T \left[(D^* - D)F_n\right]^2 dt + O_p(N_{T,est}^2/n_t + N_{T,est}^{-2\alpha+1} + n_x^{-2}) \tag{5.31}$$

Since $\sum_{n=1}^{N_{X,est}} \lambda_n^2 \int_0^T \left[(D^* - D)F_n\right]^2 dt$ is minimized at $D = D^*$, we have the following result:

Theorem 17 *Under assumption 10, 11, suppose* $N_{T,est}^2/n_t \to 0$ *as* $n_t \to \infty$*, if parameter space* $\mathbf{\Theta} = \{\theta_1, \theta_2, D\}$ *is a compact space, the estimator* $\hat{D}$ *is a consistent estimator of* D *with convergence rate as* $O_p(N_{T,est}^2/n_t + N_{T,est}^{-2\alpha+1} + n_x^{-2})$.

5.4 Asymptotic Normality

5.4.1 Asymptotic Normality of $\hat{\theta}_1$ and $\hat{\theta}_2$

Since $\hat{\theta}_1$ and $\hat{\theta}_2$ are obtained by minimizing $S_1(\theta_1, \theta_2)$, $\hat{\theta}_1$ and $\hat{\theta}_2$ are solutions of

$$\frac{\partial S_1}{\partial \boldsymbol{\theta}} = \begin{pmatrix} -2\int_0^T \left[\hat{\dot{F}}_0(t) - \hat{G}_0(t)\theta_1 - \hat{F}_0(t)\theta_2\right]\hat{G}_0(t)dt \\ -2\int_0^T \left[\hat{\dot{F}}_0(t) - \hat{G}_0(t)\theta_1 - \hat{F}_0(t)\theta_2\right]\hat{F}_0(t)dt \end{pmatrix} = 0$$

With taylor expansion at $(\theta_1, \theta_2) = (\theta_1^*, \theta_2^*)$, we have

$$\begin{pmatrix} \hat{\theta}_1 \\ \hat{\theta}_2 \end{pmatrix} - \begin{pmatrix} \theta_1^* \\ \theta_2^* \end{pmatrix} = \begin{pmatrix} ||\hat{G}_0(t)||^2 & \langle \hat{F}_0(t), \hat{G}_0(t)\rangle \\ \langle \hat{G}_0(t), \hat{F}_0(t)\rangle & ||\hat{F}_0(t)||^2 \end{pmatrix}^{-1} \times \begin{pmatrix} \langle \hat{G}_0(t)\theta_1^* + \hat{F}_0(t)\theta_2^* - \hat{\dot{F}}_0(t), \hat{G}_0(t)\rangle \\ \langle \hat{G}_0(t)\theta_1^* + \hat{F}_0(t)\theta_2^* - \hat{\dot{F}}_0(t), \hat{F}_0(t)\rangle \end{pmatrix} \tag{5.32}$$

Based on consistency of smoothed data, we have

$$\begin{pmatrix} ||\hat{G}_0(t)||^2 & \langle \hat{F}_0(t), \hat{G}_0(t)\rangle \\ \langle \hat{G}_0(t), \hat{F}_0(t)\rangle & ||\hat{F}_0(t)||^2 \end{pmatrix}^{-1} \to \begin{pmatrix} ||G_0(t)||^2 & \langle F_0(t), G_0(t)\rangle \\ \langle G_0(t), F_0(t)\rangle & ||F_0(t)||^2 \end{pmatrix}^{-1} \triangleq \boldsymbol{A_1}^* \tag{5.33}$$

For $\begin{pmatrix} \langle \hat{G}_0(t)\theta_1^* + \hat{F}_0(t)\theta_2^* - \dot{\hat{F}}_0(t), \hat{G}_0(t)\rangle \\ \langle \hat{G}_0(t)\theta_1^* + \hat{F}_0(t)\theta_2^* - \dot{\hat{F}}_0(t), \hat{F}_0(t)\rangle \end{pmatrix}$, in practice the $\mathbb{L}_2$ inner products are approximated by summation of smoothed data as

$$\frac{T}{n_t}\begin{pmatrix} \hat{\boldsymbol{G}}_{\boldsymbol{0}}{}^T \\ \hat{\boldsymbol{F}}_{\boldsymbol{0}}{}^T \end{pmatrix}\begin{pmatrix} -\theta_1^*\boldsymbol{I}_{\boldsymbol{n_t}} & -\theta_2^*\boldsymbol{I}_{\boldsymbol{n_t}} & \boldsymbol{I}_{\boldsymbol{n_t}} \end{pmatrix}\begin{pmatrix} \hat{\boldsymbol{G}}_{\boldsymbol{0}} - \mathbb{E}(\hat{\boldsymbol{G}}_{\boldsymbol{0}}) \\ \hat{\boldsymbol{F}}_{\boldsymbol{0}} - \mathbb{E}(\hat{\boldsymbol{F}}_{\boldsymbol{0}}) \\ \dot{\hat{\boldsymbol{F}}}_{\boldsymbol{0}} - \mathbb{E}(\dot{\hat{\boldsymbol{F}}}_{\boldsymbol{0}}) \end{pmatrix} \tag{5.34}$$

According to consistency and asymptotic normality of smoothed data, we can obtain

Lemma 18 *Under the assumptions 10 and 11, suppose $N_{T,est}$ is chosen such that $N_{T,est}^2/n_t \to 0$ as $n_t \to \infty$, then* $\begin{pmatrix} \langle \hat{G}_0(t)\theta_1^* + \hat{F}_0(t)\theta_2^* - \dot{\hat{F}}_0(t), \hat{G}_0(t)\rangle \\ \langle \hat{G}_0(t)\theta_1^* + \hat{F}_0(t)\theta_2^* - \dot{\hat{F}}_0(t), \hat{F}_0(t)\rangle \end{pmatrix}$ *follows multivariate normal distribution with mean zero and variance-covariance matrix* $\boldsymbol{B_1} \to \frac{T\Delta x}{n_t}\boldsymbol{B_1}^*$, *where* $\boldsymbol{B_1}^* = \begin{pmatrix} \sigma_{11} & \sigma_{12} \\ \sigma_{12} & \sigma_{22} \end{pmatrix}$ *and*

$$\sigma_{11} = \theta_1^{*^2}||G_0(t)||^2\sigma_g^2 + ||\theta_2^*G_0(t) - \dot{G}_0(t)||^2\sigma_f^2$$

$$\sigma_{12} = \theta_1^{*^2}\langle G_0(t), F_0(t)\rangle\sigma_g^2 + \langle \theta_2^*G_0(t) - \dot{G}_0(t), \theta_2^*F_0(t) - \dot{F}_0(t)\rangle\sigma_f^2$$

$$\sigma_{22} = \theta_1^{*^2}||F_0(t)||^2\sigma_g^2 + ||\theta_2^*F_0(t) - \dot{F}_0(t)||^2\sigma_f^2$$

Detailed proof of Lemma 18 is given in Appendix. Let $\boldsymbol{\Sigma}^* = \boldsymbol{A_1}^*\boldsymbol{B_1}^*\boldsymbol{A_1}^*$. According to equation (5.32), (5.33) and Lemma 18, asymptotic normality of $\hat{\theta}_1$ and $\hat{\theta}_2$ can be given as

Theorem 19 *Under the assumptions 10 and 11, supporse $N_{T,est}$ is chosen such that $\frac{N_{T,est}^2}{n_t} \to 0$ as $n_t \to \infty$ and parameter space $\boldsymbol{\Theta} = \{\theta_1, \theta_2, D\}$ is a compact space, then*

$$\sqrt{\frac{n_t}{T\Delta \boldsymbol{x}}}\left(\begin{pmatrix} \hat{\theta}_1 \\ \hat{\theta}_2 \end{pmatrix} - \begin{pmatrix} \theta_1^* \\ \theta_2^* \end{pmatrix}\right) \xrightarrow{d} \mathit{MVN}\left(\begin{pmatrix} 0 \\ 0 \end{pmatrix}, \boldsymbol{\Sigma}^*\right) \tag{5.35}$$

5.4.2 Asymptotic Normality of $\hat{D}$

Since $\hat{D}$ is obtained by minimizing $S_2(D)$, $\hat{D}$ is the solution to

$$\frac{\partial S_2}{\partial D} = \sum_{n=1}^{N_{X,est}} 2\int_0^T \left[\hat{\dot{F}}_n(t) - \hat{\theta}_1\hat{G}_n(t) - \hat{\theta}_2\hat{F}_n(t) + \lambda_n\hat{F}_n(t)D\right]\lambda_n\hat{F}_n(t)dt = 0$$

With Taylor expansion at $D = D^*$, we know that the difference between our estimator and the true value can be evaluated as

$$\hat{D} - D^* = \left[\sum_{n=1}^{N_{X,est}} \lambda_n^2||\hat{F}_n(t)||^2\right]^{-1} \sum_{n=1}^{N_{X,est}} \langle\hat{\dot{F}}_n(t) - \hat{\theta}_1\hat{G}_n(t) - \hat{\theta}_2\hat{F}_n(t) + \lambda_n\hat{F}_n(t)D^*, -\lambda_n\hat{F}_n(t)\rangle \tag{5.36}$$

Based on consistency and normality of smoothed data, we have

$$\left[\sum_{n=1}^{N_{X,est}} \lambda_n^2||\hat{F}_n(t)||^2\right]^{-1} \to \left[\sum_{n=1}^{N_{X,est}} \lambda_n^2||F_n(t)||^2\right]^{-1} \triangleq \boldsymbol{A_2}^* \tag{5.37}$$

Moreover, with similar logic as the proof of Lemma 18, we have

Lemma 20 *Under assumption 10, 11, suppose $N_{T,est}$ is chosen such that $N_{T,est}^2/n_t \to 0$ as $n_t \to \infty$, then we have $\sum_{n=1}^{N_{X,est}} \langle\hat{\dot{F}}_n(t) - \hat{\theta}_1\hat{G}_n(t) - \hat{\theta}_2\hat{F}_n(t) + \lambda_n\hat{F}_n(t)D^*, -\lambda_n\hat{F}_n(t)\rangle$ is asymptotically normally distributed with mean zero and variance $\frac{T\Delta\boldsymbol{x}}{n_t}(B_{21}^* + B_{22}^*)$, where $B_{21}^* = \sum_{n=1}^{N_{X,est}} \left[b_{21}^{xxn*} + b_{21}^{xyn*} + b_{21}^{yyn*}\right]$, $B_{22}^* = \boldsymbol{b_{22}}^*\boldsymbol{\Sigma}^*\boldsymbol{b_{22}}^{*T}$, and*

$$b_{21}^{xxn*} = \lambda_n^4||F_n(t)||^2\sigma_f^2$$

$$b_{21}^{xyn*} = -2D^*\lambda_n^3\left[\theta_2^*||F_n(t)||^2\sigma_f^2 - \langle F_n(t), \dot{F}_n(t)\rangle\sigma_f^2\right]$$

$$b_{21}^{yyn*} = \lambda_n^2\left[\theta_2^*||F_n(t)||^2\sigma_f^2 + ||\dot{F}_n(t)||^2\sigma_f^2 + \theta_1^{*2}||F_n(t)||^2\sigma_g^2 - 2\theta_2^*\langle F_n(t), \dot{F}_n(t)\rangle\sigma_f^2\right]$$

$$\boldsymbol{b_{22}}^* = \begin{pmatrix} \sum_{n=1}^{N_{X,est}} \lambda_n\langle F_n(t), G_n(t)\rangle & \sum_{n=1}^{N_{X,est}} \lambda_n||F_n(t)||^2 \end{pmatrix}$$

Detailed proof of Lemma 20 is given in Appendix. Let $\sigma^{*2} = A_2^*(B_{21}^* + B_{22}^*)A_2^*$. According to equation (5.36), (5.37) and Lemma 20, asymptotic normality of $\hat{D}$ can be given as

Theorem 21 *Under assumption 10 and 11, Supporse $N_{T,est}$ is chosen such that $\frac{N_{T,est}^2}{n_t} \to 0$ as $n_t \to \infty$ and parameter space $\boldsymbol{\Theta} = \{\theta_1, \theta_2, D\}$ is a compact space, then*

$$\sqrt{\frac{n_t}{T\Delta \boldsymbol{x}}}\left(\hat{D} - D^*\right) \xrightarrow{d} N\left(0, \sigma^{*2}\right) \tag{5.38}$$

5.5 Implementation of Proposed Method and Simulation

As discussed in the end of section 5.2.3, although it is not necessary to have $N_{X,est} \to \infty$ when sample size gets larger, we still need to choose $N_{X,est}$ properly. Moreover, the choice of $N_{T,est}$, the number of basis functions used in smoothing step, is always crucial. Therefore, in terms of the implementation of the proposed method, we want to choose $N_{T,est}$ and $N_{X,est}$ by cross validation. In the smoothing-pseudo-data step, $N_{T,est}$ can be chosen to smooth $\tilde{G}_n(t)$ and $\tilde{F}_n(t)$ with general cross validation (GCV) method. Notice that in this case, $N_{T,est}$ can be different for $\tilde{G}_n(t)$ and $\tilde{F}_n(t)$. In the parameter estimation step, we can conduct 10-fold cross validation to choose the number of equations $N_{X,est}$ based on the criterion of optimal predicted error, which is defined as the sum of square of difference between data $f(\boldsymbol{x}_i, t_j)$ and the predicted value $\hat{f}(\boldsymbol{x}_i, t_j)$ by plugging in the parameter estimators and solving PDE (5.2). Notice that in order to solve PDE (5.2), not only the parameter estimators but also source $G(\boldsymbol{x}, t)$ and initial values $F(\boldsymbol{x}, t = 0)$ are needed. In this case, we plug in smoothed data $\tilde{G}(\boldsymbol{x}, t)$ and initial values $\tilde{F}(\boldsymbol{x}, t = 0)$.

In this section, we will first describe how we smooth $G(\boldsymbol{x}, t)$ and $F(\boldsymbol{x}, t = 0)$. Then, we will discuss about the details of the cross validation procedure implemented for

choosing $N_{X,est}$ and $N_{T,est}$. In the end, we will give a summary of steps to implement the proposed method.

5.5.1 Smoothing Procedure of $G(\boldsymbol{x}, t)$

In terms of smoothing, we have a lot of technique to choose from, such as local polynomial method, smoothing with spline, kernel smoothing, etc. In our particular case, $G(\boldsymbol{x}, t)$, $F(\boldsymbol{x}, t)$ can be decomposed by eigenfunctions $\{\varphi_n(\boldsymbol{x})\}_{n=1}^{\infty}$, and the coefficient functions can be smoothed by projection technique. So we smooth function $G(\boldsymbol{x}, t)$ based on decomposition as

$$G(\boldsymbol{x}, t) = \sum_{n=1}^{\infty} G_n(t)\varphi_n(\boldsymbol{x}) = \sum_{n=1}^{\infty}\sum_{m=1}^{\infty} g_{nm}\phi_m(t)\varphi_n(\boldsymbol{x}) \quad (\boldsymbol{x}, t) \in \Omega \times [0, T]. \tag{5.39}$$

where $G_n(t) = \int_{\Omega} G(\boldsymbol{x}, t)\varphi_n(\boldsymbol{x})d\boldsymbol{x}$. Therefore, we first obtain coefficient function $G_n(t)$ by Right Riemann Summation, which is the same as how we obtained pseudo data in parameter estimation procedure. Then we smoothed $G_n(t)$ by projection technique with basis function $\{\phi_m(t)\}_{m=1}^{N_{T,smooth}}$, which is similar as how we smoothed pseudo data in parameter estimation procedure. In the end, we plug in smoothed $G_n(t)$ back to the decomposition, $G(\boldsymbol{x}, t) = \sum_{n=1}^{N_{X,smooth}} G_n(t)\varphi_n(\boldsymbol{x})$, to get smoothed $G(\boldsymbol{x}, t)$. Notice that since the actual basis functions for smoothing $G(\boldsymbol{x}, t)$ are $\{\phi_m(t)\varphi_n(\boldsymbol{x})\}_{n=1,m=1}^{N_{X,smooth},N_{T,smooth}}$, the number of basis function $\{\phi_m(t)\}$, $N_{T,smooth}$ should be the same across different $G_n(t)$, for $n = 0, 1, \cdots$. In this case, $N_{T,smooth}$ and $N_{X,smooth}$ are chosen based on 10-fold cross validation. Therefore, we smooth $G(\boldsymbol{x}, t)$ with the following procedure:

Step 1: In this step, we choose a proper combination of $N_{X,smooth}$ and $N_{T,smooth}$ to smooth $G(\boldsymbol{x}, t)$ with 10-fold cross validation. We first randomly partition our data into

10 equal-size subsets $\{\mathbb{A}_k\}_{k=1}^{10}$. For each time, we treat $\mathbb{A}_k$ as testing data and the rest 9 subsets as training data. We smooth function $G(\boldsymbol{x}, t)$ based on training data, then evaluate smoothed function $\tilde{G}(\boldsymbol{x}, t)$ at testing data points. Define smoothing error as sum of squares of difference between data $g(\boldsymbol{x}, t)$ and the smoothed function $\tilde{G}(\boldsymbol{x}, t)$ at testing data points.

$$PEsmooth_k(N_{T,smooth}, N_{X,smooth}) = \sum_{(\boldsymbol{x}_i, t_j) \in \mathbb{A}_k} \Big(g(\boldsymbol{x}_i, t_j) - \tilde{G}(\boldsymbol{x}_i, t_j) \Big)^2$$

The best combination of $N_{X,smooth}$ and $N_{T,smooth}$ is chosen by minimizing mean of smoothing error across 10 folds:

$$PEsmooth(N_{T,smooth}, N_{X,smooth}) = \frac{1}{10} \sum_{k=1}^{10} PEsmooth_k(N_{T,smooth}, N_{X,smooth})$$

Step 2: In this step, we smoothed $G(\boldsymbol{x}, t)$ with the best combination of $N_{X,smooth}$ and $N_{T,smooth}$.

5.5.2 Cross Validation in Parameter Estimation Procedure

First, we need to decide $N_{T,est}$, the number of basis function in smoothing step of parameter estimation procedure. Notice that $N_{T,est}$ chosen in this step is different from $N_{T,smooth}$ chosen in smoothing procedure described in section 5.5.1. In section 5.5.1, our goal is to smooth function $G(\boldsymbol{x}, t)$ so $N_{T,smooth}$ is chosen based on criterion of minimum predicted error of smoothed data $\tilde{G}(\boldsymbol{x}, t)$. However, now we are working on smoothing of pseudo data $\tilde{F}_n(t)$ and $\tilde{G}_n(t)$. So in this smoothing step, we can choose different $N_{T,est}$ for different $\tilde{F}_n(t)$ and $\tilde{G}_n(t)$ based on generalized cross validation(GCV) method. GCV criterion is defined as

$$GCV_{Fn}(N_{T,est}) = \frac{n_t || \boldsymbol{\Phi} \left[\boldsymbol{\Phi}^T \boldsymbol{\Phi} \right]^{-1} \boldsymbol{\Phi}^T \tilde{\boldsymbol{F}}_{\boldsymbol{n}} - \tilde{\boldsymbol{F}}_{\boldsymbol{n}} ||^2}{\Big(n_t - \text{Trace}(\boldsymbol{\Phi} \left[\boldsymbol{\Phi}^T \boldsymbol{\Phi} \right]^{-1} \boldsymbol{\Phi}^T) \Big)^2}$$

$$GCV_{Gn}(N_{T,est}) = \frac{n_t||\mathbf{\Phi}\left[\mathbf{\Phi}^T\mathbf{\Phi}\right]^{-1}\mathbf{\Phi}^T\tilde{\boldsymbol{G}}_{\boldsymbol{n}} - \tilde{\boldsymbol{G}}_{\boldsymbol{n}}||^2}{\left(n_t - \text{Trace}(\mathbf{\Phi}\left[\mathbf{\Phi}^T\mathbf{\Phi}\right]^{-1}\mathbf{\Phi}^T)\right)^2}$$

where $\mathbf{\Phi}$ is basis function matrix which is of size $n_t \times N_{T,est}$, n_t is the number of time points, and $n = 1, 2, \cdots, N_{X,est}$. we minimize $GCV_{Fn}(N_{T,est})$ and $GCV_{Gn}(N_{T,est})$ to obtain desired $N_{T,est}(Fn)$ and $N_{T,est}(Gn)$ to smooth $\tilde{F}_n(t)$ and $\tilde{G}_n(t)$.

With smoothed $\hat{G}_0(t)$ and $\hat{F}_0(t)$, we can estimate θ_1 and θ_2. However, we need to decide $N_{X,est}$, the number of equations used for D estimation. Here we use 10-fold cross validation to choose desired $N_{X,est}$ based on the criterion of minimum prediction error of PDE (5.2) solution $F(\boldsymbol{x}, t)$. Similar as in section 5.5.1, we randomly partition $\hat{F}_n(t)$ and $\hat{G}_n(t)$ into 10 equal-size subsets $\{\mathbb{B}_k\}_{k=1}^{10}$ by subsetting time point $\{t_j\}_{j=1}^{n_t}$. Within each fold, we train, test and evaluate performance in the following procedure:

- We treat $\mathbb{B}_k$ as testing data and the rest 9 subsets as training data. For each N_X, we first estimate D with training data.

- We plug smoothed data $\tilde{G}(\boldsymbol{x}_i, t_j)$, $\tilde{F}(\boldsymbol{x}_i, t = 0)$ as initial values and estimators $\hat{\theta}_1$, $\hat{\theta}_2$ and $\hat{D}(N_{X,est})$ into model to solve PDE (5.2), and obtain prediction $\hat{F}(\boldsymbol{x}_i, t_j)$.

- We evaluate performance of parameter estimation procedure at $N_{X,est}$ using prediction error, which is defined as the sum of squares of difference between data $f(\boldsymbol{x}_i, t_j)$ and $\hat{F}(\boldsymbol{x}_i, t_j)$ on testing data:

$$PE_k(N_{X,est}) = \sum_{(\boldsymbol{x}_i, t_j) \in \mathbb{B}_k} \left(f(\boldsymbol{x}_i, t_j) - \hat{F}(\boldsymbol{x}_i, t_j)\right)^2 \tag{5.40}$$

$N_{X,est}$ is chosen by minimizing the average of prediction errors across all 10 folds:

$$PE(N_{X,est}) = \frac{1}{10}\sum_{k=1}^{10} PE_k(N_{X,est}) \tag{5.41}$$

5.5.3 Implementation of Proposed Method

In summary, the proposed method is implemented with the following steps: (1) smoothing data $f(x_i, t_j)$ and $g(x_i, t_j)$ with procedure in section 5.5.1; (2) obtaining pseudo data; (3) smoothing pseudo data with $N_{T,est}$ chosen by GCV; (4) estimating θ_1 and θ_2 with smoothed data $\hat{F}_0(t)$ and $\hat{G}_0(t)$; (5) choosing $N_{X,est}$ with 10-fold cross validation; (6) Estimating D with smoothed data $\hat{F}_n(t)$ and $\hat{G}_n(t)$ with $n = 1, 2, \cdots, N_{X,est}$.

5.6 Simulation

In this section, simulation studies are conducted with different set-ups of source function $G(\boldsymbol{x}, t)$ and true parameters θ_1, θ_2 and D. All the estimation procedures were implemented in R. We first choose two sets of source function with different spatial-temporal patterns. In addition, we use our pollen tube tip growth set-ups as true values for simulation. For each set-up, we first fix the number of equation used to estimate D, $N_{X,est} = 2$, conduct simulation study, and compare simulated standard error with theoretic standard error provided in Theorem 19 and 21. Moreover, we conduct simulation study with $N_{X,est}$ selected by 10-fold cross validation to evaluate proposed procedure implementation. For all three set-ups, we choose $N_{X,est}$ and $N_{T,est}$ from $1, 2, \cdots, 10$.

5.6.1 Simulation with arbitrary source $G(x,t)$

Set-up 1:

In this set-up, we choose $\theta_1 = 1$, $\theta_2 = -0.5$, $D = 0.1$, and source function $G(x,t)$ is defined as a periodic function with single-peak spatial pattern (See Fig 5.1b) as

$$G(x,t) = (\sin(2\pi t/5) + 1) * (e^{-(x-0.5)^2/0.02}) + 1.$$

With initial value $F(x, t = 0) = e^{-\frac{(x-0.4)^2}{0.02}}$, we can solve PDE (5.2) and obtain the true value of solution $F(x,t)$ (See Fig 5.1a). As shown in Fig 5.1, $F(x,t)$ and $G(x,t)$ are in

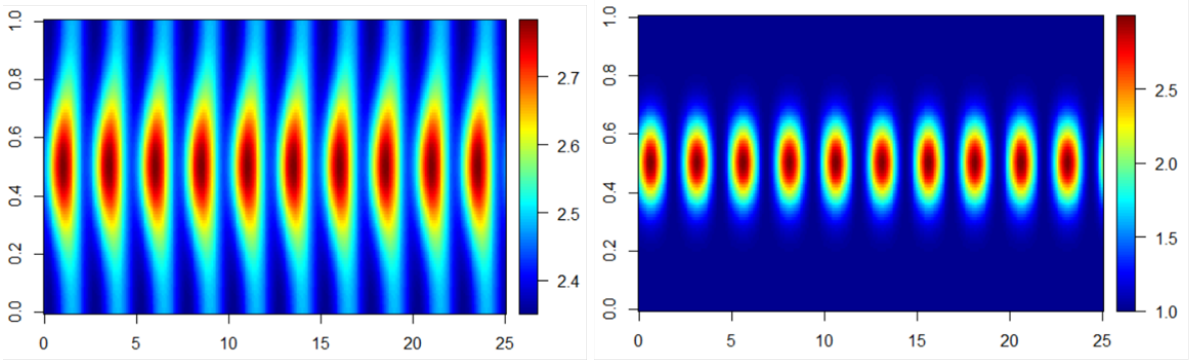

(a) True value of $F(x,t)$ (b) True value of $G(x,t)$

Figure 5.1: Spatial-temporal pattern of $F(x,t)$ and $G(x,t)$ in set-up 1

$[2.4, 2.7]$ and $[1, 2.5]$, respectively, so we choose noise of $F(x,t)$ and $G(x,t)$ as $\sigma_f = 0.3$ and $\sigma_g = 1$. We simulate data from $t \in [0, 25]$ with sample sizes $n_t = 251$ and $n_x = 101$. The simulation is conducted 1000 times and the results are summarized in table 5.1.

Set-up 2:

In this set-up, we choose $\theta_1 = 2$, $\theta_2 = 0.8$, $D = 0.2$, and source function $G(x,t)$ is defined

Table 5.1: Simulation of parameter estimation procedure for model (5.2) with set-up 1. SE: simulated standard error; SE* and covProb*: theoretical standard error and coverage provability obtained based on true value and Theorem 19 and 21; SE** and covProb**: theoretical standard error and coverage probability obtained based on estimated value and Theorem 19 and 21.

	θ_1 (1)		θ_2 (-0.5)		D (0.1)	
	$N_X = 2$	CV	$N_X = 2$	CV	$N_X = 2$	CV
bias	-0.0070	0.0051	0.0033	0.0025	-0.0051	-0.0014
SE	0.0447	0.0462	0.0225	0.0231	0.0075	0.0060
SE*	0.0452		0.0228		0.0070	
SE**	0.0450		0.0227		0.0068	
MSE	2.0468e-3	2.1572e-3	5.1710e-4	5.4051e-4	8.2487e-5	3.7848e-5
covProb*	0.954		0.952		0.868	
covProb**	0.947		0.948		0.851	

as a periodic function with double-peak spatial pattern (See Fig 5.2b) as

$$G(x,t) = (\sin(2\pi t/5) + 1) * (e^{(x-0.25)^2/0.02} + e^{(x-0.75)^2)/0.02} + 1.$$

With initial value $F(x, t = 0) = e^{-\frac{(x-0.25)^2}{0.02}} + e^{-\frac{(x-0.75)^2}{0.02}}$, we can solve PDE (5.2) to obtain the true value of solution $F(x,t)$ (See Fig 5.2a).

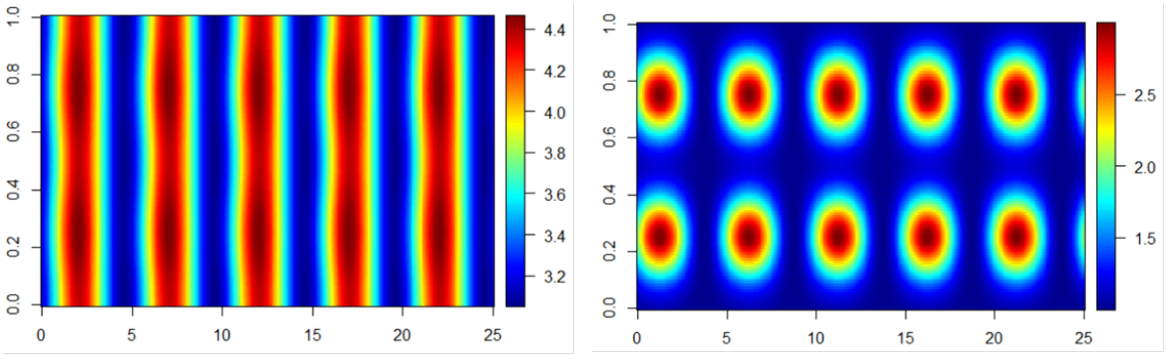

(a) True value of $F(x,t)$ (b) True value of $G(x,t)$

Figure 5.2: Spatial-temporal pattern of $F(x,t)$ and $G(x,t)$ in set-up 2

As shown in Fig 5.2, for each time point, the variation of $F(x,t)$ along spatial

dimension is quite small so we choose noise of $F(x,t)$ as $\sigma_f = 0.5$. However, the variation of $G(x,t)$ along spatial dimension is very large so we choose noise of $G(x,t)$ as $\sigma_g = 1.5$. We simulate the data from $t \in [0, 25]$ with sample size $n_t = 251$ and $n_x = 101$. The simulation is conducted 1000 times and the results are summarized in 5.2.

Table 5.2: Simulation of parameter estimation procedure for model (5.2) with set-up 2. SE: simulated standard error; SE* and covProb*: theoretical standard error and coverage provability obtained based on true value and Theorem 19 and 21; SE** and covProb**: theoretical standard error and coverage probability obtained based on estimated value and Theorem 19 and 21.

	θ_1 (2)		θ_2 (-0.8)		D (0.2)	
	$N_X = 2$	CV	$N_X = 2$	CV	$N_X = 2$	CV
bias	-0.0132	-0.01508	0.0050	0.0062	-0.0128	0.0135
SE	0.0665	0.0657	0.02717	0.0267	0.0293	0.0281
SE*	0.0647		0.0264		0.0274	
SE**	0.0643		0.0262		0.0257	
MSE	4.5993e-3	4.5450e-3	7.6278e-4	7.5051e-4	1.0203e-3	9.6992e-4
covProb*	0.943		0.953		0.91	
covProb**	0.939		0.945		0.854	

Interpretation of simulation results:

For each sets of source function, we did two simulation studies: (1) we fixed $N_{X,est} = 2$ and use cross validation to choose $N_{X,smooth}$, $N_{T,smooth}$ and $N_{T,est}$; (2) we choose all the numbers of basis functions, $N_{X,smooth}$, $N_{T,smooth}$, $N_{T,est}$ and $N_{X,est}$ with cross validation as described in section 5.5. In table 5.1 and 5.2, true value of each parameter is labeled in the parentheses. First, we look at results of cases where we fix $N_{X,est} = 2$ and where we choose $N_{X,est}$ with cross validation separately and draw the following conclusions:

1. Compared with the true value of each parameter, bias, standard error (SE) and mean squared error (MSE) are relatively small in both set-ups. It shows that our proposed

parameter estimators are consistent, and that the sample size chosen in this simulation study is sufficiently large for convergence.

2. In table 5.1 and 5.2, we provides two types of standard error. One is obtained as standard deviation of 1000-times simulation labeled as "SE" in table 5.1 and 5.2, and the other is calculated based on Theorem 19 and 21 as "SE*" or "SE**". Notice that standard error can only be calculated theoretically in the case when we fix the number of equations used in parameter estimation, $N_{X,est} = 2$. In this case, based on results in table 5.1 and 5.2, we concluded that the simulation results and theoretical values are close to each other as expected, suggesting good convergence behavior warranted by asymptotic theory.

3. The "covProb" in the table represents coverage probability, which is the proportion of 95% CI that includes true value among 1000-times simulation. We expect it to be closed to 0.95 if asymptotic normality is valid. Based on results in table 5.1 and 5.2, we find out that the coverage probability of θ_1 and θ_2 is closed to 0.95. However, the coverage probability of D is 0.868 and 0.91 for set-up 1 and set-up 2, respectively. In order to explain this difference, we check the distribution of $\hat{D}$ by QQ-plots (Fig 5.3), in which the straight line indicates normal distribution with true value of D and theoretical value of SE($\hat{D}$) from Theorem 21. From Fig 5.3, we can see that the deviation between coverage probability of D and 0.95 is caused by bias, difference between theoretical value and simulated value of SE, and deviation from normality in tails parts which is caused by approximation in calculation of distribution of $\hat{\theta_1}\hat{G}_n(t)$ and $\hat{\theta_2}\hat{F}_n(t)$, all of which can be improved with larger sample size.

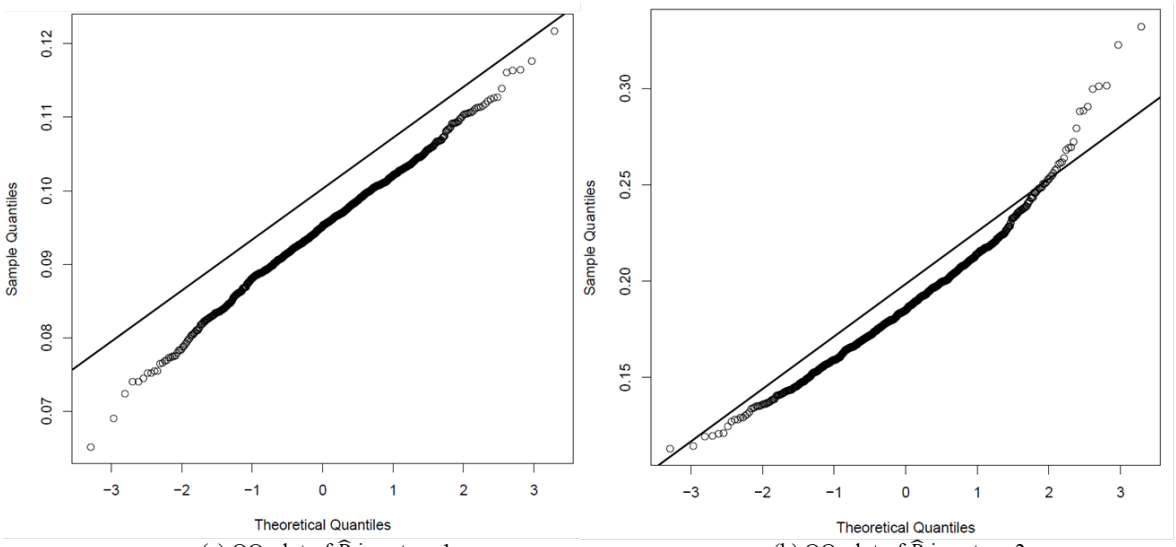

(a) QQ-plot of $\widehat{D}$ in set-up 1

(b) QQ-plot of $\widehat{D}$ in set-up 2

Figure 5.3: QQ plot for normality check of $\hat{D}$

Now we compare between results of case where we fix $N_{X,est} = 2$ and where we choose $N_{X,est}$ with cross validation. Based on table 5.1 and 5.2, we have following conclusions:

1. In terms of reaction rate θ_1 and θ_2, bias, SE, MSE in both cases are similar. This results is what we expect because the only difference between both cases are how to choose $N_{X,est}$, the number of equation used for D estimation, which does not involves in parameter estimation procedure of θ_1 and θ_2. Therefore, results of θ_1 and θ_2 should be similar between case where we fix $N_{X,est} = 2$ and where we choose $N_{X,est}$ with cross validation.

2. In terms of diffusion rate D,it shows that MSE of $\hat{D}$ is smaller in case where $N_{X,est}$ is chosen with cross validation than in case where $N_{X,est} = 2$, which indicates a better performance when $N_{X,est}$ is chosen with cross validation as expected.

5.6.2 Simulation with pollen tube tip growth model

In this section, we investigate how proposed procedure performs on our pollen tube model (2.15) through simulation study. We first solve model (2.15) with a set of parameters as

$$\begin{aligned} \alpha = 1.5 \quad L = 2.5\pi \quad R_{tot} = 5\pi \quad D_r = 0.1 \quad D_c = 10 \\ k_{pf} = \frac{0.72}{\pi} \quad k_{nf} = 3.6 \quad k_c = 0.15 \quad k_{ac} = 1 \quad k_{dc} = 0.4 \end{aligned} \tag{5.42}$$

and initial values $R(x, t = 0) = C(x, t = 0) = 0.0259 - 0.01\cos(4x)$. Then, the solution of model (2.15) is shown in Fig 5.4.

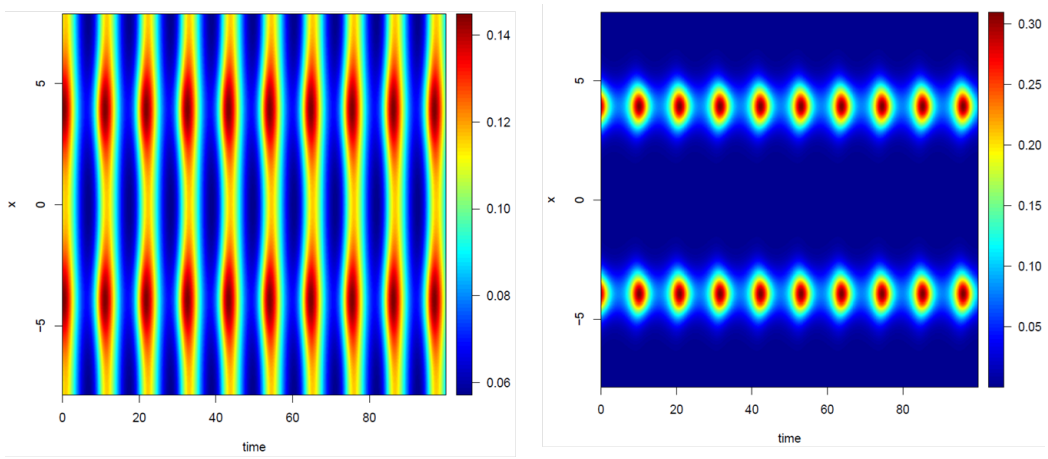

(a) True value of $C(x, t)$ (b) True value of $R(x, t)$

Figure 5.4: Spatial-temporal pattern of $C(x, t)$ and $R(x, t)$ as solution of model (2.15) with parameter as (5.42).

Note that C_t function in model (2.15) is in the same form of linear reaction diffusion equation as model (5.2). Therefore, we can treat $R(x, t)$ and $C(x, t)$ as true value of $G(x, t)$ and $F(x, t)$, respectively. In this case, k_{ac}, k_{dc} and D_c in model (2.15) can be considered as θ_1, θ_2 and D_c in model (5.2), which can be estimated by our proposed method.

Based on this idea, we conduct simulation with our pollen tube model. In this

case, true value of k_{ac}, k_{dc} and D_c are 1, 0.4, and 10. Moreover, as shown in Fig 5.4, at each time point, range of $C(x,t)$ and $R(x,t)$ is 0.02 and 0.2 respectively, so we set noise of $C(x,t)$ and $R(x,t)$ as $\sigma_c = 0.01$ and $\sigma_r = 0.05$. We simulated data from $t \in [0, 97.2]$, which included 9 entire periods of oscillation. We conducted simulation studies with different sample sizes. The results based on 1000 simulations are shown in table 5.3:

- Case 1: $n_x = 51$, $n_t = 52$.
- Case 2: $n_x = 101$, $n_t = 122$.
- Case 3: $n_x = 301$, $n_t = 389$.

Table 5.3 suggests the similar conclusions as those from the previous simulation studies including (1) Bias, SE, MSE are relatively small compared to true values, which indicates consistency of estimators; (2) Standard errors obtained by simulation and calculated based on Theorem 19 and 21 are close to each other, which indicates convergence in variation; (3) Coverage probabilities are close to 0.95, which indicates asymptotic normality of the proposed estimators. Here although coverage probability of D_c in case 3 is only 0.906, we still can conclude that the asymptotic normality of $\hat{D}_c$ is valid based on P-value of Kolmogorov-Smirnov test, Shapiro-Wilk test, Anderson-Darling test as 0.7746, 0.8018 and 0.6627, respectively and QQ-plot (Fig 5.5(c)). From Fig 5.5(c), we claim that the difference between coverage probability of $\hat{D}_c$ and 0.95 is caused by bias and difference between theoretical value and simulated value of standard error, which might be due to overfitting issue in smoothing step.

Moreover, comparing cases where we fix $N_{X,est} = 2$ and where we choose $N_{X,est}$

Table 5.3: Simulation of parameter estimation procedure for model (5.2) with $R(x,t)$ as Fig 5.4b and different cases of sample size. SE: simulated standard error; SE* and covProb*: theoretical standard error and coverage provability obtained based on true value and Theorem 19 and 21; SE** and covProb**: theoretical standard error and coverage probability obtained based on estimated value and Theorem 19 and 21.

		k_{ac} (1)		k_{dc} (0.4)		D_c (10)	
		$N_X = 2$	CV	$N_X = 2$	CV	$N_X = 2$	CV
Case 1	bias	-0.0308	-0.0313	-0.0123	-0.0123	-0.3767	-0.2567
	SE	0.0728	0.0764	0.0314	0.0328	0.7976	0.9334
	SE*	0.0726		0.0309		0.8108	
	SE**	0.0702		0.0299		0.7865	
	MSE	0.0062	0.0068	0.0011	0.0012	0.7780	0.9372
	covProb*	0.934		0.934		0.94	
	covProb**	0.899		0.899		0.895	
Case 2	bias	-0.0083	-0.0101	0.0023	-0.0030	-0.1155	-0.0841
	SE	0.0335	0.0336	0.0140	0.0146	0.3815	0.3848
	SE*	0.0333		0.0142		0.3720	
	SE**	0.0331		0.0141		0.3703	
	MSE	0.0012	0.0012	0.0002	0.0002	0.1589	0.1551
	covProb*	0.946		0.945		0.932	
	covProb**	0.938		0.946		0.924	
Case 3	bias	-0.0048	-0.0044	-0.0011	-0.0010	-0.0782	-0.0417
	SE	0.0107	0.0108	0.0046	0.0046	0.1196	0.1246
	SE*	0.0108		0.0046		0.1201	
	SE**	0.0107		0.0046		0.1201	
	MSE	1.3681e-4	1.3663e-4	2.2134e-5	2.2119e-5	0.0204	0.0173
	covProb*	0.939		0.945		0.906	
	covProb**	0.938		0.943		0.901	

with cross validation, we concluded that (1) results of k_{ac} and k_{dc} are similar in terms of bias, SE and MSE; (2) MSE of D_c is smaller when $N_{X,est}$ is chosen with cross validation than when it is fixed at 2, which indicates choosing $N_{X,est}$ with cross validation gives better performance of estimators.

The comparison across different cases clearly shows that the performance of the proposed estimation procedure is getting better when sample size is getting larger, in terms of bias, standard error and MSE of k_{ac}, k_{dc} and D_c.

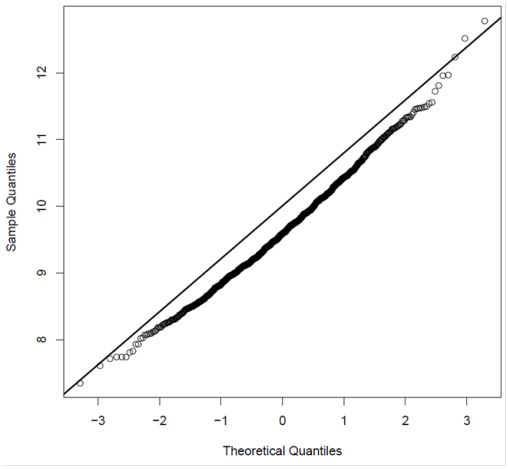

(a) QQ-plot of $\widehat{D}$ in case 1

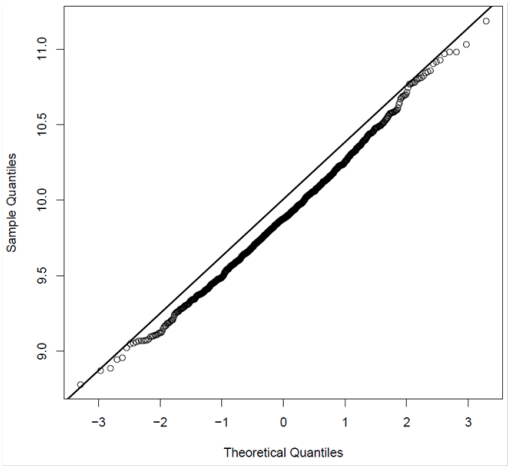

(b) QQ-plot of $\widehat{D}$ in case 2

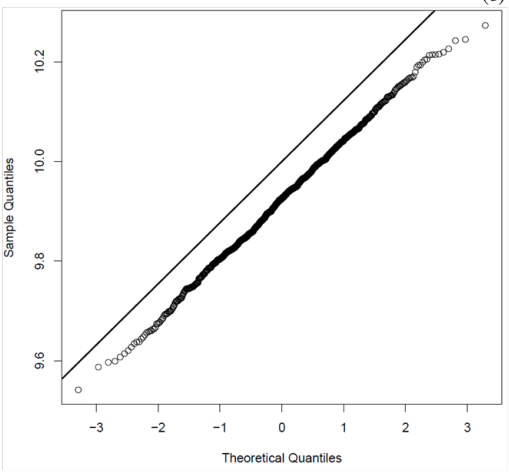

(c) QQ-plot of $\widehat{D}$ in case 3

Figure 5.5: QQ plot for normality check of $\hat{D}_c$ in three different cases.

Chapter 6

Parameter Estimation Procedure of Nonlinear Reaction Diffusion Equation

In this chapter, we will introduce a parameter estimation procedure of nonlinear reaction diffusion model defined on the bounded space Ω with boundary denoted $\partial\Omega$.

$$\begin{cases} F_t = \mathcal{F}(G(\boldsymbol{x},t), F(\boldsymbol{x},t), \boldsymbol{\theta}) + D\Delta F \quad \text{for}(\boldsymbol{x},t) \in \Omega \times [0,T] \\ \alpha_1 F(\boldsymbol{x},t) + \alpha_2 \dfrac{\partial F}{\partial \boldsymbol{n}} = 0 \quad \text{for}(\boldsymbol{x},t) \in \Omega \times [0,T] \\ F(\boldsymbol{x},0) = f_0(\boldsymbol{x}) \end{cases} \tag{6.1}$$

where $\boldsymbol{\theta}$ is a set of unknown parameters involved in reaction activities, D is unknown diffusion coefficient, $G(\boldsymbol{x},t)$ is known spatial-temporal force which affects reaction activities and can be observed, $\mathcal{F}(\cdot)$ is local reaction function depending on $F(\boldsymbol{x},t)$, $G(\boldsymbol{x},t)$, $\boldsymbol{\theta}$ and D.

In this chapter, we only consider Dirichlet condition with $\alpha_2 = 0$ and Neumann's condition with $\alpha_1 = 0$ as boundary condition.

Our proposed method is the extension of the parameter estimation procedure for linear reaction diffusion equation described in the previous chapter. In that chapter, the reason why we can avoid nonparametric estimation of the second order derivative with respect to spatial dimension, is that we can derive an ODE system (5.7) based on spectral decomposition of the solution to PDE (5.2). In fact, the coefficient functions $F_n(t)$ and $G_n(t)$ satisfying ODE system (5.7) is inner product of normalized eigenfunction of Laplacian operator and $F(\boldsymbol{x}, t)$ and $G(\boldsymbol{x}, t)$. That is to say, the ODE system (5.7) can also be considered as obtained by taking inner product of normalized eigenfunction of Laplacian operator and both side of PDE (5.2). In this chapter, motivated by this idea, we propose a parameter estimation procedure for nonlinear reaction diffusion equation. Then, we will describe implementation of the method and conduct simulation studies with different nonlinear reaction function set-ups.

6.1 Statistical Analysis

In fact, model (5.2) is a special case of model (6.1). The observation process of model (6.1) is the same as that of model (5.2). The reaction forcing factor $G(\boldsymbol{x}, t)$ and unknown dynamics $F(\boldsymbol{x}, t)$ is observed with independent Gaussian noise on deterministic time grid and location grid $\{(\boldsymbol{x}_i, t_j)\}_{i=0,j=1}^{n_x,n_t}$, i.e.

$$\begin{cases} f_{ij} = F(\boldsymbol{x}_i, t_j) + \epsilon_{ij}^{(f)} \\ g_{ij} = G(\boldsymbol{x}_i, t_j) + \epsilon_{ij}^{(g)} \end{cases} \qquad i = 0, 1, 2, \cdots, n_x \quad j = 1, 2, \cdots, n_t \tag{6.2}$$

where $\epsilon_{ij}^{(f)}, \epsilon_{ij}^{(g)}$ are observation errors satisfying $\epsilon_{ij}^{(f)} \overset{i.i.d}{\sim} N(0, \sigma_f^2)$ and $\epsilon_{ij}^{(g)} \overset{i.i.d}{\sim} N(0, \sigma_g^2)$ independently for all $i = 0, 1, 2, \cdots, n_x$ and $j = 1, 2, \cdots, n_t$. With observations of f_{ij} and g_{ij}, we want to estimate unknown reaction parameter $\boldsymbol{\theta}$ and diffusion rate D based on model (6.1).

6.1.1 Motivation

Inspired by parameter estimation procedure of linear reaction diffusion equation described in the previous chapter, the proposed procedure is also built upon the gradient matching approach on an ODE system obtained by inner product of normalized eigenfunction $\{\varphi_n(\boldsymbol{x})\}_{n=0}^{\infty}$ of Laplacian operator and both sides of PDE (6.1). For instance, in the case of Neumann's condition on Ω, we can obtain

$$\dot{F}_0(t) = \int_\Omega \mathcal{F}(G(\boldsymbol{x}, t), F(\boldsymbol{x}, t), \boldsymbol{\theta})\varphi_0(\boldsymbol{x})d\boldsymbol{x} \triangleq \mathcal{F}_0(\boldsymbol{\theta}, t) \tag{6.3}$$

$$\dot{F}_n(t) = \int_\Omega \mathcal{F}(G(\boldsymbol{x}, t), F(\boldsymbol{x}, t), \boldsymbol{\theta})\varphi_n(\boldsymbol{x})d\boldsymbol{x} - D\lambda_n F_n(t) \triangleq \mathcal{F}_n(\boldsymbol{\theta}, t) - D\lambda_n F_n(t) \quad n = 1, 2, \cdots \tag{6.4}$$

For the Dirichlet conditions, the set of ODEs starts from $n = 1$.

6.1.2 Parameter Estimation Procedure

Parameter estimators are obtained based on ODEs (6.3) and (6.4), which requires to evaluate each term on both sides of ODEs. First, $\dot{F}_n(t)$ and $F_n(t)$ in the left and right

hand sides of the model can be obtained easily with the same method described in step 1 and step 2 in section 5.2.3. However, it takes more effort to obtain $\mathcal{F}_n(\boldsymbol{\theta}, t)$. First of all, for most of nonlinear function $\mathcal{F}(\cdot)$, it is difficult to calculate explicit formula for $\int_\Omega \mathcal{F}(\cdot)\varphi_n(\boldsymbol{x})d\boldsymbol{x}$. Moreover, we don't know analytically the formulas for $G(\boldsymbol{x}, t)$ and $F(\boldsymbol{x}, t)$. Instead we can only observe $G(\boldsymbol{x}, t)$ and $F(\boldsymbol{x}, t)$ with uncertainty. On the other hand, the two problems can be solved by approximating integral with Right Riemann Summation and estimating $G(\boldsymbol{x}, t)$ and $F(\boldsymbol{x}, t)$ by smoothing data. Therefore, the term $\mathcal{F}_n(\boldsymbol{\theta}, t)$ on the right hand side of the equation can be obtained by plugging smoothed data $\tilde{F}(\boldsymbol{x}, t)$ and $\tilde{G}(\boldsymbol{x}, t)$ in Right Riemann Summation as

$$\hat{\mathcal{F}}_n(\boldsymbol{\theta}, t) = \Delta x \sum_{i=1}^{n_x} \mathcal{F}\left(\tilde{G}(\boldsymbol{x}_i, t), \tilde{F}(\boldsymbol{x}_i, t), \boldsymbol{\theta}\right) \varphi_n(\boldsymbol{x}_i) \quad n = 0, 1, 2, \cdots \tag{6.5}$$

Moreover, since model (6.3) only involves $\boldsymbol{\theta}$, we can use (6.3) to estimate $\boldsymbol{\theta}$ with nonlinear least square method. Then we plug estimator $\hat{\boldsymbol{\theta}}$ in equation (6.4) to get least square estimator of D. Therefore, proposed parameter estimation procedure can be summarized as follow:

Step 1: Obtaining smoothed function $\hat{F}_n(t)$ and $\hat{\dot{F}}_n(t)$ with exactly the same procedure as step 1 and step 2 in section 5.2.3.

Step 2: Approximating integration of $\mathcal{F}_n(\boldsymbol{\theta}, t)$ for $n = 0, 1, 2, \cdots$ with Right Riemann Summation as equation (6.5), where $F(\boldsymbol{x}, t)$ and $G(\boldsymbol{x}, t)$ can be smoothed by any smoothing technique, such as local polynomial, smoothing with spline, kernel smoothing, etc. In this dissertation, $F(\boldsymbol{x}, t)$ and $G(\boldsymbol{x}, t)$ is smoothed by the same technique as described in section 5.5.1.

Step 3: Estimating $\boldsymbol{\theta}$ by minimizing $\mathbb{L}_2$ norm of difference between left hand side and right hand side of model (6.3), i.e.

$$\hat{\boldsymbol{\theta}} = \underset{\boldsymbol{\theta}}{\operatorname{argmin}}\, S_{\boldsymbol{\theta}}(\boldsymbol{\theta}) = \underset{\boldsymbol{\theta}}{\operatorname{argmin}} \int_0^T \left(\dot{\hat{F}}_0(t) - \mathcal{F}_0(\boldsymbol{\theta}, t)\right)^2 dt$$

Then we plug in estimator $\hat{\boldsymbol{\theta}}$ in model (6.4). Suppose we consider first $N_{X,est}$ equations, D is obtained by minimizing

$$S_D(D) = \sum_{n=1}^{N_{X,est}} \int_0^T \left(\dot{\hat{F}}_n(t) - \mathcal{F}_n(\hat{\boldsymbol{\theta}}, t) + D\lambda_n \hat{F}_n(t)\right)^2$$

In practice, we minimize the following mean squared error instead of $S_{\boldsymbol{\theta}}(\boldsymbol{\theta})$ and $S_D(D)$:

$$\hat{S}_{\boldsymbol{\theta}}(\boldsymbol{\theta}) = \frac{1}{n_t} \sum_{j=1}^{n_t} \left(\dot{\hat{F}}_0(t_j) - \hat{\mathcal{F}}_0(\boldsymbol{\theta}, t_j)\right)^2$$

and

$$\hat{S}_D(D) = \frac{1}{n_t} \sum_{n=1}^{N_{X,est}} \sum_{j=1}^{n_t} \left(\dot{\hat{F}}_n(t_j) - \hat{\mathcal{F}}_n(\hat{\boldsymbol{\theta}}, t_j) + D\lambda_n \hat{F}_n(t_j)\right)^2$$

It is also worth pointing out that if $\mathcal{F}(\cdot)$ is linear function as $\mathcal{F}(F(\boldsymbol{x}, t), G(\boldsymbol{x}, t), \boldsymbol{\theta}) = \theta_1 G(\boldsymbol{x}, t) + \theta_2 F(\boldsymbol{x}, t)$, then $\mathcal{F}_n(\boldsymbol{\theta}, t) = \theta_1 G_n(t) + \theta_2 F_n(t)$, which means that the proposed method would degenerate to the parameter estimation procedure of linear reaction diffusion equation provided in section 5.2.3.

6.2 Implementation and Simulation Study

Similar as the parameter estimation procedure in section 5.2.3, $N_{X,est}$, the number of equations used to estimate diffusion coefficient D can be fixed, which means that it is not necessary to have $N_{X,est} \to \infty$ when sample size gets larger. On the other hand, the number of basis functions in smoothing step, $N_{T,est}$ should be chosen carefully. In practice,

we choose $N_{T,est}$, $N_{X,est}$, $N_{T,smooth}$, $N_{X,smooth}$ with cross validation, which is similar as described in section 5.5.1 and 5.5.2. Thus, we implement the proposed method in the following order: (1) smoothing data $f(\boldsymbol{x}_i, t_j)$ and $g(\boldsymbol{x}_i, t_j)$ with the procedure described in section 5.5.1; (2) obtaining pseudo data $\tilde{F}_n(t)$ as described in the step 1 in section 5.2.3; (3) smoothing pseudo data $\tilde{F}_n(t)$ and obtaining first derivative of $\tilde{F}_n(t)$ as described in step 2 in section 5.2.3. As for the choice of $N_{T,est}$, GCV method is used in the way described in section 5.5.2; (4) obtaining $\hat{\mathcal{F}}(\boldsymbol{\theta}, t)$ based on equation (6.5); (5) estimating $\boldsymbol{\theta}$ with $\hat{F}_0(t)$, $\hat{\dot{F}}_0(t)$ and $\hat{\mathcal{F}}(\boldsymbol{\theta}, t)$; (6) choosing $N_{X,est}$ with 10-fold cross validation with similar procedure as described in 5.5.2; (7) estimating D with first $N_{X,est}$ equations of (6.4).

In this section, simulation studies are conducted with different nonlinear reaction function $\mathcal{F}(\cdot)$ and set-up of $G(\boldsymbol{x}, t)$ and true parameters. All the estimation procedures were implemented in R. We first choose an arbitrary nonlinear reaction function $\mathcal{F}(\cdot)$, which can generate some interesting spatial-temporal pattern. In addition, we use our pollen tube tip growth setting for simulation. For each set-up, we conduct simulation study with $N_{X,est}$ and $N_{T,est}$ chosen from $1, 2, \cdots, 10$.

6.2.1 Simulation with arbitrary nonlinear reaction function $\mathcal{F}(\cdot)$

In this set-up, we apply our proposed method on nonlinear reaction-diffusion model as

$$\begin{cases} F_t = \theta_1 F(x,t) + \theta_2 F(x,t)^2 G(x,t) + D F_{xx} \quad (x,t) \in [0,1] \times [0,T] \\ F_x(0,t) = F_x(1,t) = 0 \quad t \in [0,T] \end{cases} \tag{6.6}$$

with $\theta_1 = 0.5$, $\theta_2 = -0.2$, $D = 0.3$ and $G(x,t)$ defined as a periodic function with single-peak spatial pattern (See Fig 6.1b) as

$$G(x,t) = (\sin(2\pi t/5) + 1) * (e^{-(x-0.5)^2/0.02}) + 1.$$

With initial value as $F(x, t = 0) = F(x, t = 0) = e^{-\frac{(x-0.5)^2}{0.05}}$, we can solve PDE (6.6) to get true value of solution $F(x,t)$ (See Fig 6.1a).

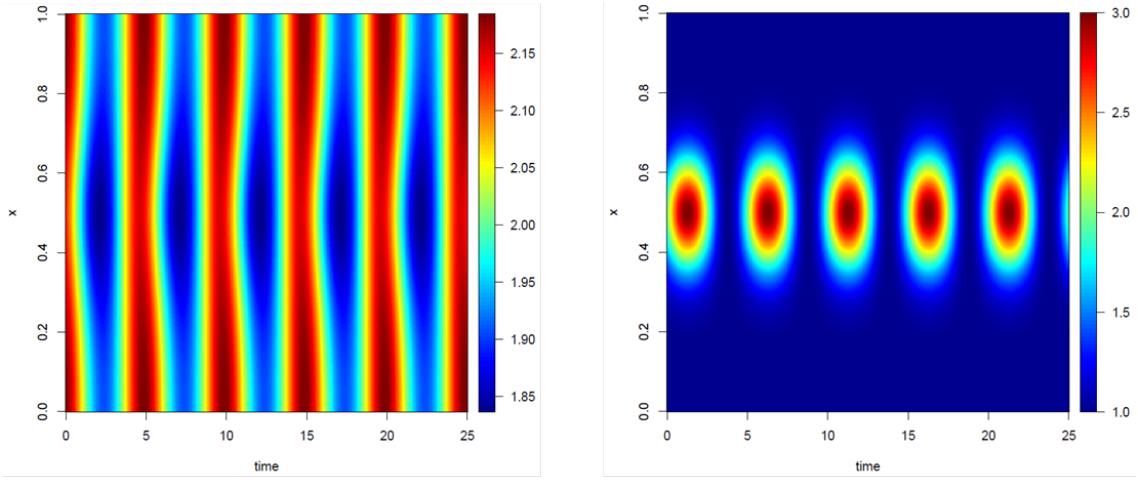

(a) True value of F(x,t)

(b) True value of G(x,t)

Figure 6.1: Spatial-temporal pattern of $F(x,t)$ and $G(x,t)$ in set-up 1 of nonlinear reaction diffusion model

As shown in Fig 6.1, at each time point, the range of $F(x,t)$ and $G(x,t)$ are around 0.1 and 2, respectively, so we choose noise of $F(x,t)$ and $G(x,t)$ as $\sigma_f = 0.05$ and $\sigma_g = 1$. We simulate data from $t \in [0, 25]$. As for sample size, we choose $n_t = 251$ and $n_x = 101$. The simulation was repeated for 1000 times. The results are shown in table 6.1.

In table 6.1, the true value of each parameter is shown in the parentheses. Compared with true value of each parameter, bias, SE and MSE are relatively small, which indicates consistency of the proposed estimators.

Table 6.1: Simulation of parameter estimation procedure for model (6.6).

	$\theta_1(0.5)$	θ_2 (-0.2)	D (0.3)
bias	-0.0032	0.0016	-0.0047
SE	0.0197	0.0078	0.0155
MSE	3.9789e-4	6.3247e-5	2.6275e-4

6.2.2 Simulation with pollen tube tip growth model

In this section, we apply our proposed method on R_t equation of our pollen tube model (2.15). We use the same parameter setting as in (5.42) and true value of $F(x,t)$ and $G(x,t)$ as solution to $R(x,t)$ and $C(x,t)$ shown in Fig 5.4, respectively. Specifically, we are working on the following nonlinear reaction diffusion model

$$\begin{cases} R_t = k_{pf} R(x,t)^{1.5}(5\pi - \int_{-2.5\pi}^{2.5\pi} R(x,t)dx) - k_{nf} R(x,t)\dfrac{C(x,t)^2}{C(x,t)^2 + k_c 3^2} + D_r R_{xx} \\ R_x(2.5\pi,t) = R_x(-2.5\pi,t) = 0 \quad t \in [0,T] \end{cases} \tag{6.7}$$

with $(x,t) \in [-2.5\pi, 2.5\pi] \times [0,T]$, true value of parameters as $k_{pf} = 0.229$, $k_{nf} = 3.6$, $k_c = 0.15$, $D_r = 0.1$, true value of $C(x,t)$ and $R(x,t)$ as shown in Fig 5.4a and b. Based on range of $R(x,t)$ and $C(x,t)$, we set noise of $R(x,t)$ and $C(x,t)$ as $\sigma_r = 0.05$ and $\sigma_c = 0.01$. We simulated data from $t \in [0, 97.2]$, which included 9 entire periods of oscillation. We conducted simulation studies with different sample sizes, and repeat each simulation 1000 times. The results are summarized in table 6.2:

- Case 1: $n_x = 51$, $n_t = 52$.
- Case 2: $n_x = 101$, $n_t = 122$.
- Case 3: $n_x = 301$, $n_t = 389$.

Table 6.2: Simulation of parameter estimation procedure for model (6.7) with different cases of sample size.

		$k_{pf}(0.229)$	k_{nf} (3.6)	k_c (0.15)	D_r (0.1)
Case 1	bias	0.0033	0.6122	0.0056	-0.0075
	SE	0.0521	4.5248	0.0909	0.0468
	MSE	0.0027	20.8486	0.0083	0.0022
Case 2	bias	0.0108	-0.1390	-0.0105	0.0063
	SE	0.0200	0.2858	0.0150	0.0189
	MSE	5.1614e-4	0.1010	3.3479e-4	3.9601e-4
Case 3	bias	0.0079	-0.1379	-0.0086	0.0058
	SE	0.0068	0.0955	0.0053	0.0058
	MSE	1.0829e-4	0.0281	1.0213e-4	6.6821e-5

Based on the table 6.2, we can draw similar conclusion as those from previous simulation studies: bias, SE and MSE are relatively small compared with true value of each parameter, which indicates consistency of the proposed estimator. The comparison across different cases clearly shows that the performance of the proposed estimation procedure is getting better when sample size is getting larger because MSE of k_{pf}, k_{nf}, k_c and D_c are getting smaller.

Chapter 7

Real Data Study: Cell Polarity Growth

The real data of ROP1 and Ca^{2+} concentration, $R(x,t)$ and $C(x,t)$ were collected from Arabidopsis pollen tubes from one of its oblique planes at position every $0.1161\mu m$ from -5.3574μm to $5.3574\mu m$ at every $0.67s$ from 0 to $69.68s$. Each data point consists of four items, the position x, time t, the associated observed ROP1 and Ca^{2+} concentration $R(x,t)$ and $C(x,t)$. As shown in Fig 7.1, both $R(x,t)$ and $C(x,t)$ concentration have a oscillatory temporal pattern with $5.7s$ period and double-peak spatial pattern with peaks on shoulders of the plasma membrane.

In this chapter, we first fit the model (2.15) with observed data to estimate unknown parameters listed in table 7.1. The values for α and R_{tot} used here are suggested by the biologist as 1.5 and 12 based on empirical studies, respectively. Then we refine the model guided by prediction of Ca^{2+} and ROP1 concentration along membrane obtained by

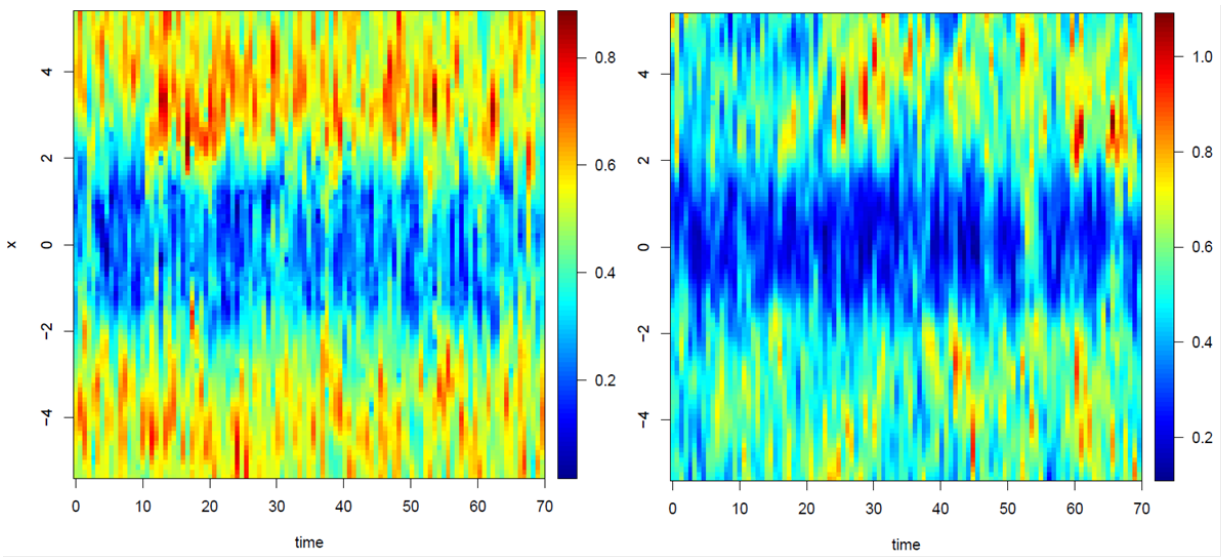

(a) Observed ROP1 Concentration on Membrane (b) Observed Ca^{2+} Concentration on Membrane

Figure 7.1: Spatial-temporal pattern of Observed $R(x,t)$ and $C(x,t)$

plugging back estimators to model (2.15).

Table 7.1: Unknown parameters in model (2.15)

Unknown parameter	Interpretation
k_{pf}	ROP1 positive feedback rate
k_{nf}	ROP1 negative feedback rate
k_c	Threshold of Ca^{2+} inhibition effect on ROP1 activity
k_{ac}	Ca^{2+} influx rate
k_{dc}	Ca^{2+} efflux rate
D_r, D_c	ROP1 and Ca^{2+} diffusion coefficient

7.1 Application of the Proposed Method on Pollen Tube Model

Although there are interaction effect between $R(x,t)$ and $C(x,t)$, parameters are independent between the two equations with $\{k_{pf}, k_{nf}, k_c, D_r\}$ only involved in R_t equation and $\{k_{ac}, k_{dc}, D_c\}$ only involved in C_t equation. Therefore, we can separately estimate $\{k_{pf}, k_{nf}, k_c, D_r\}$ with R_t equation as

$$\begin{cases} R_t = k_{pf} R(x,t)^{\alpha} (R_{tot} - \int_{-L}^{L} R(x,t)dx) - k_{nf} R(x,t) \dfrac{C(x,t)^2}{C(x,t)^2 + k_c^2} + D_r R_{xx} \\ R_x(L,t) = R_x(-L,t) = 0 \quad t \in [0,T] \end{cases} \tag{7.1}$$

and $\{k_{ac}, k_{dc}, D_c\}$ with C_t equation as

$$\begin{cases} C_t = k_{ac} R(x,t) - k_{dc} C(x,t) + D_c C_{xx} \quad (x,t) \in [-L,L] \times [0,T] \\ C_x(L,t) = C_x(-L,t) = 0 \quad t \in [0,T] \end{cases} \tag{7.2}$$

Notice that model (7.2) is a linear reaction diffusion equation, which can be fitted by the proposed method in chapter 5. And model (7.1) is a nonlinear equation, which can be fitted by extended method in chapter 6. Based on implementation of both methods described in the corresponding chapters, no matter which method we are using, the first step is to smooth $R(x,t)$ and $C(x,t)$.

Based on biological understanding, ROP1 and Ca^{2+} concentration, $R(x,t)$ and $C(x,t)$ are symmetric around $x = 0$. In this case, normalized eigenfunction of Laplacian operator is defined as

$$\varphi_n(x) = \begin{cases} \dfrac{1}{\sqrt{2L}} & n = 0 \\ \dfrac{\cos(n\pi x/L)}{\sqrt{L}} & n = 1, 2, \cdots \end{cases} \tag{7.3}$$

with eigenvalue $\lambda_n = (n\pi/L)^2$. For the basis functions used in smoothing across temporal axis, we choose Fourier basis functions as $\{1, \sin(2m\pi T/T_0), \cos(2m\pi T/T_0)\}_{m=1}^{\infty}$, where T_0 is period of oscillation, $5.7s$. For the number of basis functions, $R(x,t)$ is smoothed with $N_{X,smooth} = 2$, $N_{T,smooth} = 10$, and $C(X,t)$ with $N_{X,smooth} = 4$, $N_{T,smooth} = 10$, which are chosen with cross validation. Thus, we can get smoothed $R(x,t)$ and $C(x,t)$ shown in Fig 7.2.

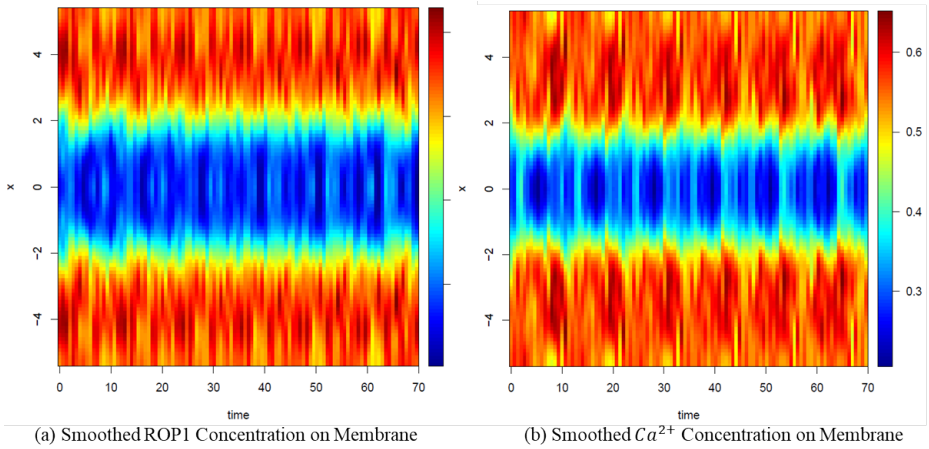

(a) Smoothed ROP1 Concentration on Membrane (b) Smoothed Ca^{2+} Concentration on Membrane

Figure 7.2: Spatial-temporal pattern of Smoothed $R(x,t)$ and $C(x,t)$

With smoothed data, we first applied the proposed method on C_t equation of model (2.15), and obtained the parameter estimators as

$$\hat{k}_{ac} = 1.28 \qquad \hat{k}_{dc} = 1.18 \qquad \hat{D}_c = -0.05 \tag{7.4}$$

with the number of ODEs used to estimate D_c, $N_{X,est} = 6$ chosen by cross validation.

Then we implemented the proposed method on R_t equation of model (2.15), and obtained the parameter estimators as

$$\hat{k}_{pf} = 0.0212 \qquad \hat{k}_{nf} = 1.0635 \qquad \hat{k}_c = 1.5680 \qquad \hat{D}_r = -0.0939 \tag{7.5}$$

with the number of ODEs used to estimate D_r, $N_{X,est} = 2$ chosen by cross validation.

7.2 Model Modification

Results in previous section show that estimators of diffusion rate D_r and D_c are both negative, which is unreasonable. One possible explanation for unreasonable parameter estimation is misspecification of our model (2.15). First of all, C_t equation in model (2.15) can be misspecified because it is established based on our limited understanding of Ca^{2+} activity in pollen tube. On the other hand, in R_t equation, we modeled inhibition effect of Ca^{2+} on ROP1 regulation based on the hypothesis that Ca^{2+} signaling might down-regulate ROP1 activity by activating negative regulators of ROP1. However, Yan [40] pointed out that there might be an alternative hypothesis that Ca^{2+} promotes the disassembly of the down-regulation of ROP1 activity by countering its F-actin-mediated positive feedback. The reason why we choose to express Ca^{2+} down-regulation effect of ROP1 activity by activating negative regulators of ROP1 is that experiments show that majority of Ca^{2+} inhibition effects involves in negative feedback of ROP1. Therefore, both Ca^{2+} and ROP1 equations might be misspecified in our case. In this section, we intend to give some guides on refining our model based on current results.

First, we look at Ca^{2+} model,

$$\begin{cases} C_t = k_{ac}R(x,t) - k_{dc}C(x,t) + D_cC_{xx} \quad (x,t) \in [-L,L] \times [0,T] \\ C_x(L,t) = C_x(-L,t) = 0 \quad t \in [0,T] \end{cases} \tag{7.6}$$

which includes influx of Ca^{2+} regulated by ROP1 concentration, efflux of Ca^{2+}, and diffusion of Ca^{2+} along the membrane. In fact, influx of Ca^{2+} depends not only on activation

effect of ROP1 on Ca^{2+} channel but also on influx base level. Moreover, the proposed model does not include the pumping back and small leak effect of endoplasmic reticulum (ER) observed by Yang's group. Therefore, we denote k_b as difference between base level effect of influx and ER effect. Notice that base level effect of influx is involved in positive feedback of Ca^{2+} and ER effect acts as negative feedback of Ca^{2+}. So k_b can be either positive or negative. Thus, we proposed a refined model of Ca^{2+} as

$$\begin{cases} C_t = k_b + k_{ac}R(x,t) - k_{dc}C(x,t) + D_cC_{xx} \quad (x,t) \in [-L,L] \times [0,T] \\ C_x(L,t) = C_x(-L,t) = 0 \quad t \in [0,T] \end{cases} \tag{7.7}$$

Applying the proposed parameter estimation procedure on model (7.7) with data, we obtain parameter estimator as

$$\hat{k}_b = -0.8220 \qquad \hat{k}_{ac} = 4.2540 \qquad \hat{k}_{dc} = 2.2381 \qquad \hat{D}_c = 1.7567 \tag{7.8}$$

In order to test whether the parameter estimator is reasonable for model (7.7), we plug in smoothed data $R(x,t)$ (see Fig 7.2a) and parameter estimation into model (7.7) and solve for $C(x,t)$ to check whether it can generate observed spatial-temporal pattern as $C(x,t)$ (see Fig 7.2b). With $R(x,t)$ as Fig 7.2a and estimator in (7.8), we obtain prediction of $C(x,t)$ as Fig 7.3. Comparing spatial-temporal pattern of predicted $C(x,t)$ (Fig 7.3) with smoothed data $C(x,t)$ (Fig 7.2b) and observed data (Fig 7.1b), we can claim that our refined model (7.7) is a good candidate for potential equation to describe Ca^{2+} activity near plasma membrane. Here, though we use a constant k_b to represent base level effect of influx and ER effect, it only shows lack of an additional term that does not depend on ROP1 and Ca^{2+} on the plasma membrane. We know that base level of C^{2+} influx is usually

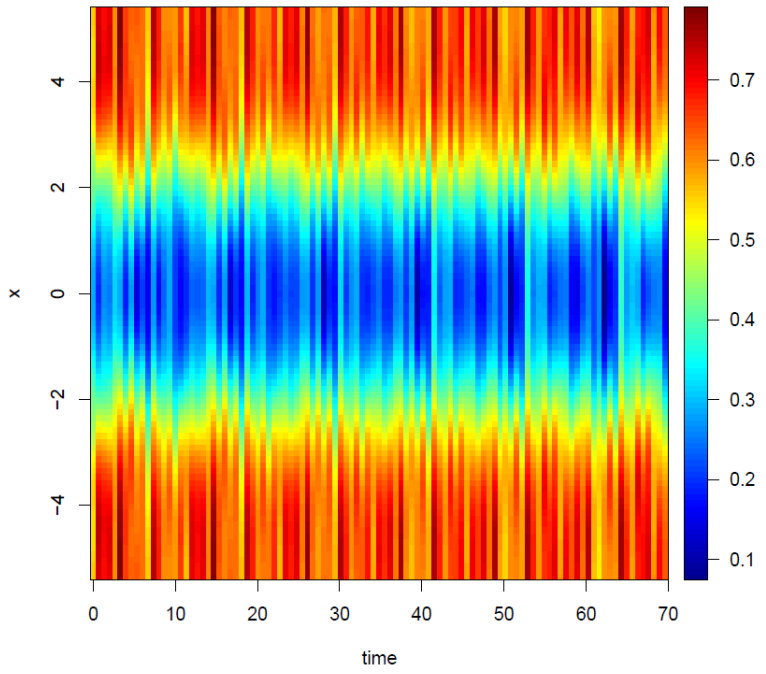

Figure 7.3: Spatial-temporal Pattern of Predicted $C(x,t)$ based on model (7.7) with $R(x,t)$ as Fig 7.2a and estimator in (7.8)

a constant, and that ER effect depends on cytosolic Ca^{2+}. Since estimator of k_b is -0.8820, which is negative, we suggest that the model can be refined by including ER effect.

As for ROP1 equation in model (2.15), there are more modification that can be made on the equation, such as Ca^{2+}down-regulation for ROP1 activity. Moreover, R_{tot}, which is immeasurable but critical from both biological and computational view, is confounded with positive feedback of ROP1. In addition, how we include R_{tot} in R_t equation is also doubtful. Therefore, more biological input is required to further modify the R_t equation in model (2.15).

Chapter 8

Conclusions

Reaction diffusion equation has been widely used in modeling dynamic processes in physics, chemistry, biology, engineering, and so forth. In this dissertation, a new reaction diffusion equation is introduced to describe ROP1 and Ca^{2+} regulation system in pollen tube tip growth, which incorporates positive and negative feedback of ROP1, influx and efflux of Ca^{2+} and lateral diffusive movement of ROP1 and Ca^{2+}. Mathematical analysis and numerical simulation of the system were carried out at several levels: (1) the non-spatial model without diffusion and non-local term; (2) the spatial-temporal model with diffusion and nonlocal effect. The existence of parameter ranges supporting spatially non-homogeneous time-periodic solutions is revealed from mathematical analysis and numerical simulation.

In order to investigate quantitative comparison of numerical simulated solutions and experimental data, model validation using experimental data as well as fine tuning of the proposed reaction diffusion model, we introduce a parameter estimation procedure

which incorporates gradient matching procedure and characters of reaction diffusion equation, and decomposes the solution with eigenfunction of Laplacian operator. The advantage of incorporating the decomposition of the solution is to avoid nonparamteric estimation of high order derivative, which can benefit parameter estimation performance in high dimensional reaction diffusion equation. Simulation studies show the consistency and asymptotic normality of the proposed estimators in both linear and nonlinear reaction diffusion equations with different examples of the model and the pollen tube model. Moreover, theoretical proof of large sample behavior in linear reaction diffusion equation case has been provided in this dissertation. On the other hand, more work is required for the proof of nonlinear reaction diffusion equation, which can be an extension of linear case with linearization of nonlinear reaction function by Taylor expansion.

The proposed parameter estimation method has been implemented on pollen tube model with experimental observation of Arbidopsis pollen tube from Yang's group to estimate feedback rates and diffusion rates. Based on our pollen tube model, negative diffusion rates are obtained with the proposed parameter estimation method, which is possibly caused by misspecification of the reaction diffusion model. With more study of the model and parameter estimation, we manage to give suggestion on modifying Ca^{2+} activity equation with an additional negative feedback term representing ER effect which depends on cytosolic Ca^{2+}. However, more investigation is needed to refine ROP1 activity model. Besides the set of data used in parameter estimation with spatial temporal pattern which can be generated by the proposed reaction diffusion equation, another set of data is observed on a different tube with spatial temporal pattern shown in Fig 8.1. Once we smooth the data to

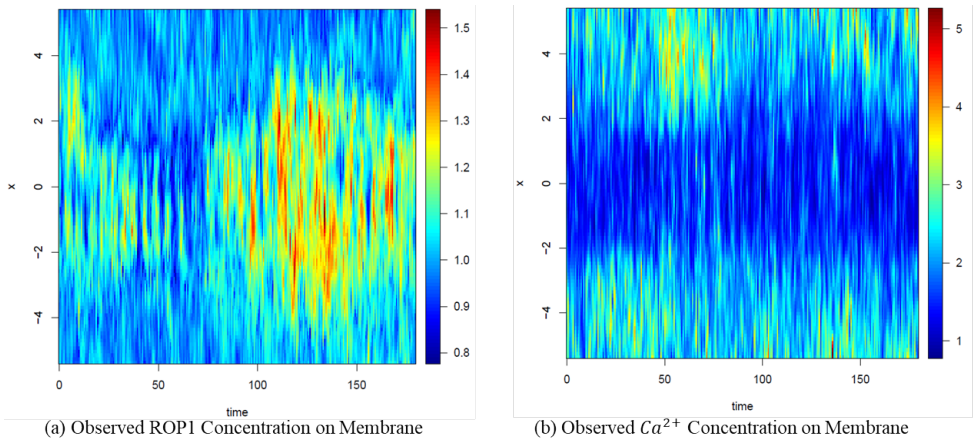

(a) Observed ROP1 Concentration on Membrane (b) Observed Ca^{2+} Concentration on Membrane

Figure 8.1: Special Spatial-temporal pattern of Observed $R(x,t)$ and $C(x,t)$.

reduce the noise, we can observe a clearer spatial-temporal pattern as Fig 8.2, which shows a single-peak spatial pattern of ROP1 concentration and a double-peak spatial pattern of Ca^{2+} concentration on plasma membrane. On the other hand, our model is only capable to recover $R(x,t)$ and $C(x,t)$ with the same spatial temporal pattern. Therefore, developing a model to generate different observed spatial-temporal patterns will be our future work.

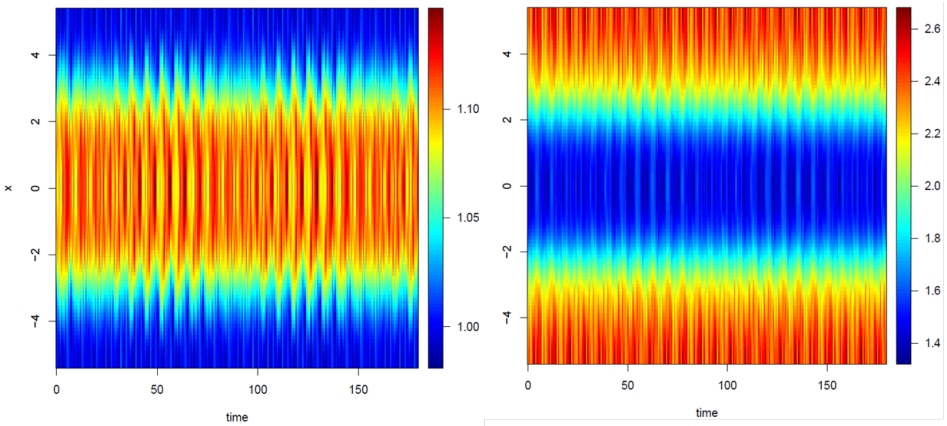

(a) Smoothed ROP1 Concentration on Membrane (b) Smoothed Ca^{2+} Concentration on Membrane

Figure 8.2: Special Spatial-temporal pattern of Smoothed $R(x,t)$ and $C(x,t)$.

Bibliography

[1] S. J. Altschuler, S. B. Angenent, Y. Wang, and L. F. Wu. On the spontaneous emergence of cell polarity. *Nature*, 454(7206):886–889, 2008.

[2] Markus Bar, Rainer Hegger, and Holger Kantz. Fitting partial differential equations to space-time dynamics. *Phys. Rev. E*, 59:337–342, Jan 1999.

[3] Scott M Berry, Raymond J Carroll, and David Ruppert. Bayesian smoothing and regression splines for measurement error problems. *Journal of the American Statistical Association*, 97(457):160–169, 2002.

[4] Nicolas J-B. Brunel. Parameter estimation of odes via nonparametric estimators. *Electron. J. Statist.*, 2:1242–1267, 2008.

[5] C.-S. Chou, Q. Nie, and T.-M. Yi. Modeling robustness tradeoffs in yeast cell polarization induced by spatial gradients. *PloS One*, 3(9):e3103, 2008.

[6] G. W. De Young and J. Keizer. A single pool inositol 1,4,5 trisphosphate receptor based model for agonist stimulated oscillations in ca2+ concentration. *Proceedings of the National Academy of Sciences of the United States of America*, 89(20):98959899, 1992.

[7] S. N. Ethier and T. G. Kurtz. *Markov Process: Charaterization and Convergence.* Wiley, New York, 1986.

[8] Jianqing Fan and Irene Gijbels. *Local Polynomial Modelling and Its Applications*, volume 66 of *Monographs on Statistics and Applied Probability*. Chapman and Hall/CRC, 1996.

[9] William Feller. *An introduction to probability theory and its applications.* John Wiley & sons, New York, third edition, 1957.

[10] S. Feng. *The Poisson-Dirichlet Distribution and Related Topics: Models and Asymptotic Behaviors.* Springer, Heidelberg, 2010.

[11] A. Goldbeter, G. Dupont, and MJ. Berridge. Minimal model for signal-induced Ca^{2+} oscillations and for their frequency encoding through protein phosphorylation. *Proceedings of the National Academy of Sciences of the United States of America.*, 87(4):1461–1465, 1990.

[12] Y. Gu, Y. Fu, P. Dowd, S.-D. Li, V. Vernoud, S. Gilroy, and Z.-B. Yang. A Rho family gtpase controls actin dynamics and tip growth via two counteracting downstream pathways in pollen tubes. *Jour. Cell Biol.*, 169(1):127–138, 2005.

[13] Ankit Gupta. Stochastic model for cell polarity. *The anals of applied probability*, 22(2):827–859, 2012.

[14] Jung Min Han, Akihiko Tanimura, Vivien Kirk, and James Sneyd. A mathematical model of calcium dynamics in hsy cells. *PLOS Computational Biology*, 13(2):1–29, 02 2017.

[15] J.-U. Hwang, Y.-J. Lee Y. Gu, and Z.-B. Yang. Oscillatory ROP GTPase activation leads the oscillatory polarized growth of pollen tubes. *Mole. Biol. Cell*, 16(11):5385–5399, 2005.

[16] H. Li, Y.-K. Lin, R. M. Heath, M. X. Zhu, and Z.-B. Yang. Control of pollen tube tip growth by a ROP GTPase-dependent pathway that leads to tip-localized calcium influx. *Plant Cell*, 11(9):1731–1742, 1999.

[17] X. Li, H. Wang, Z. Zhang, and A. Hastings. Mathematical analysis of coral reef models. *J. Math. Anal. Appl.*, 416(1):352–373, 2014.

[18] Hua Liang and Hulin Wu. Parameter estimation for differential equation models using a framework of measurement error in regression models. *Journal of the American Statistical Association*, 103(484):1570–1583, 2008.

[19] W.-C. Lo, H.-O. Park, and C.-S. Chou. Mathematical analysis of spontaneous emergence of cell polarity. *Bull. Math. Biol.*, 76(8):1835–1865, 2014.

[20] D. Ludwig, D. D. Jones, and C. S. Holling. Qualitative analysis of insect outbreak systems: the spruce budworm and forest. *J. Anim. Ecol.*, 47(1):315–332, 1978.

[21] A. Mckenzie and J. Sneyd. On the formation and breakup of spiral waves of calcium. *International Journal of Bifurcation and Chaos*, 8(10):2003–2012, 1998.

[22] T. I. Moore, C.-S. Chou, Q. Nie, N. L. Jeon, and T.-M. Yi. Robust spatial sensing of mating pheromone gradients by yeast cells. *PloS one*, 3(12):e3865, 2008.

[23] P. J. Mumby, A. Hastings, and H. J. Edwards. Thresholds and the resilience of Caribbean coral reefs. *Nature*, 450(7166):98–101, 2007.

[24] Whitney K. Newey and Thomas M. Stoker. Efficiency of weighted average derivative estimators and index models. *Econometrica*, 61(5):1199–1223, 1993.

[25] L. Perko. *Differential equations and dynamical systems*, volume 7 of *Texts in Applied Mathematics*. Springer-Verlag, New York, third edition, 2001.

[26] Y. Qin and Z.-B. Yang. Rapid tip growth: insights from pollen tubes. *Semi. Cell & Deve. Biol.*, 22:816–824, 2011.

[27] James Ramsay and Giles Hooker. *Dynamic Data Analysis : Modeling Data with Differential Equations.* Springer, New York, NY, 2017.

[28] Feng Rao, Carlos Castillo-Chavez, and Yun Kang. Dynamics of a diffusion reaction prey-predator model with delay in prey: Effects of delay and spatial components. *Journal of Mathematical Analysis and Applications*, 461(2):1177 – 1214, 2018.

[29] M. Scheffer, S. Carpenter, J. A. Foley, C. Folke, and B. Walker. Catastrophic shifts in ecosystems. *Nature*, 413(6856):591–596, 2001.

[30] M. Scheffer, S. H. Hosper, M. L. Meijer, B. Moss, and E. Jeppesen. Alternative equilibria in shallow lakes. *Trends Ecol. Evol.*, 8(8):275–279, 1993.

[31] Gieri Simonett. Center manifolds for quasilinear reaction-diffusion systems. *Differential Integral Equations*, 8(4):753–796, 1995.

[32] J. Sneyd, BT. Wetton, AC. Charles, and MJ. Sanderson. Intercellular calcium waves mediated by diffusion of inositol trisphosphate: a two-dimensional model. *Am J Physiol*, 268(6):C1537–C1545, 1995.

[33] A. C. Staver, S. Archibald, and S. A. Levin. The global extent and determinants of savanna and forest as alternative biome states. *Science*, 334(6053):230–232, 2011.

[34] A. C. Staver, S. Archibald, and S. A. Levin. Tree cover in sub-Saharan Africa: rainfall and fire constrain forest and savanna as alternative stable states. *Ecology*, 92(5):1063–1072, 2011.

[35] Sabrina Stella, Roberto Chignola, and Edoardo Milotti. Competing computational approaches to reaction-diffusion equations in clusters of cells, 2014.

[36] A. M. Turing. The chemical basis of morphogenesis. *Philos. Trans. Roy. Soc. London Ser. B*, 237(641):37–72, 1952.

[37] J.-F. Wang, J.-P. Shi, and J.-J. Wei. Dynamics and pattern formation in a diffusive predator-prey system with strong Allee effect in prey. *J. Differential Equations*, 251(4-5):1276–1304, 2011.

[38] Z. Xiao, N. Brunel, Z.-B. Yang, and X.-P. Cui. Constrained nonlinear and mixed effects of differential equation models for dynamic cell polarity signaling. *arXiv: 1605.00185*, 2016.

[39] Xiaolei Xun, Jiguo Cao, Bani Mallick, Arnab Maity, and Raymond J. Carroll. Parameter estimation of partial differential equation models. *Journal of the American Statistical Association*, 108(503):1009–1020, 2013.

[40] A. Yan, G.-S. Xu, and Z.-B. Yang. Calcium participates in feedback regulation of the oscillating ROP1 rho gtpase in pollen tubes. *Proc. Nati. Acad. Scie.*, 106(51):22002–22007, 2009.

[41] X.-S. Yang. Turing pattern formation of catalytic reaction-diffusion systems in engineering applications. *Modelling Simul. Mater. Sci. Eng.*, 11:321–329, May 2003.

[42] Xin-She Yang. Computational modelling of nonlinear calcium waves. *Applied Mathematical Modelling*, 30(2):200 – 208, 2006.

[43] Zhenbiao Yang. Signaling tip growth in plants. *Current Opinion in Plant Biology.*, 1(6):525–530, December 1998.

[44] F.-Q. Yi, J.-J. Wei, and J.-P. Shi. Bifurcation and spatiotemporal patterns in a homogeneous diffusive predator-prey system. *J. Differential Equations*, 246(5):1944–1977, 2009.

[45] T.-M. Yi, S.-Q. Chen, C.-S. Chou, and Q. Nie. Modeling yeast cell polarization induced by pheromone gradients. *Jour. Stat. Phys.*, 128(1-2):193–207, 2007.

[46] Z.-Z. Zheng, C.-S. Chou, T.-M. Yi, and Q. Nie. Mathematical analysis of steady-state solutions in compartment and continuum models of cell polarization. *Math. Biosci. Eng.*, 8(4):1135–1168, 2011.

Chapter 9

Appendix

9.1 Proof of Proposition 1

Proof. In this proposition, we study the number of roots of equation (**??**) with $1 < \alpha < 2$. The function $f(R)$ has the properties that

$$\lim_{R\to 0^+} f(R) = -\infty \quad \text{and} \quad \lim_{R\to\infty} f(R) = \infty. \tag{9.1}$$

Also, we have the first derivative of $f(R)$ as

$$f'(R) = \alpha R^{\alpha-1} - (\alpha-1)R^{\alpha-2} + k_3^2(\alpha-2)R^{\alpha-3} - k_3^2(\alpha-3)R^{\alpha-4}. \tag{9.2}$$

Let

$$h(R) = \alpha R^3 - (\alpha-1)R^2 + k_3^2(\alpha-2)R - k_3^2(\alpha-3). \tag{9.3}$$

So we have $f'(R) = R^{\alpha-4}h(R)$.

Step 1. There exists a unique $x_2 > 0$ such that $h'(R) < 0$ for $0 < R < x_2$, $h'(R) > 0$ for $R > x_2$, and $h(R)$ reaches the global minimum in $(0,\infty)$ at $R = x_2$.

Note that the function $h(R)$ has the properties that

$$h(0) = -k_3^2(\alpha - 3) > 0 \quad \text{and} \quad \lim_{R\to\infty} h(R) = \infty, \tag{9.4}$$

and we have the first derivative of $h(R)$ as

$$h'(R) = 3\alpha R^2 - 2(\alpha - 1)R + k_3^2(\alpha - 2). \tag{9.5}$$

Since $\alpha \in (1, 2)$, for (9.5), we have the discriminant $\triangle_1 = 4(\alpha - 1)^2 - 12k_3^2\alpha(\alpha - 2) > 0$. In this case, $h'(R) = 0$ must have two roots in $(-\infty, \infty)$. Notice that $\dfrac{2(\alpha - 1)}{3\alpha} > 0$ and $\dfrac{k_3^2(\alpha - 2)}{3\alpha} < 0$ so $h'(R)$ must have one negative root and one positive root. Let x_2 be the positive root of $h'(R) = 0$. Since $h'(0) = k_3^2(\alpha - 2) < 0$, we have $h'(R) < 0$ for $0 < R < x_2$, $h'(R) > 0$ for $R > x_2$. Therefore, $h(R)$ decreases for $0 < R < x_2$, and increases for $R > x_2$. That is to say, if $h(x_2) \geq 0$, then $h(R) \geq 0$ for any $R > 0$, while $h(R) = 0$ has two positive solutions if $h(x_2) < 0$.

Step 2. There exist $k_{31}, k_{32} > 0$ such that

$$h(x_2) \begin{cases} \geq 0, & \text{if } k_{31} < k_3 < k_{32}. \\ < 0, & \text{if } 0 < k_3 < k_{31} \text{ or } k_3 > k_{32}. \end{cases} \tag{9.6}$$

Since $h'(R)$ is an quadratic function and the relationship between $h(R)$ and $h'(R)$, we can have following two facts:

$$x_2 = \frac{(\alpha - 1) + \sqrt{(\alpha - 1)^2 - 3k_3^2\alpha(\alpha - 2)}}{3\alpha}, \tag{9.7}$$

$$h(x_2) = \left(\frac{x_2}{3} - \frac{\alpha - 1}{9\alpha}\right) h'(x_2) + \frac{6k_3^2\alpha(\alpha - 2) - 2(\alpha - 1)^2}{9\alpha} x_2 + \frac{k_3^2(\alpha - 1)(\alpha - 2) - 9k_3^2\alpha(\alpha - 3)}{9\alpha}. \tag{9.8}$$

Therefore, we have

$$h(x_2) \geq 0 \tag{9.9}$$

$$\Leftrightarrow \quad x_2 \leq \frac{(\alpha-1)(\alpha-2)-9\alpha(\alpha-3)}{2(\alpha-1)^2-6k_3^2\alpha(\alpha-2)}k_3^2 \tag{9.10}$$

$$\Leftrightarrow \quad \frac{(\alpha-1)+\sqrt{(\alpha-1)^2-3k_3^2\alpha(\alpha-2)}}{3\alpha} \leq \frac{(\alpha-1)(\alpha-2)-9\alpha(\alpha-3)}{2(\alpha-1)^2-6k_3^2\alpha(\alpha-2)}k_3^2 \tag{9.11}$$

$$\Leftrightarrow \quad Ak_3^4+Bk_3^2+C \geq 0, \tag{9.12}$$

where

$$A = \alpha(\alpha-2)^3 < 0, \tag{9.13}$$

$$B = 2(\alpha-1)^2(\alpha-2)^2-18(\alpha-1)(\alpha-2)+27 > 0, \tag{9.14}$$

$$C = (\alpha-1)^3(\alpha-3) < 0. \tag{9.15}$$

Notice that the discriminant of the quadratic function Ay^2+By+C is

$$\triangle_2 = [2(\alpha-1)^2(\alpha-2)^2-18(\alpha-1)(\alpha-2)+27]^2-4\alpha(\alpha-1)^3(\alpha-2)^3(\alpha-3) \tag{9.16}$$

$$= [2(\alpha-1)^2(\alpha-2)^2-18(\alpha-1)(\alpha-2)+27]^2-4(\alpha-1)^4(\alpha-2)^4+8(\alpha-1)^3(\alpha-2)^3 \tag{9.17}$$

$$> -18(\alpha-1)(\alpha-2)[4(\alpha-1)^2(\alpha-2)^2-18(\alpha-1)(\alpha-2)+27]+8(\alpha-1)^3(\alpha-2)^3 \tag{9.18}$$

$$= -2(\alpha-1)(\alpha-2)[32(\alpha-1)^2(\alpha-2)^2-162(\alpha-1)(\alpha-2)+243]. \tag{9.19}$$

Since the discriminant of the quadratic function $32y^2-162y+243$ is $\triangle_3 = 162^2-4\times 32\times 243 = -4860 < 0$, then $32(\alpha-1)^2(\alpha-2)^2-162(\alpha-1)(\alpha-2)+243 > 0$ for any α. Therefore

$$\triangle_2 > -2(\alpha-1)(\alpha-2)[32(\alpha-1)^2(\alpha-2)^2-162(\alpha-1)(\alpha-2)+243] > 0. \tag{9.20}$$

So the quadratic equation $Ay^2 + By + C = 0$ has two real-valued solutions $k_{31}^* < k_{32}^*$. Because $k_{31}^* + k_{32}^* = -\dfrac{B}{A} > 0$ and $k_{31}^* k_{32}^* = \dfrac{C}{A} > 0$, then k_{31}^* and k_{32}^* are both positive. Moreover we can have that $Ak_3^4 + Bk_3^2 + C \geq 0$ if and only if $k_{31}^* \leq k_3^2 \leq k_{32}^*$. Now let $k_{31} = \sqrt{k_{31}^*}$ and $k_{32} = \sqrt{k_{32}^*}$, we reach the conclusion in (9.6).

Step 3. We consider the number of roots of equation $f(R) = 0$ in (3.9) for each case in (9.6). In the case where $h(x_2) \geq 0$, we would have $h(R) \geq 0$ for any $R > 0$ because $h(R)$ decreases for $0 < R < x_2$, and increases for $R > x_2$. That is to say, $f'(R) = R^{\alpha-4}h(R) > 0$ for any $R > 0$. So $f(R)$ increases for all $R > 0$. According to property (9.1), $f(R) = 0$ has one unique positive root.

On the other hand, when $h(x_2) < 0$, $h(R) = 0$ has two positive solutions. Let $0 < r_1 < x_2 < r_2$ be the solutions of $h(R) = 0$. Then $h(R) > 0$ if $R \in [0, r_1) \cup (r_2, +\infty)$ and $h(R) < 0$ if $R \in (r_1, r_2)$. That is to say,

$$f'(R) = R^{\alpha-4}h(R) \begin{cases} > 0, & \text{if } R \in (0, r_1), \\ < 0, & \text{if } R \in (r_1, r_2), \\ > 0, & \text{if } R \in (r_2, +\infty). \end{cases} \tag{9.21}$$

Therefore, $f(R)$ increases for $0 < R < r_1$, decreases for $r_1 < R < r_2$, and increases when $R > r_2$. Then we know that

1. If $f(r_1)f(r_2) > 0$, then $f(R) = 0$ has one unique positive solution.

2. If $f(r_1)f(r_2) = 0$, then $f(R) = 0$ has two positive solutions.

3. If $f(r_1)f(r_2) < 0$, then $f(R) = 0$ has three positive solutions.

Define

$$l(R) = R^{\alpha-3}(1 - R)(R^2 + k_3^2). \tag{9.22}$$

Then $f(r_1)f(r_2) = [k_2 - l(r_1)][k_2 - l(r_2)]$. Since r_1 and r_2 are solutions of $h(R) = 0$, r_1 and r_2 only depends on α and k_3. So there exists k_{21}, k_{22} which only depends on α, k_3 and are defined as

$$k_{21} = r_1^{\alpha-3}(1 - r_1)(r_1^2 + k_3^2), \quad k_{22} = r_2^{\alpha-3}(1 - r_2)(r_2^2 + k_3^2), \tag{9.23}$$

such that

1. If $k_2 < k_{21}$ or $k_2 > k_{22}$, then $f(R) = 0$ has one unique positive solution.

2. If $k_2 = k_{21}$ or $k_2 = k_{22}$, then $f(R) = 0$ has two positive solutions.

3. If $k_{21} < k_2 < k_{22}$, then $f(R) = 0$ has three positive solutions.

We claim that $0 < k_{21} < k_{22}$ for $0 < k_3 < k_{31}$, while $k_{21} < k_{22} < 0$ for $k_3 > k_{32}$. This is equivalent to $r_1 < r_2 < 1$ for $0 < k_3 < k_{31}$, while $1 < r_1 < r_2$ for $k_3 < k_{32}$. Notice that $h(1) = 1 + k_3^2 > 0$, and that $h(R)$ decreases for $0 < R < x_2$ and increases for $R > x_2$. So we only need to prove that $h'(1) = \alpha + 2 + k_3^2(\alpha - 2) < 0$ for $0 < k_3 < k_{31}$, while $h'(1) > 0$ for $k_3 > k_{32}$. In fact, k_{31}^2 and k_{32}^2 are two positive roots of equation $Ay^2 + By + C = 0$, where A, B, C are defined as (9.13), (9.14) and (9.15) respectively. Notice that $A < 0$ and

$$A\left(\frac{2+\alpha}{2-\alpha}\right)^2 + B\left(\frac{2+\alpha}{2-\alpha}\right) + C = 32\left(\alpha - \frac{1}{4}\right)^2 + 54\frac{\alpha}{2-\alpha} > 0, \quad \text{for } 1 < \alpha < 2. \tag{9.24}$$

So $k_{31}^2 < \dfrac{2+\alpha}{2-\alpha} < k_{32}^2$. Therefore, we have

$$h'(1) = \alpha + 2 + k_3^2(\alpha - 2) > \alpha + 2 + k_{31}^2(\alpha - 2) > 0, \quad \text{if } 0 < k_3 < k_{31}, \tag{9.25}$$

$$h'(1) = \alpha + 2 + k_3^2(\alpha - 2) < \alpha + 2 + k_{32}^2(\alpha - 2) < 0, \quad \text{if } k_3 > k_{32}. \tag{9.26}$$

So we have proved that $0 < k_{21} < k_{22}$ for $0 < k_3 < k_{31}$, while $k_{21} < k_{22} < 0$ for $k_3 > k_{32}$. Therefore we reach the conclusion about number of solution of $f(R) = 0$. ■

9.2 Proof of Proposition 2

Proof. By the Center Manifold Theorem (Page 116 in [25]), we can compute the center manifold near the equilibrium $(0, 0)$:

$$C = \vartheta(R) = \frac{1}{k_1(2-\alpha)} R^{2-\alpha} + o(R^{2-\alpha}). \tag{9.27}$$

Then, by substituting (9.27) into the first equation of the kinetic system (2.5), we obtain the following scalar system which gives the flow of Eq. (2.5) on the center manifold:

$$R_t = k_1 R^\alpha (1-R) - k_1 k_2 \frac{R\vartheta^2(R)}{\vartheta^2(R) + k_3^2} > 0, \quad \text{for } 0 < R < \delta. \tag{9.28}$$

Thus, we know that the flow on the center manifold is moving away from the origin and it is an unstable orbit.

Next we show that there is an invariant region near $R = 0$, $C > 0$ for equation (3.6). Define

$$O = \left\{ (R, C) : 0 \le R \le \left(\frac{k_2}{2(k_3^2 + \delta^2)} \right)^{\frac{1}{\alpha-1}} C^{\frac{2}{\alpha-1}},\ 0 \le C \le \delta \right\}.$$

It is obvious that $R = 0$ is invariant for equation (3.6). Then, if $C = \delta$ and $0 \le R \le \left(\frac{k_2}{2(k_3^2 + \delta^2)} \right)^{\frac{1}{\alpha-1}} \delta^{\frac{2}{\alpha-1}}$, since $1 < \alpha < 2$ then $\frac{2}{\alpha-1} > 1$, so one can choose $\delta > 0$ small enough so that $\left(\frac{k_2}{2(k_3^2 + \delta^2)} \right)^{\frac{1}{\alpha-1}} \delta^{\frac{2}{\alpha-1}} \le \delta$. By using $C = \delta$, we have $C' < 0$.

On the boundary $R = \left(\frac{k_2}{2(k_3^2+\delta^2)}\right)^{\frac{1}{\alpha-1}} C^{\frac{2}{\alpha-1}}$, we have

$$\begin{aligned}
\frac{d}{dt}\left(\frac{R^{\frac{\alpha-1}{2}}}{C}\right) &= \frac{\frac{\alpha-1}{2}CR^{\frac{\alpha-3}{2}}R' - R^{\frac{\alpha-1}{2}}C'}{C^2} = \frac{R^{\frac{\alpha-3}{2}}}{C^2}\left(\frac{\alpha-1}{2}CR' - RC'\right) \\
&= \frac{R^{\frac{\alpha-3}{2}}}{C^2}\left[\frac{\alpha-1}{2}Ck_1\left(R^\alpha - R^{\alpha+1} - k_2\frac{RC^2}{C^2+k_3^2}\right) - R^2 + CR\right] \\
&\le \frac{R^{\frac{\alpha-3}{2}}}{C}\left[\frac{\alpha-1}{2}k_1\left(R^\alpha - k_2\frac{RC^2}{C^2+k_3^2}\right) + R\right] \\
&\le \frac{R^{\frac{\alpha-3}{2}}}{C}\left[(\alpha-1)k_1R^\alpha - \frac{(\alpha-1)k_1k_2RC^2}{2(C^2+k_3^2)}\right] \\
&\le \frac{R^{\frac{\alpha-3}{2}}}{C}\left[(\alpha-1)k_1\left(R^\alpha - \frac{(\alpha-1)k_1k_2RC^2}{2(\delta^2+k_3^2)}\right)\right] \\
&= (\alpha-1)R^{\frac{\alpha-1}{2}}k_1C^2\left[\frac{R^{\alpha-1}}{C^2} - \frac{k_2}{2(\delta^2+k_3^2)}\right] = 0,
\end{aligned}$$

and the first inequality holds for R small enough: $R < \frac{\alpha-1}{2}k_1R^\alpha$. The above calculation implies that the dynamics of (3.6) is inward on $R = \left(\frac{k_2}{2(k_3^2+\delta^2)}\right)^{\frac{1}{\alpha-1}} C^{\frac{2}{\alpha-1}}$. This shows that O is an invariant region for Eq. (3.6), and any orbit in O converges to the origin. It is also clear that when $R = 0,\ C > 0$ (the positive C-axis), we have $(R_t, C_t) = (0, -C)$. So we know that all the solutions starting from $R = 0,\ C > 0$ will always stay on this curve and eventually converge to the origin. One can choose a maximum orbit $R = h_s(C)$ so that all orbits such that $0 \le R \le h_s(C)$ converge to the origin. Then other trajectories exhibits saddle behavior near the origin. ■

9.3 Proof of Theorem 3

Proof. First, we look at the determinant of the Jacobian matrix $J(R_j, R_j)$: $\det(J(R_j, R_j)) = k_1R_j(f_2'(R_j) - f_1'(R_j))$, where f_1, f_2 are defined in (3.11). From (3.11),

we have

$$f_2(R) - f_1(R) = \frac{k_2 R^2}{R^2 + k_3^2} - R^{\alpha-1}(1-R) \tag{9.29}$$

$$\Leftrightarrow f(R) = k_2 - R^{\alpha-3}(1-R)(R^2+k_3^2) = \frac{R^2+k_3^2}{R^2}(f_2(R) - f_1(R)) \tag{9.30}$$

$$\Leftrightarrow f'(R) = -\frac{2k_3^2}{R^3}(f_2(R) - f_1(R)) + \frac{R^2+k_3^2}{R^2}(f_2'(R) - f_1'(R)). \tag{9.31}$$

From (9.30), we know that $f_2(R) - f_1(R) = 0$ when $f(R) = 0$. Since positive steady states (R_j, R_j) $(j = 1, 2, 3)$ satisfy $f(R_j) = 0$, we have $f_2(R_j) - f_1(R_j) = 0$. Therefore, from (9.31), we know

$$f'(R_j) > 0 \Leftrightarrow f_2'(R_j) - f_1'(R_j) > 0 \Leftrightarrow \det(J(R_j, R_j)) > 0;$$

$$f'(R_j) = 0 \Leftrightarrow f_2'(R_j) - f_1'(R_j) = 0 \Leftrightarrow \det(J(R_j, R_j)) = 0;$$

$$f'(R_j) < 0 \Leftrightarrow f_2'(R_j) - f_1'(R_j) < 0 \Leftrightarrow \det(J(R_j, R_j)) < 0.$$

According to the proof of Proposition 1, we have the following result of $\mathrm{Det}(J(R_j, R_j))$: there exists a constant $k_{31} > 0$ such that

1. If $0 < k_3 < k_{31}$, then there exists r_1 and r_2, which are two positive solutions of $h(R) = 0$, such that

   (a) $f'(R) > 0 \Rightarrow \mathrm{Det}(J(R,R)) > 0$ for $R \in (0, r_1) \cup (r_2, 1)$;

   (b) $f'(R) < 0 \Rightarrow \mathrm{Det}(J(R,R)) < 0$ for $R \in (r_1, r_2)$.

2. If $k_{31} < k_3$, then for any $0 < R < 1$, we always have $f'(R) > 0 \Rightarrow \mathrm{Det}(J(R,R)) > 0$.

Here we want to point out that from (9.23), we have $k_2(r_1) = k_{21}$ and $k_2(r_2) = k_{22}$.

Next we look at the trace of Jacobian matrix (3.10): $\text{Trace}(J(R_j, C_j)) = k_1 R_j f_1'(R_j) -$ 1. Define a new function

$$g(R) = Rf_1'(R) = R^{\alpha-1}[(\alpha-1) - \alpha R]. \tag{9.32}$$

We observe that $g(R)$ has the following properties:

$$g(0) = 0, \quad g\left(\frac{\alpha-1}{\alpha}\right) = 0, \quad \text{and} \quad \lim_{R\to\infty} g(R) = \infty. \tag{9.33}$$

Also we have the first derivative of $g(R)$ as

$$g'(R) = R^{\alpha-2}[(\alpha-1)^2 - \alpha^2 R]. \tag{9.34}$$

Hence the function $g(R)$ increases for $0 < R < \left(\frac{\alpha-1}{\alpha}\right)^2$ and decreases for $R > \left(\frac{\alpha-1}{\alpha}\right)^2$. So $g(R)$ achieves its maximum at $R = \left(\frac{\alpha-1}{\alpha}\right)^2$ with $g\left(\left(\frac{\alpha-1}{\alpha}\right)^2\right) = \left(\frac{\alpha-1}{\alpha}\right)^{2\alpha-1}$.

Therefore we conclude that

1. If $k_1 < \left(\frac{\alpha}{\alpha-1}\right)^{2\alpha-1}$, then

$$\text{Trace}(J(R,R)) = k_1 g(R) - 1 < \left(\frac{\alpha}{\alpha-1}\right)^{2\alpha-1}\left(\frac{\alpha-1}{\alpha}\right)^{2\alpha-1} - 1 = 0. \tag{9.35}$$

2. If $k_1 > \left(\frac{\alpha}{\alpha-1}\right)^{2\alpha-1}$, then there exists $0 < \tilde{R}_1 < \tilde{R}_2$, such that $g(\tilde{R}_1) = g(\tilde{R}_2) = \frac{1}{k_1}$. Therefore,

   (a) If $\tilde{R}_1 < R < \tilde{R}_2$, then $\text{Trace}(J(R,R)) = k_1 g(R) - 1 > k_1 g(\tilde{R}_1) = 0$.

   (b) If $0 < R < \tilde{R}_1$ or $\tilde{R}_2 < R < 1$, then $\text{Trace}(J(R,R)) = k_1 g(R) - 1 < k_1 g(\tilde{R}_1) = 0$.

■

9.4 Proof of Proposition 4

Proof. From the proof of Theorem 3, we can easily get Part 1 in Proposition 4. So here we only discuss Part 2: the case that $0 < k_3 < k_{31}$. Since $\mathrm{Det}(J(R_2, C_2)) < 0$, the steady state (R_2, C_2) is always a saddle point. So we focus on the positive steady states (R_1, C_1) and (R_3, C_3). To prove the results in Proposition 4, we need to determine the order of the possible bifurcation points: r_1, r_2, $\tilde{R}_1$ and $\tilde{R}_2$, where r_1 and r_2 are the steady state bifurcation points satisfying $h(r_1) = h(r_2) = 0$ with $h(R)$ defined in (9.3), and $\tilde{R}_1$, $\tilde{R}_2$ are possible Hopf bifurcation points satisfying $g(\tilde{R}_1) = g(\tilde{R}_2) = 1/k_1$. Then, by the results of Theorem 3, we can obtain the stability of each steady state.

First, we prove that $g(r_1) > g(r_2)$ always holds. From the definition of $h(R)$, we know that

$$h(r_1) = \alpha r_1^3 - (\alpha - 1) r_1^2 + k_3^2(\alpha - 2) r_1 - k_3^2(a\alpha - 3) = 0. \tag{9.36}$$

Multiplying (9.36) by $r_1^{\alpha-3}$, we have

$$\alpha r_1^{\alpha} - (\alpha - 1) r_1^{\alpha-1} + k_3^2(\alpha - 2) r_1^{\alpha-2} - k_3^2(a\alpha - 3) r_1^{\alpha-3} = 0, \tag{9.37}$$

which together with $g(r_1) = -\alpha r_1^{\alpha} + (\alpha - 1) r_1^{\alpha-1}$ from (9.32) implies that

$$g(r_1) = k_3^2(\alpha - 2) r_1^{\alpha-2} - k_3^2(\alpha - 3) r_1^{\alpha-3}. \tag{9.38}$$

Define

$$G(R) = k_3^2(\alpha - 2) R^{\alpha-2} - k_3^2(\alpha - 3) R^{\alpha-3},\ R \in (0, 1),\ \alpha \in (1, 2). \tag{9.39}$$

By direct calculation, we have $G'(R) = k_3^2(\alpha - 2)^2 R^{\alpha-3} - k_3^2(\alpha - 3)^2 R^{\alpha-4}$ and $G'(R) < 0$ for $R \in \left(0, \left(\frac{\alpha-3}{\alpha-2}\right)^2\right) \supset (0, 1)$. Therefore, $G(R)$ is strictly decreasing for $R \in (0, 1)$. By the fact that $0 < r_1 < r_2 < 1$, immediately we reach the conclusion that $g(r_1) > g(r_2)$.

Now we consider the case that $0 < k_3 < k_{31}$ which implies the existence of multiple steady states. For the convenience of discussion, we define

$$\tilde{g}(R) = g(R) - 1/k_1, \tag{9.40}$$

then we know that $\tilde{g}$ has two zeros $\tilde{R}_1$ and $\tilde{R}_2$. For the order of r_1, r_2, $\tilde{R}_1$ and $\tilde{R}_2$, we have the following six possible situations:

(i) $r_1 < r_2 < \tilde{R}_1 < \tilde{R}_2$. We show that this case will not happen. By the property of $h(R)$, it is not difficult to verify that $h\left(\left(\frac{\alpha-1}{\alpha}\right)^2\right) > 0 = h(r_2)$, so we know that $\left(\frac{\alpha-1}{\alpha}\right)^2 < r_2$. Because $\left(\frac{\alpha-1}{\alpha}\right)^2$ is the maximum point of $\tilde{g}(R)$ and $\tilde{R}_1$ is the smallest root of $\tilde{g}(R)$, so we have $\tilde{R}_1 < r_2$ which is a contradiction to the assumption.

(ii) $r_1 < \tilde{R}_1 < r_2 < \tilde{R}_2$. By the fact that $\tilde{g}(R) > 0$ for $R \in (\tilde{R}_1, \tilde{R}_1)$ and $g(R) < 0$ for $R \in (0, \tilde{R}_1) \cup (\tilde{R}_2, 1)$, it is easy to obtain that $\tilde{g}(r_1) < 0$ since $r_1 < \tilde{R}_1$, which is equivalent to $k_1 < 1/g(r_1)$. Also, by $\tilde{g}(r_2) > 0$, we have $k_1 > 1/g(r_2)$. However, it has been proved that $g(r_1) > g(r_2)$, so the set $(1/g(r_2), 1/g(r_1))$ is empty, which means that this case cannot happen.

(iii) $\tilde{R}_1 < r_1 < r_2 < \tilde{R}_2$ (see Fig. 3.5c). Because that $r_1,\ r_2 \in (\tilde{R}_1, \tilde{R}_2)$, so we have $\tilde{g}(r_1) > 0$ and $\tilde{g}(r_2) > 0$, which is equivalent to $k_1 > 1/g(r_2)$. In this case, by Theorem 3, we know that Hopf bifurcations occur at both of (R_1, R_1) and (R_3, R_3).

(iv) $\tilde{R}_1 < r_1 < \tilde{R}_2 < r_2$ (see Fig. 3.5d). By similar argument, since $r_1 \in (\tilde{R}_1, \tilde{R}_2)$ and $r_2 > \tilde{R}_2$, we can obtain that $\tilde{g}(r_1) > 0$ and $\tilde{g}(r_2) < 0$ which imply that $k_1 \in (1/g(r_1), 1/g(r_2))$. In this case, from $\tilde{R}_1 < r_1 < \tilde{R}_2 < r_2$ and Theorem 3, a Hopf bifurcation only occurs at (R_3, R_3) and does not occur at (R_1, R_1).

(v) $r_1 < \tilde{R}_1 < \tilde{R}_2 < r_2$ (see Fig. 3.5e). Similarly, we have $\tilde{g}(r_1) < 0$ and $\tilde{g}(r_2) < 0$, then it can be inferred that $k_{11} < k_1 < 1/g(r_1)$. In this case, no Hopf bifurcation can occur. Also, we have $\left(\frac{\alpha-1}{\alpha}\right)^2 > r_1$ in this case, which will be used later.

(vi) $\tilde{R}_1 < \tilde{R}_2 < r_1 < r_2$ (see Fig. 3.5f). In this case, we still have $k_{11} < k_1 < 1/g(r_1)$, but the difference with case (v) is that $\left(\frac{\alpha-1}{\alpha}\right)^2 < r_1$. In this case, two Hopf bifurcations occur at (R_1, R_1).

So in order to distinguish the last two cases, we define $\tilde{k}_3$ to be the value of k_3 such that $r_1 = \left(\frac{\alpha-1}{\alpha}\right)^2$, and it is easy to calculate that $\tilde{k}_3$ is given by (3.21). So case (v) is for $0 < k_3 < \tilde{k}_3$ which is equivalent to $r_1 < \left(\frac{\alpha-1}{\alpha}\right)^2$ and case (vi) is for $\tilde{k}_3 < k_3 < k_{31}$ which implies $r_1 > \left(\frac{\alpha-1}{\alpha}\right)^2$. Also we must have that $\tilde{k}_3 < k_{31}$. Suppose not, then first we assume that $k_3 > k_{32}$, then $h(R) = 0$ has two positive solutions, but both of them should be bigger than 1 and here we have $0 < R < 1$ which is a contradiction. If $k_{31} < k_3 < k_{32}$, then $h(R) = 0$ has no roots, so it contradicts with the fact that $h(R) = 0$ has one of positive roots at $(\frac{\alpha-1}{\alpha})^2 < 1$ when $k_3 = \tilde{k}_3$. Therefore, we can conclude that $\tilde{k}_3 < k_{31}$. Finally if $0 < k_1 < k_{11}$, then $\tilde{g}(R)$ has no zeros, (R_1, R_1) and (R_3, R_3) are both always linearly stable and Hopf bifurcation will not occur, which is similar to (v) above.

In summary the case (c) is implied by (iii) above, case (d) is implied by (iv) above, case (e) is implied by (v) and the case of $0 < k_1 < k_{11}$, and case (f) is implied by (vi) above. The proof is completed. ■

9.5 Proof of Lemma 5

Proof. By the Fourier expansion, we can write the eigenfunction of (3.22) as

$$(\phi, \psi)^T = \sum_{n=0}^{\infty} (a_n,\ b_n)^T \varphi_n(x). \tag{9.41}$$

Substituting (9.41) into (3.22), multiplying both sides by $\varphi_n(x)$ and integrating the equations on $[-L, L]$, then by using the orthogonality of $\varphi_n(x)$, we obtain that

$$J_n(a_n, b_n)^T = \mu(a_n, b_n)^T, \quad \text{for} \quad n \in \mathbb{N}_0.$$

Note that the nonlocal term

$$\int_{-L}^{L} \phi(x)dx = \int_{-L}^{L} \sum_{n=0}^{\infty} a_n \varphi_n(x)dx = \begin{cases} a_n, & n = 0; \\ \\ 0, & n = 1, 2, \cdots \end{cases},$$

so J_0 is different from other J_n with $n \geq 1$. Therefore, we know that the eigenvalues of (3.22) are identical with those of the matrix J_n ($n \in \mathbb{N}_0$), so the stability of the constant equilibrium (R_*, R_*) is determined by the eigenvalues of J_n. By [31, Theorem 8.6], (R_*, R_*) is locally asymptotically stable when the real parts of all the eigenvalues of J_n ($n \in \mathbb{N}_0$) are negative and, it is unstable when there exists a J_n with eigenvalues of positive real part. ■

9.6 Proof of Lemma 14

Proof.

$$S_1(\theta_1,\theta_2) = \int_0^T \left[\hat{\dot{F}}_0(t) - \hat{G}_0(t)\theta_1 - \hat{F}_0(t)\theta_2\right]^2 dt$$

$$= ||\hat{\dot{F}}_0(t) - \dot{F}_0(t)||^2 \tag{9.42}$$

$$+ ||\theta_1^* G_0(t) + \theta_2^* F_0(t) - \theta_1\hat{G}_0(t) - \theta_2\hat{F}_0(t)||^2 \tag{9.43}$$

$$+ 2\langle \hat{\dot{F}}_0(t) - \dot{F}_0(t), \theta_1^* G_0(t) + \theta_2^* F_0(t) - \theta_1\hat{G}_0(t) - \theta_2\hat{F}_0(t)\rangle \tag{9.44}$$

Based on consistency of $\hat{\dot{F}}_0$, the first term (9.42) is of order $O_p(N_{T,est}^2/n_t + N_{T,est}^{-2\alpha+1} + n_x^{-2})$. As for the second term (9.43), we have

$$||\theta_1^* G_0(t) + \theta_2^* F_0(t) - \theta_1\hat{G}_0(t) - \theta_2\hat{F}_0(t)||^2 \tag{9.45}$$

$$= ||\theta_1 G_0(t) + \theta_2 F_0(t) - \theta_1\hat{G}_0(t) - \theta_2\hat{F}_0(t)||^2 \tag{9.46}$$

$$+ ||\theta_1^* G_0(t) + \theta_2^* F_0(t) - \theta_1 G_0(t) - \theta_2 F_0||^2 \tag{9.47}$$

$$+ 2\langle \theta_1 G_0(t) + \theta_2 F_0(t) - \theta_1\hat{G}_0(t) - \theta_2\hat{F}_0(t), \theta_1^* G_0(t) + \theta_2^* F_0(t) - \theta_1 G_0(t) - \theta_2 F_0(t)\rangle$$

Based on consistency of $\hat{G}_0(t)$ and $\hat{F}_0(t)$, the first term (9.46) is of order $O_p(N_{T,est}/n_t + N_{T,est}^{-2\alpha} + n_x^{-2})$. According to Cauchy-Schwartz inequality, (9.43) is dominate by (9.47), which is $\int_0^T \left[(\theta_1^* - \theta_1)G_0(t) + (\theta_2^* - \theta_2)F_0(t)\right]^2 dt$. Therefore, limit behavior of $S_1(\theta_1,\theta_2)$ can be evaluated as

$$S_1(\theta_1,\theta_2) = \int_0^T \left[(\theta_1^* - \theta_1)G_0(t) + (\theta_2^* - \theta_2)F_0(t)\right]^2 dt + O_p(N_{T,est}^2/n_t + N_{T,est}^{-2\alpha+1} + n_x^{-2})$$

■

9.7 Proof of Lemma 16

Proof. In fact, the logic of proof of Lemma 16 is similar as that of Lemma 14.

$$\sum_{n=1}^{N_{X,est}} \int_0^T \left[\hat{\theta}_1 \hat{G}_n(t) - \theta_1^* G_n(t)\right]^2 dt = \sum_{n=1}^{N_{X,est}} ||\hat{\theta}_1 \hat{G}_n(t) - \hat{\theta}_1 G_n(t)||^2 + \sum_{n=1}^{N_{X,est}} ||\hat{\theta}_1 G_n(t) - \theta_1^* G_n(t)||^2 + 2\langle \hat{\theta}_1 \hat{G}_n(t) - \hat{\theta}_1 G_n(t), \hat{\theta}_1 G_n(t) - \theta_1^* G_n(t)\rangle$$

Now we look at each term:

$$\sum_{n=1}^{N_{X,est}} ||\hat{\theta}_1 \hat{G}_n(t) - \hat{\theta}_1 G_n(t)||^2 = \sum_{n=1}^{N_{X,est}} [\beta_1^* + O_p(d_{n_x,N_{T_est},n_t})]^2 ||\hat{G}_n(t) - G_n(t)||^2 = O_p(c_{n_x,N_{T,est},n_t})$$

$$\sum_{n=1}^{N_{X,est}} ||\hat{\theta}_1 G_n(t) - \theta_1^* G_n(t)||^2 = \sum_{n=1}^{N_{X,est}} ||G_n(t)||^2 (\hat{\theta}_1 - \theta_1^*)^2 = O_p(d^2_{n_x,N_{T,est},n_t})$$

With application of Cauchy-Schwartz inequality, we have

$$\sum_{n=1}^{N_{X,est}} \int_0^T \left[\hat{\theta}_1 \hat{G}_n(t) - \theta_1^* G_n(t)\right]^2 dt = O_p(c_{n_x,N_{T,est},n_t}) + O_p(d^2_{n_x,N_{T,est},n_t}) \tag{9.48}$$

Similarly, we have

$$\sum_{n=1}^{N_{X,est}} \int_0^T \left[\hat{\theta}_2 \hat{F}_n(t) - \theta_2^* F_n(t)\right]^2 dt = O_p(c_{n_x,N_{T,est},n_t}) + O_p(d^2_{n_x,N_{T,est},n_t}) \tag{9.49}$$

■

9.8 Proof of Lemma 18

Proof. According to consistency and normality of smoothed data, we know that $\hat{G}_0(t)$ and $\hat{F}_0(t)$ converges to true value $G_0(t)$ and $F_0(t)$. Moreover, we know that

$$\text{cov}(\hat{\boldsymbol{G}}_{\boldsymbol{0}}) = \boldsymbol{\Phi}(\boldsymbol{\Phi}^T\boldsymbol{\Phi})^{-1}\boldsymbol{\Phi}^T s_1 \qquad \text{cov}(\hat{\boldsymbol{F}}_{\boldsymbol{0}}) = \boldsymbol{\Phi}(\boldsymbol{\Phi}^T\boldsymbol{\Phi})^{-1}\boldsymbol{\Phi}^T s_2$$

$$\text{cov}(\hat{\dot{\boldsymbol{F}}}_{\boldsymbol{0}}) = \dot{\boldsymbol{\Phi}}(\boldsymbol{\Phi}^T\boldsymbol{\Phi})^{-1}\dot{\boldsymbol{\Phi}}^T s_2 \qquad \text{cov}(\hat{\dot{\boldsymbol{F}}}_{\boldsymbol{0}}, \boldsymbol{F}_{\boldsymbol{0}}) = \dot{\boldsymbol{\Phi}}(\Phi^T\boldsymbol{\Phi})^{-1}\boldsymbol{\Phi}^T s_2$$

Therefore, with simple calculation, we have

$$\begin{pmatrix} \langle \hat{G}_0(t)\theta_1^* + \hat{F}_0(t)\theta_2^* - \hat{\dot{F}}_0(t), \hat{G}_0(t) \rangle \\ \langle \hat{G}_0(t)\theta_1^* + \hat{F}_0(t)\theta_2^* - \hat{\dot{F}}_0(t), \hat{F}_0(t) \rangle \end{pmatrix}_{n_t}$$

$$\to \frac{T}{n_t} \begin{pmatrix} \hat{\boldsymbol{G}}_{\mathbf{0}}{}^T \\ \hat{\boldsymbol{F}}_{\mathbf{0}}{}^T \end{pmatrix} \begin{pmatrix} -\theta_1^* \boldsymbol{I}_{\boldsymbol{n_t}} & -\theta_2^* \boldsymbol{I}_{\boldsymbol{n_t}} & \boldsymbol{I}_{\boldsymbol{n_t}} \end{pmatrix} \begin{pmatrix} \hat{\boldsymbol{G}}_{\mathbf{0}} - \mathbb{E}(\hat{\boldsymbol{G}}_{\mathbf{0}}) \\ \hat{\boldsymbol{F}}_{\mathbf{0}} - \mathbb{E}(\hat{\boldsymbol{F}}_{\mathbf{0}}) \\ \hat{\dot{\boldsymbol{F}}}_{\mathbf{0}} - \mathbb{E}(\hat{\dot{\boldsymbol{F}}}_{\mathbf{0}}) \end{pmatrix}$$

$$\sim MVN \left(\begin{pmatrix} 0 \\ 0 \end{pmatrix}, \left(\frac{T}{n_t}\right)^2 \boldsymbol{B_1} \right)$$

where $\boldsymbol{B_1} = \begin{pmatrix} s_{11} & s_{12} \\ s_{12} & s_{22} \end{pmatrix}$, and

$$s_{11} = \theta_1^{*2} \boldsymbol{G_0}^T \boldsymbol{\Phi} (\boldsymbol{\Phi}^T \boldsymbol{\Phi})^{-1} \boldsymbol{\Phi}^T \boldsymbol{G_0} s_1 + \left[\theta_2^* \boldsymbol{G_0}^T \boldsymbol{\Phi} - \boldsymbol{G_0}^T \dot{\boldsymbol{\Phi}} \right] (\boldsymbol{\Phi}^T \boldsymbol{\Phi})^{-1} \left[\theta_2^* \boldsymbol{G_0}^T \boldsymbol{\Phi} - \boldsymbol{G_0}^T \dot{\boldsymbol{\Phi}} \right]^T s_2$$

$$s_{22} = \theta_1^{*2} \boldsymbol{F_0}^T \boldsymbol{\Phi} (\boldsymbol{\Phi}^T \boldsymbol{\Phi})^{-1} \boldsymbol{\Phi}^T \boldsymbol{F_0} s_1 + \left[\theta_2^* \boldsymbol{F_0}^T \boldsymbol{\Phi} - \boldsymbol{F_0}^T \dot{\boldsymbol{\Phi}} \right] (\boldsymbol{\Phi}^T \boldsymbol{\Phi})^{-1} \left[\theta_2^* \boldsymbol{F_0}^T \boldsymbol{\Phi} - \boldsymbol{F_0}^T \dot{\boldsymbol{\Phi}} \right]^T s_2$$

$$s_{12} = \theta_1^{*2} \boldsymbol{G_0}^T \boldsymbol{\Phi} (\boldsymbol{\Phi}^T \boldsymbol{\Phi})^{-1} \boldsymbol{\Phi}^T \boldsymbol{F_0} s_1 + \theta_2^{*2} \boldsymbol{G_0}^T \boldsymbol{\Phi} (\boldsymbol{\Phi}^T \boldsymbol{\Phi})^{-1} \boldsymbol{\Phi}^T \boldsymbol{F_0} s_2 + \boldsymbol{G_0}^T \dot{\boldsymbol{\Phi}} (\boldsymbol{\Phi}^T \boldsymbol{\Phi})^{-1} \dot{\boldsymbol{\Phi}}^T \boldsymbol{F_0} s_2$$
$$- \theta_2^* \boldsymbol{G_0}^T \dot{\boldsymbol{\Phi}} (\boldsymbol{\Phi}^T \boldsymbol{\Phi})^{-1} \boldsymbol{\Phi}^T \boldsymbol{F_0} s_2 - \theta_2^* \boldsymbol{G_0}^T \boldsymbol{\Phi} (\boldsymbol{\Phi}^T \boldsymbol{\Phi})^{-1} \dot{\boldsymbol{\Phi}}^T \boldsymbol{F_0} s_2$$

With understanding of $\boldsymbol{G_0}^T \boldsymbol{\Phi} (\boldsymbol{\Phi}^T \boldsymbol{\Phi})^{-1} \boldsymbol{\Phi}^T \boldsymbol{G_0}$, we can know the large sample behavior of s_{11}, s_{12} and s_{22}. First, we look at $(\boldsymbol{\Phi}^T \boldsymbol{\Phi})^{-1}$.

$$\boldsymbol{\Phi}^T \boldsymbol{\Phi} = \left(\boldsymbol{\phi}_i^T \boldsymbol{\phi}_j \right)_{N_{T,est} \times N_{T,est}} = \frac{n_t}{T} \left(\int_0^T \phi_i(t) \phi_j(t) dt + O(N_{T,est}/n_t) \right)_{N_{T,est} \times N_{T,est}}$$

So $\left(\boldsymbol{\Phi}^T \boldsymbol{\Phi} \right)^{-1} = \frac{T}{n_t} \left[\boldsymbol{Q} + O(N_{T,est}/n_t) \right]$ where $\boldsymbol{Q}$ is inverse of a $N_{T,est} \times N_{T,est}$ matrix, of which elements on i-th row and j-th column is $\int_0^T \phi_i(t) \phi_j(t) dt$.

Then, we look at vectors $\boldsymbol{G_0}^T\boldsymbol{\Phi}$.

$$\begin{aligned}\boldsymbol{G_0}^T\boldsymbol{\Phi} &= n_t\left[\begin{array}{cccc}\frac{1}{n_t}\boldsymbol{G_0}^T\boldsymbol{\phi}_1 & \frac{1}{n_t}\boldsymbol{G_0}^T\boldsymbol{\phi}_2 & \cdots & \frac{1}{n_t}\boldsymbol{G_0}^T\boldsymbol{\phi}_{N_{T,est}}\end{array}\right] \\ &= \frac{n_t}{T}\left[\begin{array}{cccc}\int_0^T G_0(t)\phi_1(t)dt + O(n_t^{-1}) & \cdots & \int_0^T G_0(t)\phi_{N_{T,est}}(t)dt + O(\frac{N_{T,est}}{n_t})\end{array}\right] \\ &\triangleq \frac{n_t}{T}\left[\boldsymbol{\xi_G} + O(N_{T,est}/n_t)\right] \end{aligned} \tag{9.50}$$

Therefore, we have

$$\begin{aligned}&\boldsymbol{G_0}^T\boldsymbol{\Phi}(\boldsymbol{\Phi}^T\boldsymbol{\Phi})^{-1}\boldsymbol{\Phi}^T\boldsymbol{G_0} \\ &= \left\{\frac{n_t}{T}\left[\boldsymbol{\xi_G} + O(N_{T,est}/n_t)\right]\right\}\left\{\frac{T}{n_t}\left[\boldsymbol{Q} + O(N_{T,est}/n_t)\right]\right\}\left\{\frac{n_t}{T}\left[\boldsymbol{\xi_G} + O(N_{T,est}/n_t)\right]\right\}^T \\ &= \frac{n_t}{T}\left[\boldsymbol{\xi_G}\boldsymbol{Q}\boldsymbol{\xi_G}^T + O(N_{T,est}/n_t)\right]\end{aligned} \tag{9.51}$$

Furthermore,

$$\boldsymbol{\xi_G}\boldsymbol{Q}\boldsymbol{\xi_G}^T = \text{trace}(\boldsymbol{\xi_G}\boldsymbol{Q}\boldsymbol{\xi_G}^T) = \text{trace}(\boldsymbol{Q}\boldsymbol{\xi_G}^T\boldsymbol{\xi_G}) \tag{9.52}$$

If T is multiple of period, then $\boldsymbol{Q}$ is diagonal with elements $Q_{ii} = \frac{1}{\int \phi_i^2(t)dt}$. The elements on i-th row and j-th column of $\boldsymbol{\xi_G}^T\boldsymbol{\xi_G}$ is $\int G_0(t)\phi_i(t)dt \int G_0(t)\phi_j(t)dt$. According to Parseval Identity, we have

$$\text{trace}(\boldsymbol{Q}\boldsymbol{\xi_G}^T\boldsymbol{\xi_G}) = \sum_{i=1}^{N_{T,est}} \frac{(\int G_0(t)\phi_i(t)dt)^2}{\int \phi_i(t)^2dt} \to ||G_0(t)||^2 \tag{9.53}$$

Hence, $\boldsymbol{G_0}^T\boldsymbol{\Phi}(\boldsymbol{\Phi}^T\boldsymbol{\Phi})^{-1}\boldsymbol{\Phi}^T\boldsymbol{G_0} = \frac{n_t}{T}\left[||G_0(t)||^2 + O(N_{T,est}/n_t)\right]$. Therefore, we have

$$\begin{aligned}s_{11} &\to \frac{n_t\Delta\boldsymbol{x}}{T}\sigma_{11} = \frac{n_t\Delta\boldsymbol{x}}{T}\left[\theta_1^{*^2}||G_0(t)||^2\sigma_g^2 + ||\theta_2^*G_0(t) - \dot{G}_0(t)||^2\sigma_f^2\right] \\ s_{12} &\to \frac{n_t\Delta\boldsymbol{x}}{T}\sigma_{12} = \frac{n_t\Delta\boldsymbol{x}}{T}\left[\theta_1^{*^2}\langle G_0(t), F_0(t)\rangle\sigma_g^2 + \langle\theta_2^*G_0(t) - \dot{G}_0(t), \theta_2^*F_0(t) - \dot{F}_0(t)\rangle\sigma_f^2\right] \\ s_{22} &\to \frac{n_t\Delta\boldsymbol{x}}{T}\sigma_{22} = \frac{n_t\Delta\boldsymbol{x}}{T}\left[\theta_1^{*^2}||F_0(t)||^2\sigma_g^2 + ||\theta_2^*F_0(t) - \dot{F}_0(t)||^2\sigma_f^2\right]\end{aligned}$$

Thus, $\left(\frac{T}{n_t}\right)^2 \boldsymbol{B_1} \to \frac{T\Delta \boldsymbol{x}}{n_t}\boldsymbol{B_1}^*$, which means $\begin{pmatrix} \langle \hat{G}_0(t)\theta_1^* + \hat{F}_0(t)\theta_2^* - \hat{\dot{F}}_0(t), \hat{G}_0(t)\rangle \\ \langle \hat{G}_0(t)\theta_1^* + \hat{F}_0(t)\theta_2^* - \hat{\dot{F}}_0(t), \hat{F}_0(t)\rangle \end{pmatrix}$ is multivariate normally distributed with mean zero and variance-covariance matrix $\boldsymbol{B_1} \to \frac{T\Delta x}{n_t}\boldsymbol{B_1}^*$. ■

9.9 Proof of Lemma 20

Proof. Since, in practice, the inner products are approximated by summation of smoothed data. Based on consistency of smoothed data, we have

$$\sum_{n=1}^{N_{X,est}} \langle \hat{\dot{F}}_n(t) - \hat{\theta}_1\hat{G}_n(t) - \hat{\theta}_2\hat{F}_n(t) + \lambda_n\hat{F}_n(t)D^*, -\lambda_n\hat{F}_n(t)\rangle_{n_t}$$

$$= \frac{T}{n_t}\sum_{n=1}^{N_{X,est}} \left[-\lambda_n\hat{\boldsymbol{F}}_{\boldsymbol{n}}{}^T\right] \begin{pmatrix} -D^*\boldsymbol{I}_{\boldsymbol{n_t}} & \boldsymbol{I}_{\boldsymbol{n_t}} \end{pmatrix} \begin{pmatrix} -\lambda_n\hat{\boldsymbol{F}}_{\boldsymbol{n}} + \mathbb{E}(\lambda_n\hat{\boldsymbol{F}}_{\boldsymbol{n}}) \\ \hat{\dot{\boldsymbol{F}}}_{\boldsymbol{n}} - \hat{\theta}_1\hat{\boldsymbol{G}}_{\boldsymbol{n}} - \hat{\theta}_2\hat{\boldsymbol{F}}_{\boldsymbol{n}} - \mathbb{E}(\hat{\dot{\boldsymbol{F}}}_{\boldsymbol{n}} - \hat{\theta}_1\hat{\boldsymbol{G}}_{\boldsymbol{n}} - \hat{\theta}_2\hat{\boldsymbol{F}}_{\boldsymbol{n}}) \end{pmatrix}$$

$$\to \frac{T}{n_t}\sum_{n=1}^{N_{X_{est}}} \left[-\lambda_n\boldsymbol{F}_{\boldsymbol{n}}{}^T\right] \begin{pmatrix} -D^*\boldsymbol{I}_{\boldsymbol{n_t}} & \boldsymbol{I}_{\boldsymbol{n_t}} \end{pmatrix} \left[\begin{pmatrix} -\lambda_n\boldsymbol{I}_{\boldsymbol{n_t}} & 0 & 0 \\ -\theta_2^*\boldsymbol{I}_{\boldsymbol{n_t}} & \boldsymbol{I}_{\boldsymbol{n_t}} & -\theta_1^*\boldsymbol{I}_{\boldsymbol{n_t}} \end{pmatrix} \begin{pmatrix} \hat{\boldsymbol{F}}_{\boldsymbol{n}} - \mathbb{E}(\hat{\boldsymbol{F}}_{\boldsymbol{n}}) \\ \hat{\dot{\boldsymbol{F}}}_{\boldsymbol{n}} - \mathbb{E}(\hat{\dot{\boldsymbol{F}}}_{\boldsymbol{n}}) \\ \hat{\boldsymbol{G}}_{\boldsymbol{n}} - \mathbb{E}(\hat{\boldsymbol{G}}_{\boldsymbol{n}}) \end{pmatrix} \right] \tag{9.54}$$

$$+ \frac{T}{n_t}\sum_{n=1}^{N_{X,est}} \left[-\lambda_n\boldsymbol{F}_{\boldsymbol{n}}{}^T\right] \begin{pmatrix} -D^*\boldsymbol{I}_{\boldsymbol{n_t}} & \boldsymbol{I}_{\boldsymbol{n_t}} \end{pmatrix} \left[\begin{pmatrix} -\lambda_n\boldsymbol{F}_{\boldsymbol{n}} & \boldsymbol{0} & \boldsymbol{0} \\ \dot{\boldsymbol{F}}_{\boldsymbol{n}} & -\boldsymbol{G}_{\boldsymbol{n}} & -\boldsymbol{F}_{\boldsymbol{n}} \end{pmatrix} \begin{pmatrix} 1 \\ \hat{\theta}_1 - \mathbb{E}(\hat{\theta}_1) \\ \hat{\theta}_2 - \mathbb{E}(\hat{\theta}_2) \end{pmatrix} \right] \tag{9.55}$$

Since $\hat{\theta}_1$ and $\hat{\theta}_2$ only depends on $\hat{F}_0(t)$, $\hat{G}_0(t)$ and $\hat{DF}_0(t)$, which is independent with $\hat{F}_n(t)$, $\hat{G}_n(t)$ and $\hat{DF}_n(t)$, variance of $\sum_{n=1}^{N_{X,est}}\langle \hat{\dot{F}}_n(t) - \hat{\theta}_1\hat{G}_n(t) - \hat{\theta}_2\hat{F}_n(t) +$

$\lambda_n \hat{F}_n(t) D^*, -\lambda_n \hat{F}_n(t) \rangle_{n_t}$ is sum of two component $\left(\frac{T}{n_t}\right)^2 B_{21}$ and $\left(\frac{T}{n_t}\right)^2 B_{22}$, which are variance of term (9.54) and (9.55), respectively.

First, we look at B_{21}, which is variance of term (9.54). With simple calculation, we have $B_{21} = \sum_{n=1}^{N_{X,est}} (b_{21}^{xxn} + b_{21}^{xyn} + b_{21}^{yyn})$, where

$$
\begin{aligned}
b_{21}^{xxn} &= D^{*2} \lambda_n^4 \boldsymbol{F_n}^T \boldsymbol{\Phi} (\boldsymbol{\Phi}^T \boldsymbol{\Phi})^{-1} \boldsymbol{\Phi}^T \boldsymbol{F_n} s_2 \\
b_{21}^{xyn} &= -2 D^* \lambda_n^3 \left[\theta_2^* \boldsymbol{F_n}^T \boldsymbol{\Phi} (\boldsymbol{\Phi}^T \boldsymbol{\Phi})^{-1} \boldsymbol{\Phi}^T \boldsymbol{F_n} s_2 - \boldsymbol{F_n}^T \boldsymbol{\Phi} (\boldsymbol{\Phi}^T \boldsymbol{\Phi})^{-1} \dot{\boldsymbol{\Phi}}^T \boldsymbol{F_n} s_2 \right] \\
b_{21}^{yyn} &= \lambda_n^2 \Big[\theta_2^{*^2} \boldsymbol{F_n}^T \boldsymbol{\Phi} (\boldsymbol{\Phi}^T \boldsymbol{\Phi})^{-1} \boldsymbol{\Phi}^T \boldsymbol{F_n} s_2 + \boldsymbol{F_n}^T \dot{\boldsymbol{\Phi}} (\boldsymbol{\Phi}^T \boldsymbol{\Phi})^{-1} \dot{\boldsymbol{\Phi}}^T \boldsymbol{F_n} s_2 \\
&\qquad + \theta_1^{*^2} \boldsymbol{F_n}^T \boldsymbol{\Phi} (\boldsymbol{\Phi}^T \boldsymbol{\Phi})^{-1} \boldsymbol{\Phi}^T \boldsymbol{F_n} s_1 - 2 \theta_2^* \boldsymbol{F_n}^T \boldsymbol{\Phi} (\boldsymbol{\Phi}^T \boldsymbol{\Phi})^{-1} \dot{\boldsymbol{\Phi}}^T \boldsymbol{F_n} s_2 \Big]
\end{aligned}
$$

With similar logic as that of derivation in proof of Lemma 18, we have

$$
\begin{aligned}
b_{21}^{xxn} &\to \frac{n_t \Delta \boldsymbol{x}}{T} \lambda_n^4 ||F_n(t)||^2 \sigma_f^2 = \frac{n_t \Delta \boldsymbol{x}}{T} b_{21}^{xxn*} \\
b_{21}^{xyn} &\to -\frac{n_t \Delta \boldsymbol{x}}{T} 2 D^* \lambda_n^3 \left[\theta_2^* ||F_n(t)||^2 \sigma_f^2 - \langle F_n(t), \dot{F}_n(t) \rangle \sigma_f^2 \right] = \frac{n_t \Delta \boldsymbol{x}}{T} b_{21}^{xyn*} \\
b_{21}^{yyn} &\to \frac{n_t \Delta \boldsymbol{x}}{T} \lambda_n^2 \left[\theta_2^* ||F_n(t)||^2 \sigma_f^2 + ||\dot{F}_n(t)||^2 \sigma_f^2 + \theta_1^{*2} ||F_n(t)||^2 \sigma_g^2 - 2 \theta_2^* \langle F_n(t), \dot{F}_n(t) \rangle \sigma_f^2 \right] \\
&= \frac{n_t \Delta \boldsymbol{x}}{T} b_{21}^{yyn*}
\end{aligned}
$$

Therefore,

$$
B_{21} \to \frac{n_t \Delta \boldsymbol{x}}{T} \sum_{n=1}^{N_{X,est}} \left(b_{21}^{xxn*} + b_{21}^{xyn*} + b_{21}^{yyn*} \right) = \frac{n_t \Delta \boldsymbol{x}}{T} B_{21}^* \tag{9.56}
$$

Now we look at B_{22}, which is variance of term (9.55). Based on results of asymptotic normality of $\hat{\theta}_1$ and $\hat{\theta}_2$ (Theorem 19), with simple calculation, we have

$$B_{22} = \begin{pmatrix} \sum_{n=1}^{N_{X,est}} \lambda_n \boldsymbol{F_n}^T \boldsymbol{G_n} & \sum_{n=1}^{N_{X,est}} \lambda_n \boldsymbol{F_n}^T \boldsymbol{F_n} \end{pmatrix} \text{cov} \begin{pmatrix} \hat{\theta}_1 \\ \hat{\theta}_2 \end{pmatrix} \begin{pmatrix} \sum_{n=1}^{N_{X,est}} \lambda_n \boldsymbol{F_n}^T \boldsymbol{G_n} \\ \sum_{n=1}^{N_{X,est}} \lambda_n F_n^T F_n \end{pmatrix}$$

$$\rightarrow \frac{n_t}{T\Delta \boldsymbol{x}} \begin{pmatrix} \sum_{n=1}^{N_{X,est}} \lambda_n \langle F_n(t), G_n(t) \rangle \\ \sum_{n=1}^{N_{X,est}} \lambda_n ||F_n(t)||^2 \end{pmatrix}^T \boldsymbol{\Sigma}^* \begin{pmatrix} \sum_{n=1}^{N_{X,est}} \lambda_n \langle F_n(t), G_n(t) \rangle \\ \sum_{n=1}^{N_{X,est}} \lambda_n ||F_n(t)||^2 \end{pmatrix}$$

$$= \frac{n_t}{T\Delta \boldsymbol{x}} \boldsymbol{b_{22}}^* \boldsymbol{\Sigma}^* \boldsymbol{b_{22}}^{*T} = \frac{n_t}{T\Delta \boldsymbol{x}} B_{22}^* \tag{9.57}$$

Therefore, according to results (9.56) and (9.57), we have $\sum_{n=1}^{N_{X,est}} \langle \hat{\hat{F}}_n(t) - \hat{\theta}_1 \hat{G}_n(t) - \hat{\theta}_2 \hat{F}_n(t) + \lambda_n \hat{F}_n(t) D^*, -\lambda_n \hat{F}_n(t) \rangle$ is asymptotically normally distributed with mean zero and variance $\frac{T\Delta \boldsymbol{x}}{n_t} (B_{21}^* + B_{22}^*)$. ■